

# Connectivity and Morphology of the Primate Brain

Inaugural-Dissertation

zur

Erlangung des Doktorgrades der  
Mathematisch-Naturwissenschaftlichen Fakultät  
der Heinrich-Heine-Universität Düsseldorf

vorgelegt von

**Andrew Reid**

aus

**Gander, Canada**

Mai, 2010

Aus dem Institut für Experimentelle Psychologie  
der Heinrich-Heine Universität Düsseldorf

Gedruckt mit der Genehmigung der  
Mathematisch-Naturwissenschaftlichen Fakultät der  
Heinrich-Heine-Universität Düsseldorf

Referent: Prof. Dr. Petra Stoerig

Koreferent: Prof. Dr. Egon Wanke

Tag der mündlichen Prüfung: 2 Juli, 2010

## Acknowledgements

It is customary, apparently, to fill this section with the names of one's friends and colleagues, but I have made so many great friends, and met so many intriguing colleagues over the course of my wonderful four year European adventure, that I will never be able to remember them all in the short time I have left to write this section. Here I will address by name only those colleagues whose conversation, collaboration, and companionship have been instrumental to my academic progress here in Nijmegen, and as for the rest, I hope it will suffice to refer to all of you in general, and I hope that you know who you are, and understand what your friendship has meant to me during this period.

First and foremost, my supervisor and friend Rolf Kötter, without whom I would most likely never have made the 180° detour that brought me across the Atlantic. Rolf has been a constant source of guidance for me, in many aspects of my work; for starters, he has taught me a new respect for anatomy where my attitude was – let's say – nonchalant previously. Through him I have met numerous others who are shining stars in their various disciplines, and this has taught me how broad the scope of my chosen field has really become. I am indebted to him in innumerable ways, not the least of which for serving as a mentor and a tower of strength and optimism in the face of a personal situation which I cannot begin to comprehend. Thank-you Rolf.

I cannot speak for the Ph.D. tenures of others, because I get the impression that any one experience is truly unique (and such is the attraction to academics, perhaps); but for me this has been a truly educational few years. Rolf contacted me about a position in 2006 on the basis of my neuroscientific background, combined with my computer experience and my expressed desire to move in the direction of computational neuroscience. I had little idea of what I was getting into. In the end, as this dissertation bears out, my research shifted more towards surface modelling and visualization software (with which many of my figures were produced), and a bit of graph theory thrown in for good measure. The forward modelling, which was a prospect both Rolf and myself were looking forward to, will have to wait. Such is the nature of science, and this is another aspect of the learning experience.

I have to extend many thanks to Frank-Erik de Leeuw, who approached us with the RUN-DMC data set four years ago, and has been enthusiastic about our collaboration ever since. Through Frank-Erik and my participation in the Donders Center, I have also met some great colleagues and collaborators, including Marcel Zwiers, Anouk van Norden and Lucas van Oudheusden, who were indispensable parts of the (Reid et al., 2010) publication, and Anil Tuladhar, with whom I have been collaborating on the diffusion-weighted imaging project. Egon Wanke at Heinrich Heine in Düsseldorf, and Antje Krumnack, who is now at the Justus-Liebig-Universität Gießen, have been excellent partners on the Shapley value and cortical hierarchies publications. All of you have heightened my interest in scientific research, and I hope we can work together again in the future.

My other colleagues in the Neuropi group, Biophysics department, and Donders Center have been equally as indispensable, both academically and socially. Gleb Bezgin collected me at the airport in Düsseldorf, and since that time has been helpful to me in more ways than I can communicate; on top of which he has become a close friend and a constant source of optimism. Ingo Bojak is a fellow researcher, a fine physicist, a solid mathematician, a good friend, and someone who I will perhaps remember most as the person who taught me the meaning of kalauer, which I have never been able to pronounce. Dirk Schubert, Rembrandt

Bakker, Thom Oostendorp, Eva Ludowig, and all of the wonderful students who have graced our lab at some point, have been irreplaceable lunch companions over the past few years, full of humour, intelligence, stories, minor trivia, and South Park anecdotes; I look forward to 12:30 every day.

Of course I must thank my parents and the rest of my family as well, who have been.. well, as perfect a family as a guy could ask for. Four years is a long time to be away from each other (especially when your little nephew has grown from a wee baby to an irrepressible bundle of energy), but not once have I felt alone over here, what with the emails and the Skyping and the Easter parcels and the visits. Love you guys, and I really couldn't have gotten through this thing without you.

# Table of Contents

Acknowledgements .....	i
Table of Contents .....	iii
List of Abbreviations .....	viii
List of Figures and Tables .....	x
List of Published Figures and Tables .....	xi
Abstract .....	xii
<b>1. Introduction .....</b>	<b>1</b>
1.1. Overview .....	1
1.2. The Neocortex .....	1
1.2.1. History .....	1
1.2.2. Anatomical Methods .....	3
1.2.3. Macroscale Anatomy .....	4
1.2.4. Mesoscale Anatomy .....	4
1.3. Human Brain Mapping .....	6
1.3.1. History and Definitions .....	6
1.3.2. Individual Differences .....	7
1.3.3. Representations .....	8
1.3.3.1. Textual (coordinate-independent) .....	8
1.3.3.2. Spatial (coordinate-dependent) .....	8
1.3.4. Atlases and Templates .....	9
1.3.4.1. Terminology .....	10
1.3.4.2. Classical atlases .....	11
1.3.4.3. Probabilistic atlases .....	11
1.4. Brain Connectivity .....	13
1.4.1. Structural Connectivity .....	13
1.4.1.2. Experimental methods .....	13
1.4.1.3. Metadata and databases .....	14
1.4.2. Functional Connectivity .....	15
1.4.3. Effective Connectivity .....	16
1.4.3.1. Multiple linear regression .....	17
1.4.3.2. Structural equation modelling .....	17
1.4.3.3. Dynamic causal modelling .....	18
1.4.4. Cortical Hierarchies .....	19
1.4.5. Graph Theoretical Approaches .....	20

1.4.5.1. Small worldness .....	22
1.4.5.2. Betweenness centrality .....	23
<b>1.5. Magnetic Resonance Imaging .....</b>	<b>24</b>
1.5.1. Basic Principles .....	24
1.5.1.1. Nuclear magnetic resonance .....	24
1.5.1.2. Field gradients .....	25
1.5.1.3. Acquisition protocols .....	26
1.5.2. Diffusion-Weighted Imaging .....	26
1.5.2.1. Principles .....	26
1.5.2.2. Diffusion tensor imaging .....	26
1.5.2.3. Q-ball and persistent angular structure imaging .....	27
1.5.2.4. Tractography .....	28
<b>1.6. Human Brain Morphometry .....</b>	<b>29</b>
1.6.1. Voxel-based Morphometry .....	29
1.6.2. Surface-based Morphometry .....	30
<b>1.7. The Aging Brain .....</b>	<b>31</b>
1.7.1. Neurological and Cognitive Correlates .....	31
1.7.1.1. Memory .....	31
1.7.1.2. Executive function .....	31
1.7.2. Structural Correlates .....	32
1.7.2.1. White matter .....	32
1.7.2.2. Grey matter .....	32
1.7.3. Structure and Function .....	33
1.7.4. Compensation .....	33
1.7.5. Small vessel disease .....	34
<b>2. Cortical Morphometry .....</b>	<b>35</b>
<b>2.1. Methods .....</b>	<b>35</b>
2.1.1. The RUN-DMC Dataset .....	35
2.1.2. Rationale and Ethics .....	35
2.1.3. Subjects .....	36
2.1.4. Imaging Protocols .....	36
2.1.5. Spatial Normalization .....	37
2.1.6. Nonuniformity Correction .....	37
2.1.6. White Matter Lesion Delineation .....	37
2.1.7. Cortical Grey Matter Thickness Estimation .....	37

2.1.7.1. Tissue classification .....	38
2.1.7.2. Surface approximation.....	38
2.1.7.3. Deformation constraints .....	39
2.1.7.4. Cortical thickness estimate .....	40
2.1.8. Cortical Parcellation.....	40
2.1.8.1. Landmark-based deformation .....	41
2.1.8.2. Intersubject surface coregistration .....	42
2.1.9. Statistical Analyses .....	43
2.1.9.1. False discovery rate .....	43
2.1.9.2. Random field theory.....	43
2.1.9.3. Mean Analyses .....	44
2.1.9.4. Vertex-wise Analyses .....	44
2.1.9.5. ROI-wise Analyses .....	44
2.1.9.6. Grouped by Age .....	44
<b>2.2. Results.....</b>	<b>45</b>
2.2.1. Descriptive Statistics.....	45
2.2.2. Age .....	47
2.2.3. Sex .....	49
2.2.4. White Matter Lesions .....	49
2.2.5. Accuracy of Brodmann Parcellation.....	49
<b>2.3. Discussion.....</b>	<b>50</b>
2.3.1. Distribution of Cortical Thickness.....	50
2.3.2. Age-related Cortical Thinning .....	52
2.3.3. Sex Differences .....	53
2.3.4. Relating White and Grey Matter Morphometry .....	53
2.3.5. General Considerations.....	54
2.3.6. Conclusions .....	54
<b>3. Shapley Values for Brain Networks .....</b>	<b>56</b>
<b>3.1. Methods .....</b>	<b>56</b>
3.1.1. The Shapley Function.....	56
3.1.2. The Shapley Function for Cortical Networks.....	57
3.1.3. Empirical Data.....	58
3.1.4. Statistical Comparisons of Vertex Indices.....	59
3.1.5. Lesioned Networks .....	59
<b>3.2. Results.....</b>	<b>60</b>

3.2.1. Intact Networks .....	60
3.2.1.1. Y92 network.....	60
3.2.1.2. W40 networks.....	60
3.2.2. Comparison with Other Measures.....	61
3.2.3. Lesioned Networks .....	63
<b>3.3. Discussion .....</b>	<b>63</b>
3.3.1. Intact networks.....	64
3.3.1.1. Y92 network.....	64
3.3.1.2. W40 networks.....	64
3.3.2. Comparison of Vertex-wise Graph Measures .....	65
3.3.3. Lesioned Network.....	65
3.3.4. General Considerations.....	65
3.3.5. Conclusions .....	66
<b>4. Optimization of Cortical Hierarchies.....</b>	<b>67</b>
<b>4.1. Methods.....</b>	<b>67</b>
4.1.1. Graph Representation and the Hierarchy Function.....	67
4.1.2. Empirical Data.....	68
4.1.3. Interregional Correlations.....	69
<b>4.2. Results.....</b>	<b>69</b>
4.2.1. FVE91 Original.....	69
4.2.2. FVE91 Modified .....	70
4.2.2.1. Alternative optimization criteria.....	72
4.2.3. Barone et al. Network.....	73
<b>4.3. Discussion .....</b>	<b>73</b>
4.3.1. Optimization of the FVE91 Network.....	74
4.3.1.1. Comparison with original hierarchy .....	74
4.3.1.2. Modified constraint set with hierarchical distance .....	74
4.3.1.3. Alternative optimization criteria.....	75
4.3.2. SLN% as a Hierarchical Distance Constraint.....	75
4.3.3. General Considerations.....	77
4.3.4. Conclusions .....	78
<b>5. Structural Integrity of Corticocortical Connections.....</b>	<b>79</b>
<b>5.1. Methods.....</b>	<b>79</b>
5.1.1. Image Preprocessing.....	79
5.1.2. Surface-to-Volume Projection of Cortical Parcellation .....	79

5.1.3. White Matter / Grey Matter Interface.....	81
5.1.4. Tractography.....	81
5.1.5. Structural Integrity Estimation.....	82
5.1.6. Mean Symmetry.....	82
<b>5.2. Results.....</b>	<b>83</b>
5.2.1. Connectivity.....	83
5.2.2. Integrity Measures.....	86
5.2.3. Mean Symmetry.....	86
<b>5.3. Discussion.....</b>	<b>86</b>
5.3.1. Connectivity.....	86
5.3.2. Integrity Scores.....	87
5.3.3. Mean Symmetry.....	87
5.3.4. General Considerations.....	88
<b>6. General Discussion.....</b>	<b>89</b>
6.1. The Blind Men and the Elephant.....	89
6.2. The Brain as a Computer.....	89
6.3. Lessons from the Aging Brain.....	90
6.4. Large, Longitudinal, Human Data Sets.....	91
6.5. Future Considerations.....	93
6.5.1. Informing Models of Effective Connectivity.....	93
6.5.2. Mean Field Modelling.....	94
6.5.3. Longitudinal Data.....	96
<b>7. References.....</b>	<b>97</b>
<b>8. Appendix.....</b>	<b>110</b>

## List of Abbreviations

<b>AC</b>	anterior commissure
<b>AD</b>	Alzheimer's Disease
<b>ADC</b>	apparent diffusion coefficient
<b>AITd</b>	anterior inferotemporal area, dorsal part
<b>AITv</b>	anterior inferotemporal area, ventral part
<b>BA</b>	Brodmann area
<b>BEDPOSTX</b>	Bayesian Estimation of Diffusion Parameters Obtained using Sampling Techniques with Crossing Fibers
<b>BOLD</b>	blood oxygen-dependent signal
<b>CESD</b>	Center for Epidemiologic Studies Depression Scale
<b>CITd</b>	central inferotemporal area, dorsal part
<b>CITv</b>	central inferotemporal area, ventral part
<b>CLASP</b>	Constrained Laplacian Automated Segmentation with Proximities
<b>CNS</b>	central nervous system
<b>CoCoMac</b>	Collations of Connectivity data on the Macaque brain
<b>CSF</b>	cerebrospinal fluid
<b>CT</b>	computed tomography
<b>DCM</b>	dynamic causal modelling
<b>DIDI</b>	Donders Institute Diffusion Imaging
<b>DTI</b>	diffusion tensor imaging
<b>DWI</b>	diffusion-weighted imaging
<b>EEG</b>	electroencephalogram
<b>EM</b>	electromagnetic
<b>F99-UA1</b>	macaque cortical surface representation
<b>FA</b>	fractional anisotropy
<b>FAST</b>	FMRIB's Automated Segmentation Tool
<b>FDR</b>	false discovery rate
<b>FDT</b>	FSL's Diffusion Toolbox
<b>FFA</b>	fusiform face area
<b>FLAIR</b>	Fluid-Attenuated Inversion Recovery (MRI acquisition)
<b>fMRI</b>	functional magnetic resonance imaging
<b>FMRIB</b>	Oxford centre for functional magnetic resonance imaging of the brain
<b>FSL</b>	FMRIB Software Library
<b>FVE91</b>	Felleman and Van Essen (1991) visual network
<b>FWE</b>	family-wise error
<b>GLM</b>	general linear model
<b>GM</b>	grey matter
<b>HARDI</b>	high-angular-resolution diffusion imaging
<b>ICA</b>	independent component analysis
<b>ICBM</b>	International Consortium for Brain Mapping
<b>MCMC</b>	Markov Chain Monte Carlo
<b>MEG</b>	magnetoencephalogram
<b>MMSE</b>	mini-mental state exam
<b>MP RAGE</b>	Magnetization-Prepared 180 degrees radio-frequency pulses and RApid Gradient-Echo sampling (MRI acquisition)
<b>MRI</b>	magnetic resonance imaging

<b>MT</b>	middle temporal visual area
<b>N3</b>	nonparametric nonuniformity intensity normalization
<b>NMR</b>	nuclear magnetic resonance
<b>NPI</b>	network participation index
<b>ODE</b>	ordinary differential equation
<b>ODF</b>	orientation distribution function
<b>PALS-B12</b>	Population-Average, Landmark- and Surface-based atlas
<b>PAS-MRI</b>	persistent angular structure magnetic resonance imaging
<b>PATCH</b>	Patching the Artifacts from Cardiac and Head motion
<b>PC</b>	posterior commissure
<b>PCA</b>	principal component analysis
<b>PET</b>	positron emission tomography
<b>PFC</b>	prefrontal cortex
<b>PITd</b>	posterior inferotemporal area, dorsal part
<b>PITv</b>	posterior inferotemporal area, ventral part
<b>PLIC</b>	posterior limb of the internal capsule
<b>PVE</b>	partial volume effects
<b>RF</b>	radio-frequency
<b>RFT</b>	random field theory
<b>RM</b>	Regional Map
<b>RNA</b>	ribonucleic acid
<b>ROI</b>	region of interest
<b>RUN-DMC</b>	Radboud University Nijmegen Diffusion tensor- and Magnetic resonance imaging Cohort
<b>SEM</b>	structural equation modelling
<b>SLN%</b>	proportion of supragranularly labelled neurons
<b>SPM</b>	statistical parametric map
<b>STP</b>	superior temporal polysensory area
<b>STS</b>	superiotemporal sulcus
<b>SVD</b>	cerebral small-vessel disease, or cerebral microangiopathy
<b>T1</b>	spin-lattice relaxation time constant
<b>T2</b>	spin-spin relaxation time constant
<b>TE</b>	echo time (MRI)
<b>TI</b>	inversion time (MRI)
<b>TR</b>	repeat time (MRI)
<b>V1</b>	visual area 1
<b>V2</b>	visual area 2
<b>V3</b>	visual area 3
<b>V4</b>	visual area 4
<b>VBM</b>	voxel-based morphometry
<b>W40</b>	Walker (1940) prefrontal network
<b>WM</b>	white matter
<b>WMH</b>	white matter hyperintensities
<b>WML</b>	white matter lesion
<b>WMLV</b>	white matter lesion volume
<b>Y92</b>	Young (1992) visual network

## List of Figures and Tables

<b>Figure 1.1.</b> The human cortex parcellated into lobes. ....	3
<b>Figure 1.2.</b> Basic six-layered structure of the neocortex. ....	4
<b>Figure 1.3.</b> The Brodmann parcellation. ....	7
<b>Figure 1.4.</b> Probabilistic atlases. ....	12
<b>Figure 1.5.</b> Investigations of structural connectivity. ....	14
<b>Figure 1.6.</b> Functional vs. effective connectivity. ....	17
<b>Figure 1.7.</b> Projection-based constraints for determining hierarchical relationships ....	20
<b>Figure 1.8.</b> Various graph representations. ....	21
<b>Figure 1.9.</b> NMR signal relaxation profiles. ....	25
<b>Figure 1.10.</b> Diffusion-weighted imaging. ....	27
<b>Figure 1.11.</b> DWI-based tractography ....	28
<b>Table 2.1.</b> Demographics for the RUN-DMC cohort. ....	36
<b>Figure 2.1.</b> Surface approximation performed by the Civet pipeline ....	39
<b>Figure 2.2.</b> Three possible measures of cortical thickness. ....	40
<b>Figure 2.3.</b> Weighting functions applied to Brodmann area ROIs. ....	42
<b>Figure 2.4.</b> Box plots showing the distribution of Thickness for each BA ROI ....	45
<b>Figure 2.5.</b> Three-dimensional renderings of vertex-wise values ....	46
<b>Table 2.2.</b> Results of ROI-wise statistical analyses. ....	47
<b>Figure 2.6.</b> Correlations between <i>WMLV</i> and <i>Thickness</i> ....	48
<b>Figure 2.7.</b> Weighing vertices by proximity to borders. ....	50
<b>Figure 2.8.</b> Delineation of BA36 ....	51
<b>Figure 2.9.</b> Delineation of the insula ....	52
<b>Figure 3.1.</b> Cortical networks analyzed for Shapley values. ....	58
<b>Figure 3.2.</b> Shapley values for the Y92 network. ....	60
<b>Figure 3.3.</b> Shapley values for the three W40 variants. ....	61
<b>Table 3.1.</b> Comparison of network measures. ....	61
<b>Figure 3.4.</b> Correlation coefficients calculated between six vertex-wise graph measures ....	62
<b>Figure 3.5.</b> Simulated focal lesions. ....	62
<b>Figure 3.6.</b> Ranges for the Shapley values of the remaining regions ....	63
<b>Figure 4.1.</b> Two directed graph representations of a hierarchical cortical network. ....	67
<b>Figure 4.2.</b> Modified projection scheme from FVE91 ....	68
<b>Table 4.1.</b> Constraint sets specifying ranges for the modified FVE91 scheme. ....	69
<b>Figure 4.3.</b> Optimization of FVE91 with original constraints. ....	70
<b>Figure 4.4.</b> Hierarchies obtained through the modified constraints for FVE91 ....	71
<b>Figure 4.5.</b> The mean cortical hierarchical level distributed across the macaque cortex ....	71
<b>Figure 4.6.</b> Correlations across ten constraint sets, of interregional distance. ....	72
<b>Table 4.2.</b> Projections which produced violations in all constraint sets ....	73
<b>Figure 4.7.</b> Hierarchy produced from Barone et al. (2000) ....	73
<b>Figure 4.8.</b> Absolute versus relative measures as a baseball analogy. ....	76
<b>Figure 4.9.</b> Toy example for calculating relative SLN% weights. ....	76
<b>Figure 5.1.</b> The regional map (RM) painted on three surface templates. ....	80
<b>Figure 5.2.</b> Projection of the surface-based RM parcellation into native volume space ....	80
<b>Figure 5.3.</b> Preliminary results for DWI tractography. ....	84
<b>Figure 5.4.</b> Superior view of DWI-derived connectivity ....	85
<b>Figure 5.5.</b> Histograms of DWI-derived data. ....	86

<b>Figure 6.1.</b> Example DCM formulation, to investigate effective connectivity .....	94
<b>Figure 6.2.</b> Mean field model (MFM) with realistic geometry .....	95

## List of Published Figures and Tables

<b>Figure 1.3.</b> (Reid et al., 2010)
<b>Figure 1.7.</b> (Reid et al., 2009)
<b>Table 2.1.</b> (Reid et al., 2010)
<b>Figure 2.4.</b> (Reid et al., 2010)
<b>Figure 2.5.</b> (Reid et al., 2010)
<b>Table 2.2.</b> (Reid et al., 2010)
<b>Figure 2.6.</b> (Reid et al., 2010)
<b>Figure 3.1.</b> (Kötter et al., 2007)
<b>Figure 3.2.</b> (Kötter et al., 2007)
<b>Figure 3.3.</b> (Kötter et al., 2007)
<b>Table 3.1.</b> (Kötter et al., 2007)
<b>Figure 3.4.</b> (Kötter et al., 2007)
<b>Figure 3.5.</b> (Kötter et al., 2007)
<b>Figure 3.6.</b> (Kötter et al., 2007)
<b>Figure 4.1.</b> (Reid et al., 2009)
<b>Figure 4.2.</b> (Reid et al., 2009)
<b>Table 4.1.</b> (Reid et al., 2009)
<b>Figure 4.3.</b> (Reid et al., 2009)
<b>Figure 4.4.</b> (Reid et al., 2009)
<b>Figure 4.5.</b> (Reid et al., 2009)
<b>Figure 4.6.</b> (Reid et al., 2009)
<b>Table 4.2.</b> (Reid et al., 2009)
<b>Figure 4.7.</b> (Reid et al., 2009)

## Abstract

Modern neuroscientific research is built upon the solid foundation of over a century of pioneering efforts by anatomists, physiologists, physicians, surgeons, and more recently physicists, mathematicians, and computer scientists. The study of the neocortex – its structural organization and function – has proven a particularly difficult undertaking, and yet it may be fundamental to the understanding of human cognition, as well as neurological pathologies such as the loss of memory, sensation, motor function, and various forms of dementia. This dissertation focuses on both the structure and function of cortex using a number of distinct approaches.

Firstly, I present the results from morphometric analyses of a large cohort of elderly adults with symptomatic small vessel disease, called the Radboud University Nijmegen Diffusion tensor- and Magnetic resonance imaging Cohort (RUN-DMC). Cortical surface representations of 485 subjects were obtained from structural MRI scans, and analyzed for the effects of age, sex, hemisphere, and white matter lesion volume, both as whole-surface and region-of-interest analyses. A distinct pattern of age-related cortical thinning was observed, which was greatest in prefrontal cortex, lateral and medial temporal cortex, and parts of primary visual and primary auditory cortex. The relationship of white matter lesion volume with cortical thickness was investigated across three age groups, indicating a strong negative correlation in most Brodmann areas for adults aged 60-85, as well as two paradoxical positive correlation in motor and sensory association regions.

Secondly, drawing on graph and game theory, I present a novel formulation of the Shapley value, originally devised to analyze economic systems, to assess the degree to which individual vertices in a graph (representing connected cortical regions), contribute to the global connectivity of that graph. Shapley values were calculated for both intact and lesioned networks, obtained from macaque tract tracing literature, to demonstrate their utility for analyzing real cortical networks, and predicting the effects of insults to these networks. The Shapley value is compared to existing graph measures of cortical networks, demonstrating a fair degree of covariance – but not complete redundancy – particularly with the betweenness centrality measure.

Thirdly, I present an extension of the cortical hierarchy idea, first presented by Felleman and Van Essen (1991), which associates the anatomical patterns of cortical projections with their position in a functional hierarchy. A novel optimization framework is described, which uses continuous scales and ranges of values as constraints which define hierarchical relationships. The results of this optimization produce a hierarchy which is optimal, but which still has a number of constraint violations, corresponding to a number of regions which may be interesting for future anatomical investigation. Finally, a new measure based upon cell counting techniques, called the SLN%, is considered as a novel constraint for the optimization.

Fourthly, and finally, I present a novel method for assessing the degree to which an interregional projection is compromised by a white matter lesion, based upon diffusion-weighted MRI probabilistic tractography. Preliminary results from this method indicate that connectivity for long-range projections is difficult to detect using this technique; however, ways in which to resolve this issue are discussed. In light of the above research, I conclude by discussing the implications for clinical and basic research, and illustrate a number of future research prospects.

# 1. Introduction

## 1.1. Overview

What follows is a brief introduction into the very many topics which converge on the research projects that follow. This section is divided into seven parts, describing: (1.) *the neocortex*, which is the biological system of interest – here I describe a bit of the history and origins of neocortical research; (2.) *human brain mapping*, in which I outline the various ways in which the human brain can be mapped, and the various issues which arise when one attempts to do so; (3.) *brain connectivity*, in which I present the cortex as a connected network, and describe the various types of connectivity (structural, functional, and effective), and how they are presently studied; (4.) *magnetic resonance imaging*, which is the data acquisition method for the morphometric and tractographic analyses – here I introduce some of the basic principles behind MRI and diffusion-weight imaging; (5.) *human brain morphometry*, in which I discuss two methods of measuring the geometry of the brain, and in particular the neocortex; and finally (6.) *the aging brain*, where I discuss the cognitive, structural, and functional ways in which the brain degrades in old age.

## 1.2. The Neocortex

The *neocortex* is the biological subject of all the discussion which follows in this dissertation. As such, it is useful to precede the discussion with a brief overview of this complex bit of tissue, and thereby set the context for what follows. Neocortex is the outermost layer of the central nervous system (CNS), and is a distinguishing characteristic of the class *Mammalia*. Its name derives from the observation that it is the evolutionarily newest addition to the CNS, and together with *paleocortex* and *archicortex* it comprises the cerebral cortex of the mammalian brain. Following a convention of sorts, and considering that it is the only part of the cerebral cortex with which we shall here be concerned, the neocortex will herein be referred to synonymously as simply “cortex”.

### 1.2.1. History

An association between brain and behaviour goes back at least as far as Hippocrates, who among other inquiries had a keen interest in the physiology of epilepsy (Chang et al., 2007). A clear focus upon the functional roles of neocortex, however, was first suggested by Franz Joseph Gall, upon whose morphological speculations the field of *phrenology* was founded (see Section 1.6), and documented more precisely by Broca (Broca, 1861) and Wernicke (Wernicke, 1874), each of whom inferred functional roles on the basis of their disruption by focal brain lesions in human cortex, which resulted in specific forms of aphasia. Contemporaneously, (Fritsch and Hitzig, 1960) first directly demonstrated the localized function of cortex, by eliciting stereotypical motor responses with targeted electrical stimulation of the dog brain. These and similar findings have lent support to the theory that the cortex behaves in a localized fashion; i.e., that each of its specific functions is subserved by a distinct neuroanatomical structure, which is specialized for that function. This theory was further substantiated by detailed investigation into the cytoarchitectonic organization of cortical tissue by Campbell (Campbell, 1905) and Brodmann (Brodmann, 1905, 1909), who

## Introduction

demonstrated that localized patches of tissue formed a clearly distinguishable topology across the neocortical sheet (see Section 1.3).

Despite the appeal of this localization hypothesis, it had a number of prominent opponents – notably John Hughlings Jackson and Karl Lashley, the latter of whom argued that, apart from low-level sensory or motor functions, there did not appear to be any sensible connection between cortical lesion location and higher level functions such as learning and memory. In particular, Lashley (Lashley, 1950) showed that by lesioning non-sensory regions of cortex in rats, he could disrupt maze learning performance to a degree which was proportional to the extent of the lesion, and independent of its location. On the basis of this and other of his experimental findings, he concluded that memory traces, or *engrams*, are distributed equally throughout the cortex (his principle of *equipotentiality*), and that memories or learned behaviours emerge by means of an integration of neuronal activity specified by the connectivity provided by engrams, which are in turn formed by more general facilitation mechanisms including hormones and emotions (his principle of *mass action* or *mass facilitation*).

As is commonly the case with two seemingly opposing schools of thought, the more parsimonious theory of cortical function is likely one which incorporates parts of both. Consider, for instance, face recognition. The existence of neurons selective for specific faces, or parts of faces, have been widely reported in the macaque superior temporal sulcus (STS) (Gross et al., 1972; Desimone, 1991; Perrett et al., 1991). In humans, fMRI evidence points to an analogous function in the fusiform face area (FFA), located in inferotemporal cortex (IT) (Kanwisher et al., 1997), and localized lesions to this area typically result in a complete inability to perceive or differentiate faces, a condition called *prosopagnosia* (De Renzi, 2000). This evidence supports the idea that brain function, even at the level of complexity of face recognition, is supported by localized processing “modules”, as predicted by the localization hypothesis. However, a large amount of neural processing is required to either perceive a face, or to encode it in memory. STS receives input from the ventral processing stream, including visual areas V1, V2, and V4, where complex visual stimuli are thought to be broken into basic elements and recombined into shapes and textures, from which components they are constructed into complete face representations by specialized cells in FFA (Rolls, 2000). Moreover, to remember a face, it must be encoded, a process that appears to activate a broad network of areas, including amygdala and hippocampus, and extrastriate, frontal and parietal cortices (Keightley et al., 2010).

From the viewpoint of modern neuroscience, one of the most appealing theories of cortical function is that it is comprised of many discrete sub-networks which are specialized for different types of information processing. Some of these modules may construct primitive topological feature representations of sensory stimuli, others may perform temporal encoding. Some may specialize in producing motor commands, others may integrate multimodal information, or coordinate emotional responses. These individual modules, which are expressed anatomically as contiguous cortical or subcortical regions, are connected up in specific ways which optimize the information transfer between them: a module is “wired” to expect certain types of information as input, to transform or integrate that information in specific ways, and to transmit new information of a specific type to their own target modules (see, for instance: (Houk and Wise, 1995)). How such an organization might function in the human or macaque cortex is a very open question, although frequency

analysis of interregional oscillations may provide some important clues (Fries, 2009). In this dissertation I describe a number of investigative approaches which seek to address parts of this open question: namely, graph theoretical and computational studies of cortical connectivity, and an MRI-based inquiry into age- and pathology-related alterations to cortical morphology.

### 1.2.2. Anatomical Methods

Our current understanding of the anatomy of human neocortex owes itself to a number of methodological advances. The most important of these, in the context of the present dissertation, include: (1.) *histology*, which involves the microscopic observation of cells and their components; (2.) *tract tracing*, which is a form of histology that investigates the specific long-range connectivity patterns of the brain (discussed in Section 1.4.1.2); and (3.) *neuroimaging*, which permits the *in vivo* observation of both the structure and function of the human brain; it is the subject of Section 1.5.

Histology refers to the study of microscale anatomy; in neuroscience it typically refers to the investigation of cell morphology. Histological studies of the human cortex can be conducted on sections of post-mortem brain tissue, and often seek to qualitatively or quantitatively describe the distribution and morphology of neurons, including their spatial organization, packing density, size, and orientation – features which are collectively referred to as cytoarchitecture. A related field of research focuses on the architecture of white matter (i.e., myelinated axonal projections), which is referred to as myelinoarchitecture (Eickhoff et al., 2005a). More recent advances in genetics have facilitated a third form of histological investigation – focusing on so-called receptorarchitecture. This methodology utilizes label substances which target specific RNA precursors, and thus permit an indirect spatial quantification of protein expression; the target molecules in this case being receptor proteins. Histological observations such as these have been the basis of many attempts to map the human brain (e.g., (Brodmann, 1909)) (see also Section 1.3).

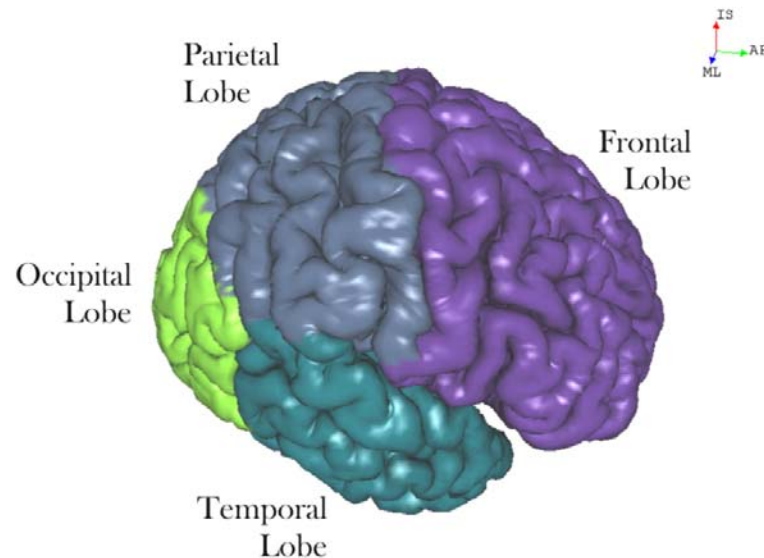


**Figure 1.1.** The human cortex parcellated into lobes. The anatomical reference set uses three primary axes: AP=anterior-posterior (front-to-back; also called rostral-caudal), ML=medial-lateral (middle to left and right sides), and IS=inferior-superior (bottom to top; also called ventral-dorsal).

### 1.2.3. Macroscale Anatomy

In humans, neocortex is a component of the telencephalon, also referred to as the cerebrum, which also includes white matter, amygdala, hippocampus, rhinencephalon, and lateral ventricles. The neocortex is comprised of a convoluted “sheet” of grey matter, with a thickness ranging from 1.5 to 5 mm. These convolutions are referred to as gyri (singular gyrus), which are its outward, visible protrusions, and sulci (singular sulcus), which are its inward invaginations. The cortical sheet itself can be coarsely subdivided into four lobes, separated by major sulci: frontal, temporal, parietal, and occipital; as well as insula and cingulate cortex (Figure 1.1).

### 1.2.4. Mesoscale Anatomy

Histology of neuronal tissue was greatly advanced by the neuronal staining methods discovered by Camillo Golgi and Franz Nissl, which bear their names. Golgi’s method in particular has been useful for characterizing and classifying individual cells, due to its still-mysterious ability to stain a small number of neurons in their entirety, including all neurites. Ramon y Cajal, for instance, utilized this technique to examine the cytoarchitecture of many parts of the human central nervous system, an endeavour at which he was extremely prolific, and for which he and Golgi shared the Nobel Prize in Physiology or Medicine in 1906 (see (Fishman, 2007)). Much of the early anatomy of the cortex was built upon histological staining methods, which revealed, among other observations: (1.) that the brain is comprised of distinct cellular units – particularly neurons and glial cells; (2.) that these units are morphologically heterogeneous and can be classified on this basis; (3.) that neurons are comprised of somata, dendritic arbours, and axons; and (4.) that the cortex is organized generally into cytoarchitecturally distinct layers.

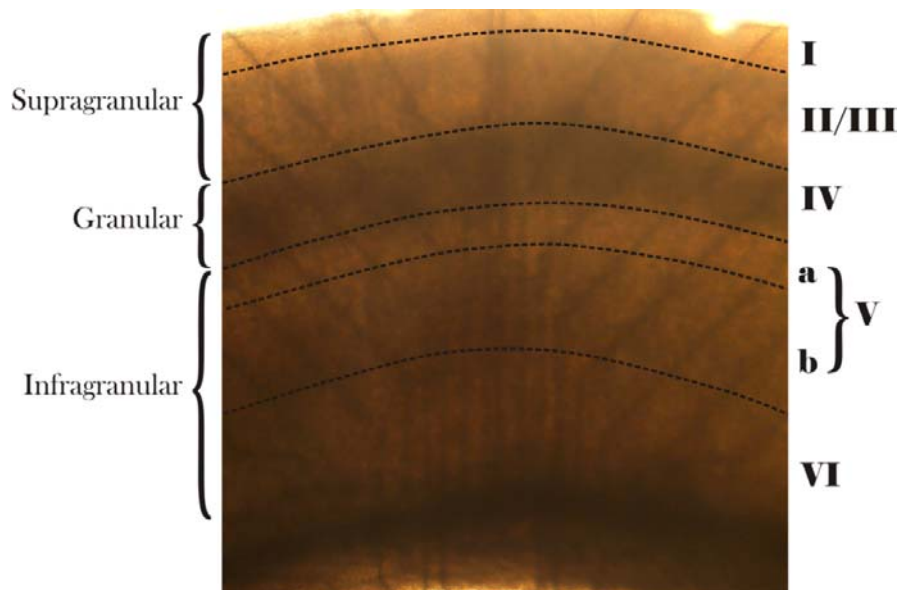


**Figure 1.2.** Basic six-layered structure of the neocortex. Shown on a microphotograph of sectioned rat somatosensory (barrel) cortex, where layer V is subdivided into a and b sublayers. This laminar organization is also referred to in terms of granular (layer IV), supragranular, and infragranular.

This latter observation was first reported by Theodor Meynert (Meynert, 1868), and later expanded and systematized by Korbinian Brodmann (Brodmann, 1905, 1909) – among

others. Considering the laminar schemes proposed by a variety of independent researchers, Brodmann discussed the lamination of cortex in terms to two basic criteria: *ontogeny* (or embryonic development), and *comparative anatomy* (comparisons between the phylogeny of different species). Ontogenetically, cortical development occurs in an inside-out fashion, with the result that more superficial layers develop later (which further suggests that they are phylogenetically more recent). In terms of comparative anatomy, Brodmann made the assertion that virtually all mammals have basic six-layered cortices in the embryonic stage of development, which tend to decrease in adult “lower” mammals with lissencephalic brains. This scheme is presented in Figure 1.2.

### 1.3. Human Brain Mapping

*§1. Cartography is the diagrammatic imitation of the known parts of the World with its unique features and it differs from Chorography since really this is the selecting out of certain regions as such to detail almost all the features in the smallest detail, and fixing in place such things as harbours, villages, towns and the course taken by rivers.*

*§2. The concern of Cartography is to determine the nature of the Earth by showing it as one whole, how it is formed and, from one given point, show a comprehensive circumscription with contours, the location of rivers, great cities and races of people most worthy of mention, and the shape of every one of the most distinguished features.*

*§3. In its ultimate role, Chorography holds the key to describing just one part of the above mentioned whole as if one represented just the ear or the eye alone. But Cartography is the viewing of the whole, the analogy being that concerned with showing the whole head.*

–Ptolemy, on the differences between Chorography and Cartography. *Geographica*. (Ptolemy)

By way of introduction into one of the world's first treatises on cartography, Ptolemy draws a distinction between it and the related field of chorography (a term linked to the modern practice of surveying), pointing out that while the latter is concerned with the detailed description of some local terrestrial feature, the former approaches a holistic geometric representation of Earth, as well as its relation to the heavens. He draws an analogy with the description of the head, which is fortuitous for the present discussion because it is a nice way of introducing the parallel between the ancient science of cartography – the mapping of Earth – and the mapping of the human brain. As an earth science, cartography represents a fundamental tool for all other disciplines of earth science. A knowledge of maps, for instance, was critical to the later understanding of navigation, plate tectonics, glacial activity, and volcanism. Similarly, as we shall see, a knowledge of brain maps lays the groundwork for a large part of modern neuroscientific research.

Ptolemy's comparison of local and holistic representations of terrestrial topography is especially applicable to the problem of utilizing localized brain maps for the purpose of compiling larger scale brain networks (discussed in Section 1.4.1). His analogy falls short, however, at one crucial distinction. Whereas Earth cartographers had only one, relatively constant, subject of interest – our planet – brain cartographers have the added difficulty of mapping an entire population of individual brains, for any given animal species. And while there does appear to be a degree of topographical consistency across individuals within a species, there is also a large degree of individual variation – particularly in humans – which adds a new layer of complexity to the problem. What follows is a description of the historical development of brain mapping, definitions of its most important concepts, an introduction to the different topographical representations of this complex organ, and a general overview of the aspects of human (and non-human primate) brain mapping most relevant to this discussion.

#### ***1.3.1. History and Definitions***

Seeking an anatomical basis for the localization hypothesis, Brodmann undertook a systematic parcellation of the cortical sheet on the basis of laminar patterns of cytoarchitecture, which often exhibit sharp transitions that allow clear regional delineations (Brodmann, 1909; Zilles and Amunts, 2010). The result of this intensive effort was a 43-

region map of human cortex (Figure 1.3), in addition to maps in a number of different species, across which he made an attempt to attribute homologies. Further investigations into anatomical parcellation followed that of Brodmann. Cécile and Oskar Vogt, working alongside Brodmann, utilized myelin stains to develop a myelinoarchitectonic map, which subdivided the cortex into 200 regions (Vogt and Vogt, 1919). Von Economo and Koskina expanded upon the work of Brodmann, primarily by refining his ontology and further subdividing his parcellation (von Economo and Koskina, 1926).

The parcellation and methods of Brodmann have received a number of criticisms, most notably by Percival Bailey and Gerhardt von Bonin (Bailey and von Bonin, 1951), who argued that his methods suffered from individual observer bias, given that all observations and parcellations were made by Brodmann alone. Moreover, von Bonin and Bailey tested Brodmann's delineation methods by scrambling photographs of stained cortical tissue and attempting to ascribe these photographs to particular areas based solely upon Brodmann's cytoarchitectonic criteria. Observing that most Brodmann areas failed this test, they concluded that this criteria alone was insufficient to objectively classify the majority of the cortical sheet. This latter criticism is valid to an extent; however, since a parcellation into cortical regions is essentially an attempt to ascribe anatomical borders to distinct regions, the topological information utilized by Brodmann (and eliminated by von Bonin and Bailey) is a perfectly legitimate criterion for parcellation, suffering only in the case of neighbouring areas.

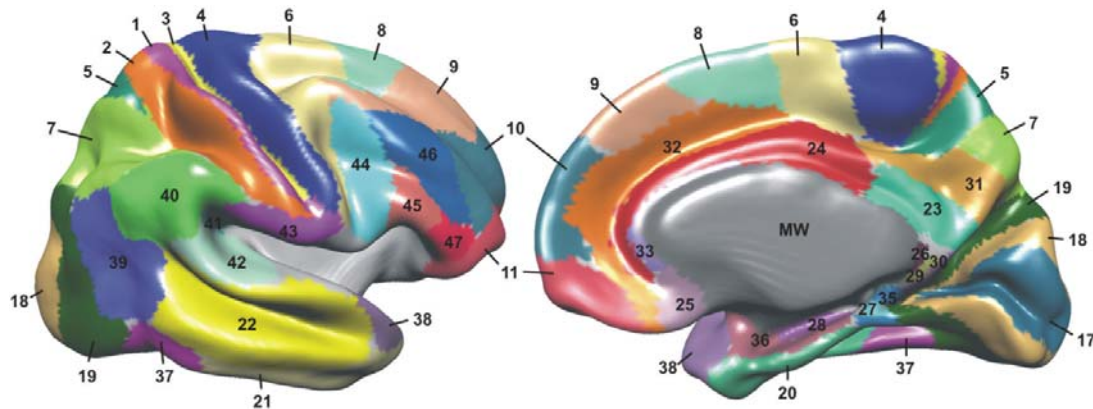


**Figure 1.3.** The Brodmann parcellation. Representation of the cytoarchitectonic parcellation of Brodmann (1905), on a population average human cortex. MW=artificially created medial wall.

### 1.3.2. Individual Differences

One obvious utility of a cortical parcellation is its assignment to individuals, from where it can serve as a means of identifying functional properties; such brain maps can, for instance, be used to link structural and functional phenotypes, or investigate how structural alterations, such as age-related degeneration, lesions, infarcts, or pathologies, are related to functional observations such as motor, sensory, cognitive, or memory deficits. Both the gross and cytoarchitectonic morphology of the human cortex, however, vary substantially across individuals, to a much greater extent than in other species (Kennedy et al., 1998). Since it is currently impossible to use cytoarchitecture or other histological approach to make regional

## Introduction

assignments *in vivo*, for either macaques or humans, this observation introduces a critical difficulty with respect to applying a canonical parcellation scheme, such as that of Brodmann, to living, functioning individuals within the species.

One approach to this problem utilizes the large-scale features of human cortex which are generally preserved across individuals: namely, major gyral and sulcal patterns. Treating these features as “landmarks”, it is possible to use their locations on the cortical surface as constraints for a spatial deformation field, which allows sets of nodes from two individual surface representations (see Section 1.3.3.2) to be mapped onto one another. This approach has been used to map both between individuals, between template surfaces, and even between primate species. While promising, however, this deformation method suffers from at least one major drawback: that the correspondence between major landmarks and cytoarchitectonic regions can vary substantially across individuals. This caveat was raised by Brodmann himself, and further substantiated by more recent histological methods (Amunts and Zilles, 2001; Uylings et al., 2005).

### ***1.3.3. Representations***

#### ***1.3.3.1. Textual (coordinate-independent)***

In the course of evolution of the field of comparative neuroanatomy – particularly tract tracing studies performed in macaque monkeys – a large number of distinct and localized brain maps have been devised in order to describe various scales of structural connectivity, with the notion that these might provide useful inferences into the structure of human brain networks. Typically, these “coordinate-independent” brain maps (Kötter and Wanke, 2005) make textual references to previously defined maps (e.g., statements such as: “Our area A is identical to/included within/contains so-and-so’s area X”), and often portray this relationship in a sectional figure. Given the large number of such anatomical studies that have been performed over the past century, however, the integration of this large body of mapping and connectivity data into a single cortical representation is a daunting task. This metadata approach has been undertaken in the form of the CoCoMac database, which provides a systematic means of cataloguing and comparing these textual representations, allowing the data to be integrated into cortex-wide representations. This database is described in more detail in Section 1.4.

#### ***1.3.3.2. Spatial (coordinate-dependent)***

Since histological investigations typically utilize sectional slices of neural tissue, spatial representations of human and macaque brains have traditionally taken the form of two-dimensional sections. This planar representation provides simple and intuitive figures for journal articles; however, because they are restricted to a single planar orientation, it is often difficult to determine anatomical relationships for features which do not occur within the chosen plane. The utility for morphometric analysis, moreover, is greatly limited.

Volumetric representations are usually compiled from stacks of planar images (of a specific thickness), and have become increasingly popular with the advent of both computing technology and advanced neuroimaging techniques. An MRI scan, for instance, is naturally represented in this way (see Figure 1.4). Volumetric representations allow sectional views at arbitrary plane orientations, and can also be visualized using three-dimensional rendering techniques, with optional masking of specific tissue classes such as skull and scalp, thus

providing a vastly improved means of showing anatomical, as well as functional, features. Volumetric representations also permit a wider array of analytical approaches, such as voxel-based morphometry (VBM), described in Section 1.6.1.

Since the neocortex takes the form of a convoluted sheet, it can be conveniently represented as a set of connected three-dimensional vertices: a tessellated two-manifold, as it is more formally known, or a surface mesh, as it will be referred to here. Such a mesh can be generated from a volumetric brain representation, by manually or algorithmically segmenting the image into tissue compartments (such as grey matter, white matter, and cerebrospinal fluid), and deforming a mesh of sufficient resolution to approximate the boundaries of these compartments (Dale and Sereno, 1993; Thompson et al., 1997; MacDonald et al., 2000; Kim et al., 2005). The resulting cortical surface can be used both as a visualization tool and as a means for performing a number of useful morphometric analyses, such as cortical thickness, gyrification, sulcul depth, and curvature. This representation is also quite useful as a population template (see Section 1.3.4 below).

Because two-manifolds are surfaces, they can also be represented in two dimensions, in the same way that the surface of the (pseudo-)spherical Earth can be represented as a two-dimensional map. As in the case of terrestrial maps, such a “flat map” representation of cortex is achievable by strategically defining “cuts” along the cortical surface, and unfolding it until it all of its vertices lie on a single plane (Figure 1.4). Although this inevitably results in a degree of spatial skewing, flat map representations provide a convenient view of the entire cortex, while retaining most of its neighbourhood relationships. Additionally, plotting curvature on this map allows gyrification patterns to be represented. Flat maps have also been used to define spatial deformation fields, allowing individual representations to be compared (Van Essen et al., 1998).

#### ***1.3.4. Atlases and Templates***

Through the course of history of neuroscientific research, there have been many attempts to formulate a generalized spatial representation of the brain’s anatomy, which representations are indispensable for performing statistical comparisons between subjects. So-called *stereotaxic* representations of neuroanatomy have become increasingly refined, in response to the demands of neurosurgery and neurology; however, these representations have almost invariably relied on tedious post-mortem histological methods obtained from a limited number of individuals (e.g., Brodmann’s parcellation), which are not possible in the living organism – and particularly the living human. In the past few decades, however, as computer technology and neuroimaging techniques have advanced, the prospect of developing a universal mapping scheme, or atlas, of the human brain, has become increasingly likely. Stereotaxic brain atlases can thus be classified into two categories: (1.) *classical atlases*, which are typically based upon a single – or small number – of specimens, and which provide a guide into the relative locations of anatomical features; and (2.) *probabilistic atlases*, which are based upon a sufficiently large number of specimens to be representative of a population, and specify absolute spatial coordinates, relative to which a probabilistic distribution, derived from the sample, can be expressed. This is perhaps best achieved through the definition of a standard, or template representation.

### 1.3.4.1. Terminology

Brain mapping uses a number of terms to refer to its elements, which are briefly introduced here:

#### i. Maps and parcellations

The term *map*, derived from the Latin *mappa*, for napkin, or towel (Merriam-Webster online dictionary), originally referred to terrestrial charts; i.e., a two-dimensional representation of the Earth's features. While the brain is a three-dimensional structure, the neocortex can be represented as a closed two-manifold, which can be further represented as a sphere, in the same way that the planet can be represented as a sphere. It is, however, often desirable to represent more of the brain's complexity than such a surface representation affords: i.e., white matter tracts, subcortical structures, ventricles, vasculature, etc. The term *map* can thus be extended to permit such volumetric representations. A *parcellation* is a class of map, in which the area or volume is subdivided into discrete parcels (areas or regions, see next). This term is usually used to refer to cortical parcellations.

#### ii. Areas and regions

The term *cortical area* is often used to refer to specific parcels of a cortical parcellation. Brodmann's areas are such an example. This term is appropriate to a surface representation, where subdivisions indeed have finite surface areas. However, in a volumetric representation, the use of "area" to describe a parcel is technically erroneous, given the mathematical sense of the word. Neither can the term "volume" be unambiguously used, as it typically refers to an entire volumetric map. The more general term "region" is often used instead, and this is the term I will adopt herein to refer to any brain parcel.

#### iii. Atlases and templates

The term "atlas" has been used in various ways within the brain mapping community, often confusingly, so it is worth dissecting here. Merriam-Webster defines the word as:

*atlas* **a**: a bound collection of maps often including illustrations, informative tables, or textual matter **b**: a bound collection of tables, charts, or plates.

This definition fits with, for instance, classical brain atlas representations, whose subjects were single or small numbers of individuals. Given, however, that the brain of a given species is in reality a *plurality* of brains, with substantial variability, this classical definition falls short. Instead, many modern atlases are probabilistic in nature (see, for example, (Mazziotta et al., 2001)); geometrically, such probabilistic atlases serve as templates onto which individual representations can be deformed, where the term *template* is defined as (Merriam-Webster):

*template* something that establishes or serves as a pattern.

As the term "atlas" is widely used in the field today, I shall use it herein to refer to mapping schemes of both varieties. The term "template" is best

reserved for discussions of the geometric operations required to compose or register individuals to probabilistic atlases.

#### ***1.3.4.2. Classical atlases***

Brodmann, the Vogts, von Economo & Koskina, and others have put forward cortical parcellation schemes based upon the post-mortem histological examination of brain slices, obtained from a small number of individuals. These pioneering efforts were painstaking and comprehensive, and their products can be considered atlases in the classical sense. More modern versions of such atlases are still being published, and utilized for investigations in animal models such as mouse, rat, and rhesus macaque (Mai et al., 1997; Paxinos et al., 1999), as well as neurosurgery in humans (Rengachary and Wilkins, 1996). Such atlases might also be referred to as *relativistic*, given that they are generally used to ascertain the relative locations of anatomical structures, which serve as a rough guide for the localization of target regions.

#### ***1.3.4.3. Probabilistic atlases***

Facing a growing need to represent the brain, as a plurality, with greater fidelity than that offered by relativistic atlases, Talairach and Tourneaux (Talairach and Tournoux, 1988) first introduced a method for geometrically aligning individual brain representations to one another. To this end, they produced a template representation (derived from the post-mortem brain of an elderly female), and then outlined a method for aligning individuals to this template. This alignment scheme consisted of dividing Euclidean space into 12 parts (Figure 1.4), defined by consistent midsagittal anatomical landmarks (anterior and posterior commissures, AC and PC), and then performing 12 separate linear transformations which would align the dimensions of the individual brain to those of the template. Despite numerous drawbacks to this approach (e.g., reliance on a single, non-representative template, or the use of local rather than global transformations), the template-based scheme it proposed established a groundwork for the construction of a probabilistic atlas of the human brain.

Further work has built upon this groundwork. Mazziotta and colleagues (Mazziotta et al., 2001) introduced a project aimed at establishing a population-based atlas representation of various data modalities, called the International Consortium for Brain Mapping (ICBM). This project currently collects and maintains data from a large number of subjects, using a variety of imaging modalities and standard protocols. As an important extension of the Talairach and Tourneaux template, Louis Collins and colleagues produced a new template called the MNI-305, consisting of MRI scans from 305 normal young adults, coregistered using a global 9-parameter linear transformation (Collins et al., 1994) and averaged across subjects. This volumetric atlas, or a derivation thereof called the ICBM-152, serves as an anatomical template for many modern processing tools (Ashburner and Friston, 1999; Smith et al., 2004) (Figure 1.4).

One shortcoming of the ICBM-152 is that, given the high variability of cortical gyri, it represents cortex as blurred regions, which makes good sulcal correspondence between coregistered images difficult to attain. David Van Essen (Van Essen, 2005) introduced a different form of population template, based not upon a volumetric representation, but upon a cortical surface representation. The Population-Average, Landmark- and Surface-based atlas (PALS-B12; Figure 1.4) is based upon cortical surface approximations of 12 normal

## Introduction

young adults (six males and six females), aligned to one another using sulcal landmarks, and averaged to produce a single surface representation. The PALS template exhibits a more consistent alignment of sulci than volume-based approaches, and thus arguably provides a more accurate means of aligning individual representations to one another. Moreover, a surface-based parcellation scheme can be used to respect both sulcal boundaries and neighbourhood relationships, both of which suffer in an assignment based upon a volumetric parcellation.

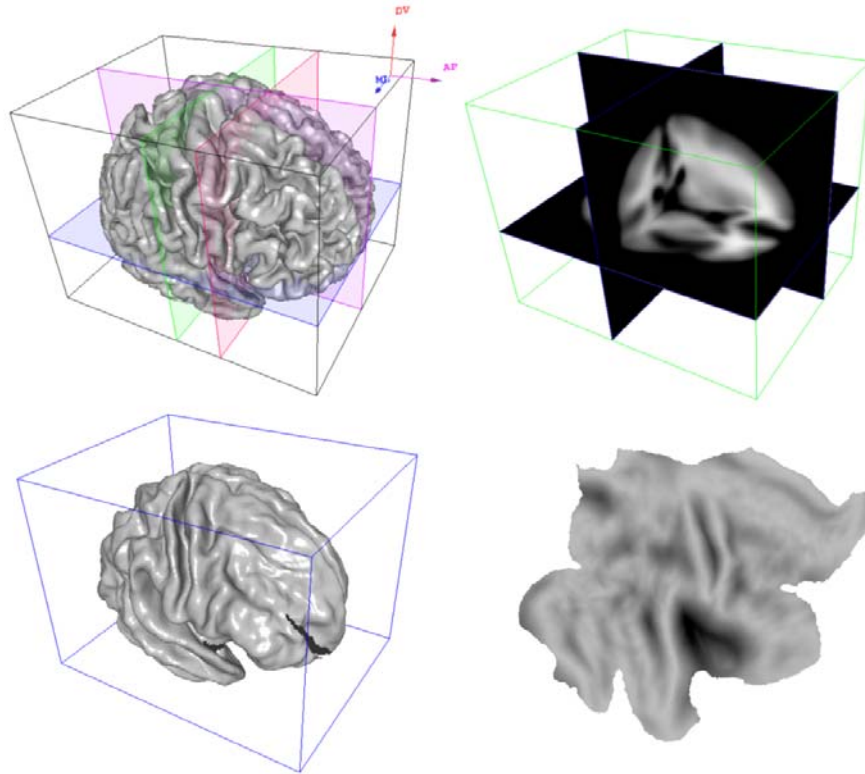


**Figure 1.4.** Probabilistic atlases. **Top Left:** Normalization scheme introduced by Talairach and Tournoux (1988). **Top Right:** ICBM-152 average volumetric template. **Bottom Left:** PALS-B12 surface template. **Bottom Right:** PALS-B12 flat map representation.

While population-based volumetric and surface atlases provide a powerful means of aligning individual representations, there remains the problem of how to represent brain parcellations. As discussed in Section 1.3.2, individual differences in anatomy make this assignment non-trivial. One approach which addresses this issue is the construction of a *probabilistic parcellation*. Using *ex vivo* human brain sections, and applying both cytoarchitectonic and receptorarchitectonic criteria (the latter referring to a distribution of expression for specific neurotransmitter receptor molecules), one can obtain a spatial probability distribution for various cortical regions, which can be assigned to standard space and applied to individual geometrical models which have been transformed to this space (Amunts and Zilles, 2001; Eickhoff et al., 2005b). A variation on this approach is the use of neuroimaging data as the criterion for regional delineation (Shattuck et al., 2008). While this latter approach suffers from a lesser spatial resolution, and does not permit the observation of cellular or molecular features, it has been shown to have a high degree of interrater reliability, and has the distinct advantage of being derived from an *in vivo* population.

## 1.4. Brain Connectivity

A popular view of the brain and its functionality is based upon the idea of connectionism: that the brain functions as a network of interconnected processing units, and that this connectivity is fundamental to its overall behaviour. Given the body of anatomical literature summarized here, there can be little doubt that the brain is indeed wired in such a fashion. The functional implications of this structural organization, however, remain one of the most investigated questions in neuroscientific research, and indeed form a substantial part of this dissertation. What follows is a summary of our current theoretical understanding of brain connectivity, and methods by which it is investigated.

### 1.4.1. *Structural Connectivity*

Structural connectivity refers to a physical connection between two distinct units. In a simple electrical circuit, for instance, this would refer to the “wiring” through which current can flow, and thus a physical means of signal transfer. In the brain, structural connectivity is determined by the observation of directed axonal projections from one brain region (the source) to another (the target). Such connections can be divided loosely into two categories: short-range (local) and long-range (interregional). Short-range connections (0-500 $\mu$ m) are typically found throughout the cortical sheet (Hellwig, 2000) and mediate the local spread of neuronal activity. Long-range connections are those which originate in one brain region and project via white matter fasciculi to another, distal, region. Under normal developmental conditions, long-range connectivity is very regular and specific within a species, and this specificity has also been observed to be preserved across related species such as primates.

#### 1.4.1.2. *Experimental methods*

The bulk of current knowledge about structural connectivity in the human brain is based upon comparative anatomy obtained largely from macaque monkeys. Such an approach requires the supposition of homologies between the two species, which can be based upon such criteria as ontogeny, cytoarchitecture, or function. Tract tracing is a staining method in which the tracer substance is injected at a specific location *in vivo*, allowed time to be actively transported along axons, and examined *ex vivo* for the resulting distribution of *labelled sites*. Tracer substances are typically of two classes, based upon the direction in which they are transported: anterograde (transported from the soma towards the axon terminal) and retrograde (transported from the axon terminal towards the soma). Figure 1.5 illustrates this paradigm for both tracer types. More recent advances in magnetic resonance imaging (MRI) allow an indirect, *in vivo*, noninvasive observation of cortical connectivity, by measuring the degree of anisotropic diffusion of water molecules in a technique called diffusion-weighted imaging (DWI; described in detail in Section 1.5.2).

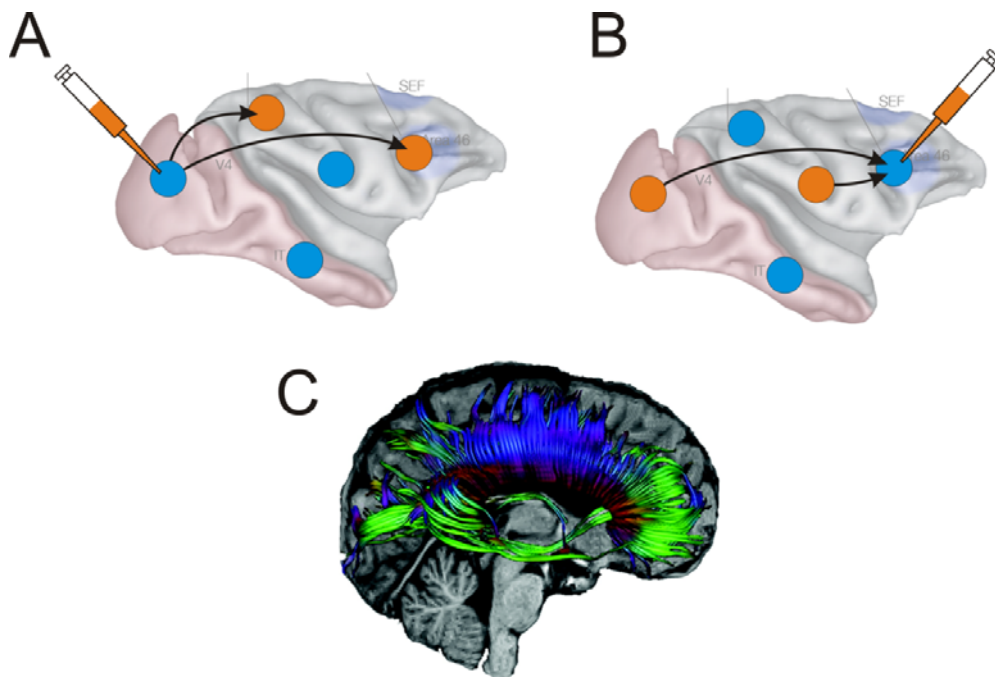


**Figure 1.5.** Investigations of structural connectivity. **A:** Anterograde tract tracing. Tracer substance is injected in a source region, taken up by somata, and transported to axon terminals in target regions (orange). **B:** Retrograde tract tracing. Tracer is injected in a target region, taken up at axon terminals, and transported back to somata in source regions. **C:** DWI-based tractography in the human brain (see Section 1.5.2).

#### 1.4.1.3. Metadata and databases

One drawback of the comparative anatomical approach is that, through its development, a large number of localized maps have been devised for individual studies which do not necessarily facilitate a comparison with other studies. It has been common practice, for instance, to introduce novel maps and nomenclature for structures with existing names, or to utilize differing scales of granularity depending on the scope of a given tract tracing experiment. Occasionally, textual statements or figures provide a means of relating structures in one study with those in preceding studies, but the overall result of this practice is a very large set of brain regions with connectivity information, but no simple means of incorporating this information into more holistic representations.

This problem of metadata has been approached in a number of ways. Most relevant for the present discussion is the CoCoMac database (Collations of Connectivity data on the Macaque brain) (Kötter, 2004), which provides a systematic compilation of a large amount of existing tract tracing literature, including a system of recording textual relationships between the brain areas of different maps (i.e., using set terminology indicating whether a brain structure A contains, is contained by, is equivalent to, or is disjoint from another brain structure B). Such ontological relationships permit the combination of structural connectivity information across many distinct maps, including those which are separated by a number of relational statements (or relationship *paths*; e.g.,  $A > B = C > D$  reduces to  $A > D$ ).

### 1.4.2. Functional Connectivity

As its name suggests, functional connectivity refers to a dynamic brain network through which signals are propagating – either by transduction of external stimuli, relaying of neuronal firing patterns, integration of diverged signal pathways, or generation of intrinsic activity. This idea is based upon the notion that the time series of activity from a given brain region  $A$  can be statistically compared to a second region  $B$ , and this comparison can demonstrate the degree to which the two signals are related to each other. The study of functional brain connectivity is thus an extension of signal theory into connected brain networks, and its investigations make extensive use of the statistical tools developed for this physical theory. Functional connectivity can be defined, in the context of neuroscience, as a statistical relationship – typically either *correlation* or *dependence* – between neural activity occurring within spatially distinct regions of the brain. These terms are discussed below:

#### i. Correlation:

The correlation  $r_{xy}$  between two random vectors (e.g., time series)  $\mathbf{x}$  and  $\mathbf{y}$ , is the degree of synchrony with which their values vary. More formally, it is the expectation of the product of their components, which depends upon the probability distributions of  $\mathbf{x}$  and  $\mathbf{y}$ , and can be expressed as:

$$r_{xy} = E\{xy\}$$

#### ii. Dependence:

The dependence of two random vectors  $\mathbf{x}$  and  $\mathbf{y}$  is defined in terms of probability densities and is proportional to the difference of the joint probability  $p_{x,y}(x,y)$  from the product of the marginal probabilities  $p_x(x)$  and  $p_y(y)$ . In other words, two variables are *independent* only if their probability together is equal to their probability separately:

$$p_{x,y}(x,y) = p_x(x)p_y(y)$$

If:

$$p_{x,y}(x,y) > p_x(x)p_y(y)$$

$x$  and  $y$  can be said to be *positively* dependent (i.e., they are more probable together than separately), and if:

$$p_{x,y}(x,y) < p_x(x)p_y(y)$$

$x$  and  $y$  can be said to be *negatively* dependent (i.e., they are less probable together than separately).

Correlation is in fact a special case of statistical dependence, where  $\mathbf{x}$  and  $\mathbf{y}$  are derived from linear functions, and their relationship is also linear. The two terms are also equivalent in the special case where both  $\mathbf{x}$  and  $\mathbf{y}$  have Gaussian distributions (see (Hyvärinen et al., 2001)). These two concepts are fundamental to a number of important signal processing techniques that are currently used to investigate neuroimaging data: uncorrelatedness is the basis of *principal component analysis* (PCA), and independence is the basis of *independent*

*component analysis* (ICA), both of which methods are used to isolate distinct, relatively disconnected networks of functionally connected brain regions.

In the analysis of functional connectivity, correlational approaches suffer from the fact that communication between brain regions will always have a specific transmission latency which, depending on the nature of the connectivity between regions  $A$  and  $B$ , and the temporal resolution of the recording method, may offset the phase of the oscillatory signal such that connected regions appear uncorrelated. This problem has been approached by calculating the *cross-correlation* (or *phase coherence*) of a pair of signals, which optimizes their correlation after accounting for a specific time-lag between them.

Statistical dependence can also be expressed in terms of *mutual information*,  $I(X; Y)$ , which is a measure derived from information theory, and describes the degree to which two vectors of data contain redundant, or mutual information. This measure was originally devised to analyze the degree to which two lines of code could be compressed without loss of information, but has proven quite useful in other aspects of signal processing. For discrete vectors, mutual information is defined as (Latham and Roudi, 2009):

$$I(X; Y) = \sum_{y \in Y} \sum_{x \in X} p_{x,y}(x, y) \log \left( \frac{p_{x,y}(x, y)}{p_x(x)p_y(y)} \right)$$

From this equation it is easy to see that any term in the summation is positive when  $p_{x,y}(x, y) > p_x(x)p_y(y)$ , negative when  $p_{x,y}(x, y) < p_x(x)p_y(y)$ , and zero when  $p_{x,y}(x, y) = p_x(x)p_y(y)$ . Thus mutual information is commonly utilized to assess the degree of functional dependence between two brain regions (Honey et al., 2007).

### 1.4.3. *Effective Connectivity*

While functional connectivity implies that connected regions are part of the same functional network, it does not provide information about how these regions are connected. For instance, if thalamic nucleus  $T$  has projections to both cortical regions  $A$  and  $B$ , then  $A$  and  $B$  will be functionally connected, even in the case where they have no direct structural connections between them (Figure 1.6). *Effective connectivity* refers to such causal relationships between brain regions, and as such affords stronger statements about how a brain network functions; e.g., activity in  $A$  *causes* subsequent activity in  $B$  (with some probability  $P$ ). According to (Büchel and Friston, 1997):

*Effective connectivity is closer to the intuitive notion of a connection than functional connectivity and can be defined as **the influence one neural system exerts over another** (Friston et al., 1993b), either at a synaptic (c.f. synaptic efficacy) or cortical level. ... It has also been proposed that “the [electrophysiological] notion of effective connectivity should be understood as the experiment and time-dependent, simplest possible circuit diagram that would replicate the observed timing relationships between the recorded neurons” (Aertsen & Preissl, 1991).*

There is an implication in this latter definition that while functional connectivity is a data-driven statistical measure, effective connectivity is model-based and requires a parametric optimization (i.e., a fit to dynamic empirical data) which can offer probabilistic estimates of how activity is propagated through a brain network. According to Büchel and Friston, two such models are needed: (1.) a representation of structural connectivity, i.e., as discerned

from neuroanatomical evidence; and (2.) a mathematical model describing the transmission of signals between connected regions.

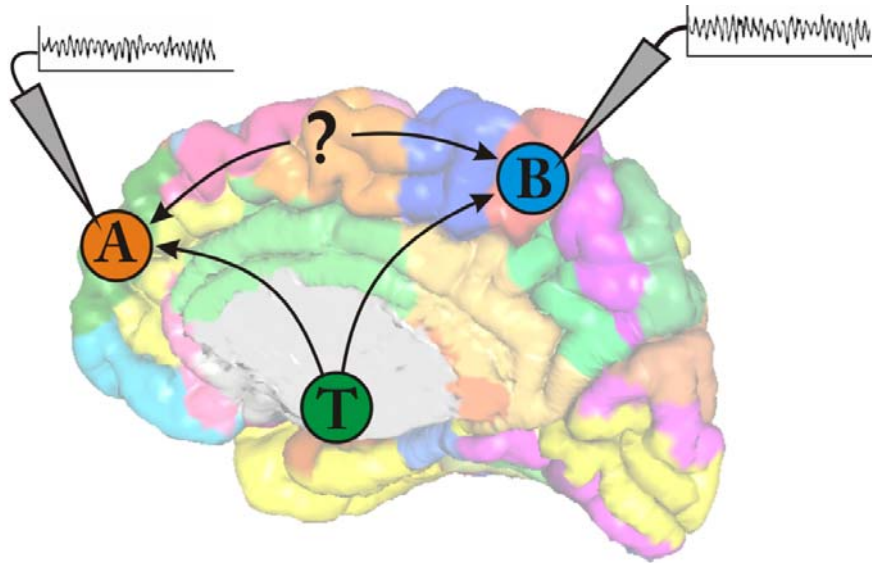


**Figure 1.6.** *Functional vs. effective connectivity.* Even if functional connectivity is demonstrated between brain areas A and B, it is impossible to infer from this whether a direct causal link exists between A and B, since they may be driven by a common input T.

Due to the complexity of making inferences on large networks, which do not tend to scale linearly, most investigations of effective connectivity focus on a limited set of regions. Three such approaches are summarized below: (1.) multiple linear regression, (2.) structural equation modelling (SEM); and (3.) dynamic causal modelling (DCM):

#### 1.4.3.1. Multiple linear regression

Perhaps the simplest mathematical representation is a linear model, of the form:

$$m_i = \sum C_{ij}m_j + e_i$$

where  $m_i$  is the activity in brain region  $i$ ,  $C_{ij}$  is the connection strength from region  $j$  to region  $i$ , and  $e_i$  is an error term (from (Büchel and Friston, 1997)). This relationship can then be treated as a multiple linear regression problem, where the weights  $C$  are the coefficients and brain activity measures  $m_j$  are the regressors.

In practice, however, the covarying activity of brain networks changes with respect to time, and thus more temporally-informed modelling approaches are necessary to obtain accurate estimates of effective connectivity. Two such approaches follow.

#### 1.4.3.2. Structural equation modelling

SEM (also known as *path analysis*) is basically an extension of the above linear model, with the addition of a temporal dimension, and an assumption of statistical independence between time steps. This involves the specification of a statistical model to describe an observed physical system, and the minimization of error in a goodness-of-fit statistic, which measures the difference between the model prediction and empirical evidence (i.e., between their patterns of variance and covariance) (McIntosh and Gonzalez-Lima, 1991; Penny et al., 2004). For a connected brain network, this involves constructing a graph model whose

directed edges are constrained by structural connectivity, as assumed on the basis of previous experimentation. Subsequently, the connection strengths (i.e., synaptic efficacy) can be treated as free parameters, which can be manipulated so as to minimize the goodness-of-fit error. Additionally, external inputs, representing residual variance not explained by the model, can be included in the minimization. The connection strength covariance matrix which serves as the fitting constraint represents functional connectivity, so SEM can be intuited as an integration of structural and functional connectivity to infer causality, which is possible because the connections are unidirectional.

### 1.4.3.3. *Dynamic causal modelling*

DCM combines a small-scale, biophysically plausible forward model with a statistical framework facilitating model inversion (i.e., parameter fitting) and comparison (see (Daunizeau et al., 2009) for review). This is a potentially much more powerful means of estimating effective connectivity, given a sound model formulation, because it allows manipulation of the underlying (“latent”) neurodynamics, rather than the observables, as is the case with SEM (Penny et al., 2004). The general form of a DCM model is a set of ordinary differential equations (ODEs) which describe the rate of change of the system’s state,  $x$  (after (Daunizeau et al., 2009)):

$$\dot{x} = f(x, u, \theta)$$

where  $u$  represents experimental manipulations (e.g., external input), and  $\theta$  represents free (unknown) *system* parameters (e.g., synaptic strengths). Since  $x$  typically represents some hidden system state, such as the mean neuronal firing rate or local field potential, an additional transfer function (or *observation equation*) is usually necessary, mapping from the hidden state to some observable signal, such as BOLD or EEG:

$$y = g(x, \varphi)$$

where  $\varphi$  represents free (unknown) *observation* parameters (e.g., describing volume conduction in scalp EEG). The DCM can then be constructed as a graph (see Section 1.4.5), with each vertex representing an element of  $x$ , and each edge representing a causal relationship, the nature of which is determined by the parameters  $\theta$ . The vertices can then assume states which evolve at discrete time points, generating a simulated signal through  $y$ .

DCMs are generally set in a Bayesian statistical framework. This form allows the incorporation of prior knowledge, including known biophysical constraints on parameters (e.g., the presence or absence of anatomical connections, or the range of values a parameter can plausibly assume). The Bayesian framework for a DCM  $m$  is characterized by (1.) the marginal likelihood, or *model evidence*:

$$p(y | m) = \int p(y | \vartheta, m) \cdot p(\vartheta | m) d\vartheta$$

where  $\vartheta$  represents both sets of parameters  $\theta$  and  $\varphi$ , from above; and (2.) the *posterior probability density*:

$$p(\vartheta | y, m) = \frac{p(y | \vartheta, m) \cdot p(\vartheta | m)}{p(y | m)}$$

The model evidence represents the probability of a set of observations  $y$  (e.g., fMRI signals), given a specific model  $m$ , by generating simulations of  $y$  over all possible parameter values. In practice, this involves sampling over their distributions, or by using an optimization

approximation called a *variational Bayesian* technique (Penny et al., 2003). It can be used to compare between distinct model formulations (i.e., different versions of the function  $f$ , above). The posterior probability can be used to make inferences about model parameters  $\vartheta$  (e.g., what happens when we modulate synaptic connectivity with serotonin?).

#### 1.4.4. Cortical Hierarchies

In the early 1960s, David Hubel and Thorsten Wiesel undertook a series of electrophysiological experiments investigating the structural and functional organization of the cat visual system (Hubel and Wiesel, 1959). They reported that neurons in striate cortex had a very specific preference to fire in response to visual stimuli which included *contrast* (i.e., the borders between dark and light regions). These cells could be further classified on the basis of the *orientation* of the edge to which they responded, a property referred to as *orientation tuning*. Moreover, these orientation-specific cells were arranged into columnar groups across the striate cortex, in a topological fashion corresponding to the small retinal receptive field from which they received input. These orientation-tuned cells with small receptive fields were termed "simple cells". Other neurons were found to have a similar orientation specificity, but much broader receptive fields (i.e., they demonstrated a larger degree of *spatial invariance*). Still other neurons responded specifically to *movement* in a particular direction. Due to the relative complexity of these response properties, and the hypothesis that their inputs comprised an integration of simple cell outputs, these latter types of neuron were termed "complex cells".

Further investigation of the visual system extended into anatomical regions beyond striate cortex, including V2, V3, V4 and MT. Hubel and Wiesel found no evidence of simple cells beyond striate cortex, but did find complex cells, similar in their response patterns to those of V1, as well as neurons with more elaborate characteristics, which they termed "hypercomplex cells". These cells had generally very broad receptive fields, but were specific for stimulus properties such as width, length, orientation of movement, and other "higher-order" spatial and temporal patterns.

One of the conclusions that may be drawn from this important body of research is that the visual cortex is potentially organized in a distinctly hierarchical fashion, such that neurons which receive information directly from sensory inputs code for very simple stimulus properties (such as retinal position and edge orientation), and this coded information is relayed to higher-level neurons which code in turn for more complex features. This perceptual hypothesis implicates a division of labour that provides an intuitive explanation for the patterns of connectivity in the early visual cortex, and suggests that such a hierarchical system may indeed be an organizing principle of the entire neocortex.

In the late 1970s and early 1980s, the notion arose that anatomical measurements could be utilized as a criterion for establishing a hierarchy of cortical regions. In particular, the laminar source and target distributions of interregional projections were observed to correspond to the feedforward, lateral, and feedback relationships of the connected regions (Maunsell and Van Essen, 1983) (see Figure 1.7). In 1991, Daniel Felleman and David Van Essen systematically investigated this notion, by compiling a large body of tract tracing evidence, and applying this as a constraint on the delineation of a full cortical hierarchy of the visual system, including 32 cortical areas, and 318 of the 992 possible pairwise hierarchical relationships between them. This resulted in a comprehensive wiring diagram

## Introduction

of the visual system (see Figure 4, (Felleman and Van Essen, 1991)), which is still widely employed within the field of neuroscience.

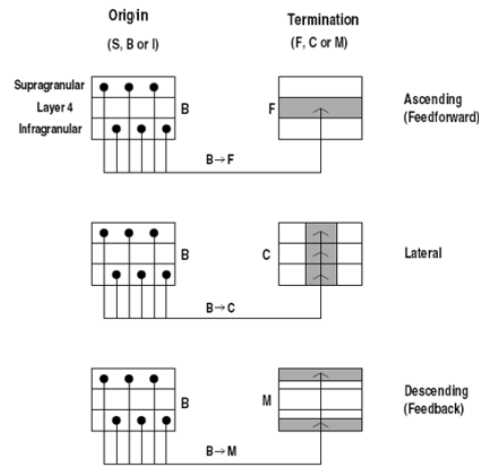


**Figure 1.7.** Projection-based constraints for determining hierarchical relationships, from Felleman and Van Essen (1991).

Two major criticisms of the Felleman and Van Essen hierarchy, however, are: (1.) that it requires eight violations of the anatomical constraints, and (2.) that it is chosen, somewhat arbitrarily, by the authors, from a model space on the order of  $10^{37}$ . To address these issues, (Hilgetag et al., 1996) developed a genetic algorithm approach, producing 150,000+ unique hierarchies which had less constraint violations than the original (six instead of eight). While the position of cortical regions at the bottom of the hierarchy (V1, V2, etc.) remained fairly stable across hierarchies, the higher regions varied greatly, suggesting a possibly inherent indeterminacy in this sort of determination.

However, a number of developments in neuroanatomical research have changed the picture somewhat. Firstly, the observation that laminar source and termination patterns cannot only predict the direction, but also the relative hierarchical *distance* of a projection (i.e., how far apart the connected regions are in the hierarchy) (Kennedy and Bullier, 1985; Barone et al., 2000; Batardière et al., 2002; Hilgetag and Grant, 2010), suggests that new constraints can be applied to the optimization. Secondly, extending this even further, if cells labelled from a retrograde tracer are counted, the proportion of cells in the supragranular layers, to the total number of cells, can yield a real-valued estimate of the relative hierarchical distance, called the SLN% (Barone et al., 2000). Furthermore, while previous representations have chosen to set cortical regions on discrete hierarchical levels, there is no apparent reason why regions should be classified in this way. My colleagues and I (Reid et al., 2009) have proposed a new hierarchical optimization scheme, using continuous values rather than discrete levels, and ranges to represent hierarchical distance. These methods are described in Section 4.1.

### 1.4.5. Graph Theoretical Approaches

Brain networks can be conveniently represented as directed graphs, with brain regions as graph nodes and their projections as directed edges connecting these nodes. Graphs are

particularly well-suited to investigations of structural brain connectivity, as they permit the application of graph theoretical analyses to these networks. Below I introduce, as exemplars, three common graph theoretical measures which are currently used to investigate the structural characteristics of brain networks. For this purpose, it is useful to first define a few graph theoretical concepts: (1.) graph, vertex, and edge; (2.) directed graphs; (3.) weighted graphs; and (4.) paths:

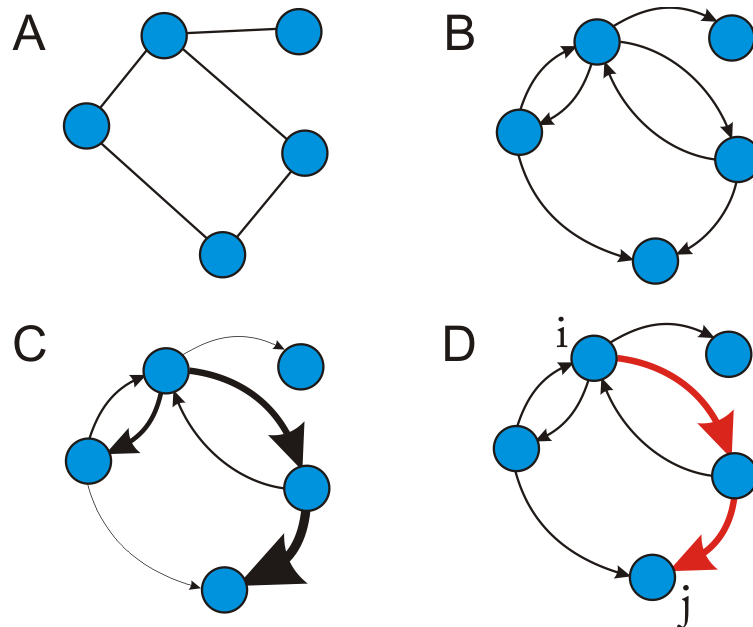


**Figure 1.8.** Various graph representations. *A:* undirected, unweighted graph. *B:* directed graph. *C:* directed, weighted graph. *D:* red edges show a directed path of length 2 from vertex  $i$  to vertex  $j$ .

#### i. Graph, vertex, and edge

A graph  $G$ , is defined by a set of vertices  $V$ , and a set of edges  $E$ , where each edge defines a link between two vertices in  $V$ . Figure 1.8A shows a simple graph with five vertices and five edges.

#### ii. Directed graphs

A *directed graph* is one that contains directed edges, designated with an arrow on one end. Directed edges depict unidirectional relationships (e.g., causality, axonal connections, etc.). Figure 1.8B portrays a directed graph.

#### iii. Weighted graphs

A *weighted graph* is one for which edges have a set of associated values, or weights. Edge weights allow concepts such as connection strength or distance to be represented in a graph (for a neural network or a geographical graph, respectively). Figure 1.8C portrays a weighted, directed graph.

#### iv. Paths

A *path* can be defined as a sequence of edges (and the vertices they connect) through which two vertices  $i$  and  $j$  ( $i, j \in G$ ) can be connected. A path must be

acyclic, meaning that it cannot contain a vertex more than once. The term *shortest path* denotes the set of unique paths between  $i$  and  $j$  in  $G$ , which have the fewest number of vertices. Figure 1.8D portrays a shortest path between two vertices.

#### 1.4.5.1. *Small worldness*

*Small worldness* is the property of a network in which any one of its vertices is connected to any other of its vertices via a small number of intervening vertices (i.e., relative to what would be expected from a randomly connected network). As first demonstrated by the social psychologist Stanley Milgram (Travers and Milgram, 1969), human social networks demonstrate this property (often referred to as “six degrees of separation” or “six degrees of Kevin Bacon”, depending on who you ask). Cortical networks have also been demonstrated to have small worldness (Sporns et al., 2000, 2007; Sporns and Honey, 2006), and this can be used as a measure of network efficiency (how well a network transmits information), which has been reported to decrease, for instance, in multiple sclerosis patients (He et al., 2009). Duncan Watts and Steven Strogatz (Watts and Strogatz, 1998) introduced two formal criteria and a canonical model to define small worldness: relative to a random graph (as defined by (Erdős and Rényi, 1959)), it must demonstrate (1.) an equal or smaller *mean shortest path length*; and (2.) a significantly higher *clustering coefficient*. This can be formulated more precisely as follows (after (Watts and Strogatz, 1998; Humphries and Gurney, 2008)):

##### i. **Mean shortest path length**

For a directed, unweighted graph  $G$ , the shortest path length  $x_{ij}$  between vertices  $i$  and  $j$  ( $i, j \in G$ ) is the path with the fewest number of intervening vertices. The *mean* shortest path length  $L_G$ , then, is the mean over all node pairs  $(i, j)$ :

$$L_G = \frac{\sum_i^n \sum_j^n x_{ij}}{n(n-1)}, (i \neq j)$$

##### ii. **Clustering coefficient**

The clustering coefficient  $c_i$  of vertex  $i$  ( $i \in G$ ) represents the degree to which  $i$ 's neighbours are interconnected. This can be calculated as:

$$c_i = \frac{2E_i}{k_i(k_i - 1)}$$

where  $E_i$  is the number of connections between  $i$ 's neighbours, and  $k_i$  is the number of neighbours.  $C_G$ , the clustering coefficient of graph  $G$ , is then the mean  $c_i$  over all vertices.

##### iii. **Small worldness**

Since small worldness is defined with respect to random graphs, we can get a measure of small worldness by taking ratios of ratios:

$$\gamma_G = \frac{C_G}{C_{rand}} \quad \text{and} \quad \lambda_G = \frac{L_G}{L_{rand}}$$

where  $C_{rand}$  and  $L_{rand}$  are derived from a random graph, and:

$$S_G = \frac{\gamma_G}{\lambda_G}$$

$G$  can be considered small world if  $S_G > 1$ .

#### 1.4.5.2. *Betweenness centrality*

*Betweenness* is a measure of a vertex's *centrality* in a network; in other words, how well-connected it is on average to all other vertices in the network. Centrality has been used in social networks to measure a person's importance for communication within that network (Freeman, 1978), and high centrality is an important property of a "hub" node, such as can be found in computer, airport, and brain networks. Betweenness refers specifically to the frequency with which a vertex occurs in shortest paths between two other vertices (Freeman, 1977; Brandes, 2001). For the simplest case of an undirected, unweighted graph, it can be defined more formally as follows (after Brandes, 2001):

Given an undirected, unweighted graph  $G$ , and two vertices  $i$  and  $j$  ( $i, j \in G$ ), we can define  $\sigma_{ij}$  as the number of *unique, shortest* paths between  $i$  and  $j$ . We can further define  $\sigma_{ij}(v)$  as the number of *unique, shortest* paths between  $i$  and  $j$  which include vertex  $v$  ( $v \in G$ ). Betweenness centrality, then, is simply the ratio of the number of shortest paths in  $G$  which contain  $v$ , with the total number of such paths. Formally, this looks like:

$$C_B = \sum_{i \neq v \neq j} \frac{\sigma_{ij}(v)}{\sigma_{ij}}$$

where  $C_B$  is the betweenness centrality measure.

## 1.5. Magnetic Resonance Imaging

Magnetic resonance imaging (MRI) is based upon the principle of nuclear magnetic resonance (NMR), which was first observed by Isidor Rabi in 1938, and employed by Felix Bloch and Edward Mills Purcell in 1946, for which the latter two shared the 1952 Nobel Prize in Physics. This principle was further applied to medical imaging by Paul Lauterbur and Peter Mansfield, which earned them the Nobel Prize in Physiology or Medicine in 2003.

It is difficult to overstate the importance of MRI to both modern neuroscientific research and clinical practice. Depending on the contrast and acquisition protocols used, MRI allows a visualization of the structural details or functional activation of the *in vivo* human brain, at an impressive spatial resolution that promises to improve as higher magnetic field strengths are employed. MRI, moreover, is completely noninvasive, and does not require exposure to potentially harmful radiation, as is the case with alternative methods such as x-ray computed tomography (CT) scanning. As MRI is the data acquisition method for the RUN-DMC data considered in this dissertation, this section provides an overview of the techniques and basic principles underlying MRI.

### 1.5.1. Basic Principles

#### 1.5.1.1. Nuclear magnetic resonance

NMR is a property observed in magnetic nuclei in a magnetic field: when radiated by an radio-frequency (RF) electromagnetic (EM) pulse of a specific *resonance frequency* (or *Larmor frequency*), these nuclei absorb energy from the pulse and radiate it back at rates which can be used to infer the composition of the medium containing them. A commonly-employed model of this phenomenon is: (1.) when nuclei are placed in an applied magnetic field  $H_0$ , a fraction of their magnetic spins become aligned with  $H_0$ ; (2.) when they are radiated by an RF pulse (with a frequency equal to the Larmor frequency for a target particle), these spins become momentarily misaligned, creating a thermal nonequilibrium state; and (3.) after cessation of the RF pulse, misaligned nuclei “relax”, or return to their thermal equilibrium states, at measureable rates from which time constants can be derived. Relaxation occurs as two separate physical processes: (1.) parallel to the orientation of  $H_0$ , called *spin-lattice relaxation time* (with the associated time constant  $T_1$ ); and (2.) perpendicular to it, called *spin-spin relaxation time* (with time constant  $T_2$ ). These are described below:

#### i. Spin-lattice relaxation time ( $T_1$ )

If we assign  $M_Z$  as the *net longitudinal magnetization vector* (the vector in the direction of  $H_0$ , resulting from the sum of spins in the medium being imaged), and  $M_0$  as the state of this vector under the uniform magnetic field  $H_0$  (i.e., the *equilibrium magnetization*), then after a sufficient RF pulse (a so-called  $90^\circ$  pulse, which rotates the net magnetization by  $90^\circ$ ), we have  $M_Z=0$  (indicating that all spins are misaligned with  $H_0$ ). The *spin-lattice relaxation time* describes the rate at which the spins realign to  $H_0$ . This relaxation towards the equilibrium magnetization is exponential (Figure 1.9, left), and can be described by the function:

$$M_Z(t) = M_0 \cdot (1 - e^{-t/T_1})$$

## ii. Spin-spin relaxation time ( $T_2$ )

When spin vectors are not aligned with the longitudinal axis of  $H_0$ , their behaviour is characterized by *precession*, which is analogous to the behaviour of a spinning top rotating in a gravitational field. A  $90^\circ$  RF pulse causes the phases of the precessing spin vectors to align in the transverse (XY) plane, resulting in a nonzero *net transverse magnetization vector*  $M_{XY}$ . As the system relaxes, however, the phases of its spin vectors fall out of alignment, until  $M_{XY}$  approaches its equilibrium state of zero. Spin-spin relaxation takes the form of an exponential decay (Figure 1.9, right), described by the function:

$$M_{XY}(t) = M_{XY}(0) \cdot e^{-t/T_2}$$

Notably, the rate of decay is dependent upon two factors: (1.) molecular interactions, which are the phenomena of interest, and whose net effect is typically referred to as the true  $T_2$  signal; and (2.) local inhomogeneities in the magnetic field within a voxel, which are typically considered noise. The measured signal is a combination of these factors, and is referred to as  $T_2^*$ .

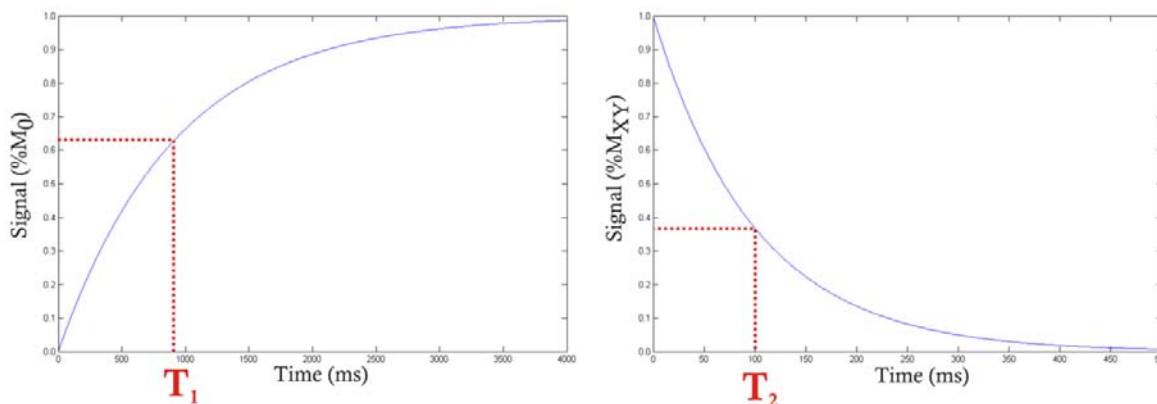


**Figure 1.9.** NMR signal relaxation profiles with typical time constants for cortical grey matter. **Left:** spin-lattice relaxation ( $T_1 = 920\text{ms}$ ). **Right:** spin-spin relaxation ( $T_2 = 100\text{ms}$ ).

### 1.5.1.2. Field gradients

Because the resonance frequency of a particle is proportional to the magnetic field strength, a gradient set up across the field can be used to determine the *position* of a signal source produced by NMR. The three-dimensional localization of an MR acquisition can be accomplished in two steps: (1.) a linear, one-dimensional gradient  $G_Z$  is established in the longitudinal direction, during the RF pulse. Since the resonance frequency required to flip a particle's spin is dependent upon the field strength, only particles within a small corridor of the field will absorb the EM energy, and longitudinal position of this corridor can be controlled by the pulse frequency. In general, this is called the *slice-selecting gradient*, denoted  $G_S$ . (2.) A linear, one-dimensional gradient  $G_X$  is established in the transverse direction during signal acquisition (in this case, the x direction). This ensures that particles will have differential resonance frequencies during their relaxation period, which correspond

## Introduction

to their positions with respect to the orientation of  $G_x$  (i.e., their x position).  $G_x$  (generally  $G_f$ ) is thus called a *frequency-encoding gradient*. A second gradient can now be used to encode the y direction, called the *phase-encoding gradient*  $G_y$  (generally  $G_\phi$ ).  $G_y$  is applied for a duration prior to signal acquisition and then removed, resulting in a systematic offset of the phases of the precessing magnetization vectors; if  $G_y$  is changed across  $n$  repeated acquisitions, this offset can be used to determine the signal's y position. The dimensionality of y will thus be  $n$ . This determination is obtained through Fourier analyses, which will not be elaborated here.

### ***1.5.1.3. Acquisition protocols***

Since the values of  $T_1$  and  $T_2$  are dependent on the composition of the medium being imaged, their values can be used to weight voxel intensities in the resulting image, and the contrast between voxels can be used to differentiate between tissue classes. Since the desired contrasts obtained by an MRI protocol vary depending on the research or clinical question (e.g., grey matter, white matter, cerebrospinal fluid, strokes, lesions, or tumours), a variety of acquisition protocols have been developed which maximize contrast between particular tissue types (i.e., weighting on one or the other of these time constants). These are typically extensions of two basic protocols: (1.) gradient echo, and (2.) spin echo; where “echo” refers to a means of amplifying a signal by arranging for an alignment of spin phases at a specific time called the *echo time* (TE).

### ***1.5.2. Diffusion-Weighted Imaging***

Diffusion-weighted imaging (DWI) is a modification of the MR acquisition protocol, which allows the quantification of molecular diffusion in the brain. Since diffusion occurs maximally along directed fibers, DWI has been used to image the distribution and integrity of white matter tracts in the human brain, and thus has a very promising potential for connectivity research, as well as myriad clinical applications.

#### ***1.5.2.1. Principles***

DWI derives from the observation that particles, such as water molecules, move in a random fashion called *Brownian motion*. In an isotropic medium, any one molecule may be displaced significantly over a duration  $\Delta t$ , although the net displacement of molecules will have a magnitude of zero. This diffusion of individual molecules can be detected by MRI. Following work by Stejskal and Tanner (Stejskal and Tanner, 1965), this is accomplished by adding two new strong gradient pulses to the acquisition sequence, equal in magnitude and duration, but opposite in direction. This sequence will have the effect of dephasing and then rephasing the spins of the particles, such that the net phase shift should be zero; however, if the particle is displaced along the gradient direction during the pulses, its net phase shift will most likely be *nonzero*. The average of these nonzero phase shifts will result in a reduced phase coherence, and a drop in the measured signal. The average rate of diffusion in a given voxel, then, can be inferred from the signal drop induced by this gradient pulse sequence. The resulting value is called the apparent diffusion coefficient (ADC).

#### ***1.5.2.2. Diffusion tensor imaging***

The anisotropic diffusion of water through white matter was first reported by Michael Moseley (Moseley et al., 1990), who reported that ADC derived from this tissue was dependent upon the gradient direction, relative to the orientation of the white matter tract.

This led to the idea that diffusion could be represented as a tensor, by acquisitions using three or more gradient directions. A tensor specifies a geometric ellipsoid, whose orientation and anisotropy can serve as a model for the diffusion of water molecules. For each gradient direction, the gradient can be represented by a vector  $\mathbf{q}$ , oriented with the direction of diffusion, and having a magnitude equal to the gradient field strength. The diffusion weighted image is typically specified using the weighting factor  $b$ :

$$b \sim q^2 \cdot \Delta$$

where  $q$  is the magnitude of  $\mathbf{q}$ , and  $\Delta$  is the duration between the onset of the two gradient pulses.

The resulting imaging protocol, called *diffusion tensor imaging* (DTI), meant that MRI could yield information not only about the rate of diffusion in tissue, but also the degree of anisotropy (a measure called *fractional anisotropy*, or FA), and the magnitudes and directions of anisotropic diffusion (reviewed in (Le Bihan, 2003)).

### 1.5.2.3. *Q-ball and persistent angular structure imaging*

One problem with the tensor model described above is that a single ellipsoid (representing a single Gaussian distribution) is often an inadequate model for diffusion, particularly in voxels where fibers may be crossing one another, bending, or twisting within the voxel. This is only partially improved by adding additional tensor models (a so-called multi-tensor model), since typically only two principle directions are represented in this way (Parker & Alexander, 2005). An alternative approach was proposed by David Tuch and colleagues (Tuch et al., 1999; Tuch, 2004), who suggested that a tessellated sphere called a *q-ball* could be used, in conjunction with a larger number of gradient angles.

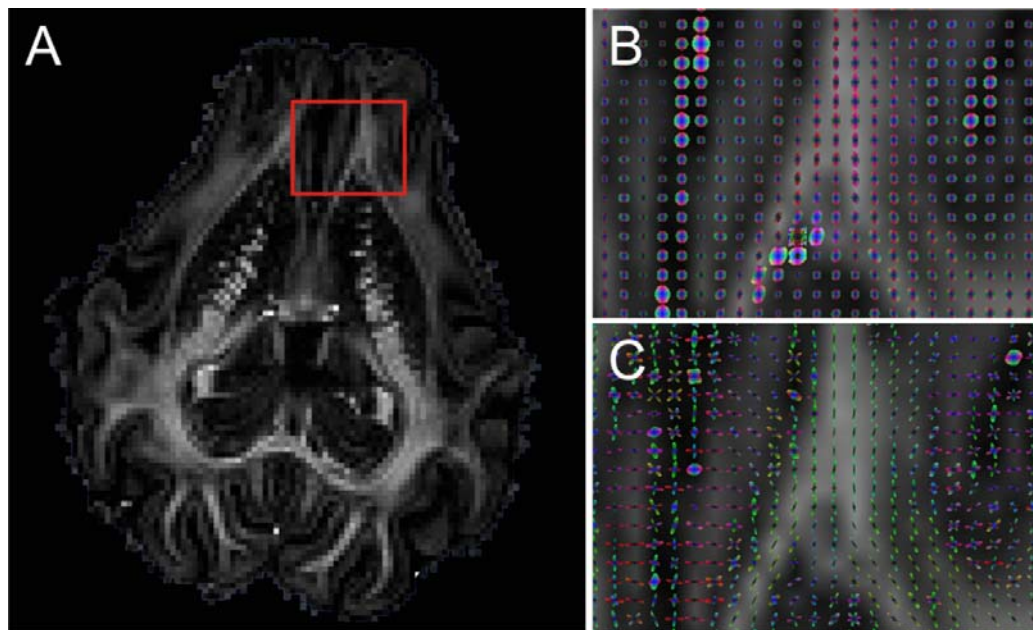


**Figure 1.10.** Diffusion-weighted imaging of a pig brain shown in horizontal section, obtained using Camino software. **A:** Fractional anisotropy (FA) map. Red box indicates the region magnified at right. **B:** Orientation distribution functions (ODFs), calculated with the persistent angular structure (PAS) model. **C:** Multi-tensor model of the same data.

For a given gradient direction, the gradient field can be represented by a wavevector  $\mathbf{q}$ :

$$\mathbf{q} = (2\pi)^{-1}\gamma\delta\mathbf{g},$$

where  $\gamma$  is the gyromagnetic constant,  $\delta$  is the duration of each diffusion gradient pulse, and  $\mathbf{g}$  is the diffusion gradient vector (Tuch, 2004). Thus,  $\mathbf{q}$  is oriented with the direction of diffusion, and has a magnitude proportional to the net diffusion in that direction.

*Q-ball imaging*, as this approach is called, is based upon *high-angular-resolution diffusion imaging* (HARDI), in which acquisitions are taken with gradient fields of many orientations, such that each vertex of the q-ball can be specified by the  $\mathbf{q}$  vector corresponding to a particular orientation. Q-ball imaging, and a similar method called persistent angular structure (PAS-) MRI (Jansons and Alexander, 2003), provide a model-free estimation of an *orientation probability distribution function* (ODF), which allows a much more comprehensive representation of diffusion, and is thus a very useful means of quantifying the microstructural features of white matter within a voxel. An example of these ODFs is shown in Figure 1.10.

#### 1.5.2.4. Tractography

One of the most obvious utilities of tensor, q-ball, and PAS imaging are their use in the *tractography* of white matter tracts. Tractography is a method of estimating the trajectory of a fiber tract using voxel-wise orientation information. This involves starting the tract at some *seed region*  $S$ , and estimating its new direction after passing through a series of voxels, until some stopping criterion is met. For a DTI voxel, this typically means following the single eigenvector specifying the orientation of the ellipsoidal Gaussian distribution (Figure 1.11A). Tractography can be performed once, or it can make use of the modelled probability distributions by performing multiple runs, sampling from each voxel-wise ODF on each run, a form of tractography called *probabilistic tractography*. Probabilistic tractography can also be performed with the use of *target regions* (regions in which tracts must terminate) or *waypoints* (regions through which tracts must pass), in order to investigate specific questions about connectivity. Since q-ball and PAS imaging provide a model-free ODF with a far superior representation of directional information, compared to DTI, their advantage for probabilistic tractography is obvious (Parker and Alexander, 2005) (Figure 1.11B).

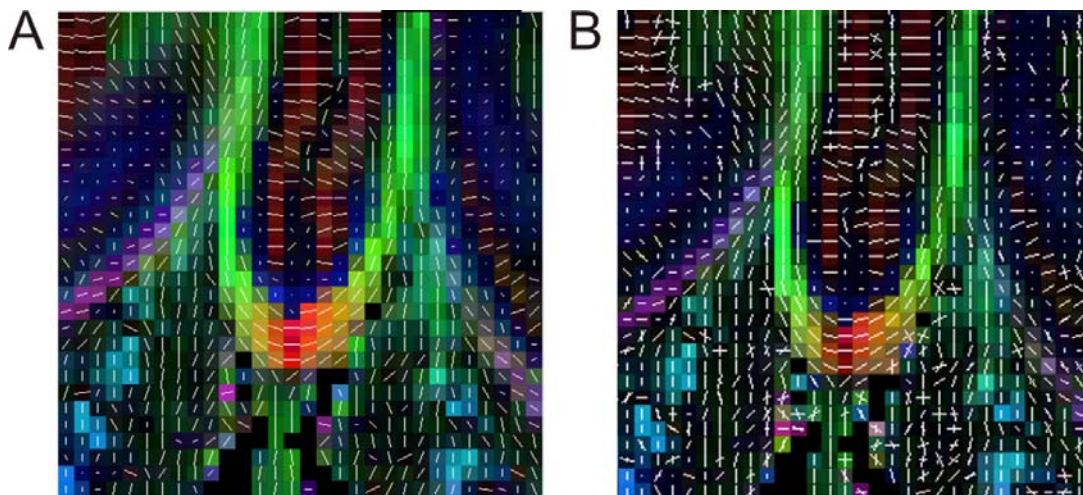


**Figure 1.11.** DWI-based tractography (images obtained using Camino software). **A.** Principle eigenvector obtained from a diffusion tensor model. The background is coloured by FA. **B.** Fiber-orientation estimates for the same data, obtained from q-ball ODFs. The background is coloured by a Hessian-derived estimate of the peak sharpness for a given ODF.

## 1.6. Human Brain Morphometry

*Whoever would not remain in complete ignorance of the resources which cause him to act; whoever would seize, at a single philosophical glance, the nature of man and animals, and their relations to external objects; whoever would establish, on the intellectual and moral functions, a solid doctrine of mental diseases, of the general and governing influence of the brain in the states of health and disease, should know, that it is indispensable, that the study of the organization of the brain should march side by side with that of its functions.*

–Franz Joseph Gall, *On the Organ of the Moral Qualities and Intellectual Faculties, and the Plurality of the Cerebral Organs* (Gall, 1835).

Gall was a German-born physician and neuroanatomist whose chief scientific interest was the establishment of a general mapping from the human brain's morphology to its functions. In 1909, based upon a series of poorly-controlled experiments, Gall, along with his protégée Johann Gaspar Spurzheim, published an atlas of the human cortex called *Anatomie et physiologie du système nerveux en général, et du cerveau en particulier*. Perhaps the most notable of their assertions was that the shape and size of a person's skull, which was assumed to correlate with the neural tissue beneath it, could be used to determine that person's disposition and character; and, by extension, predict his or her probable behaviour. Although these assertions, which led to the field of *phrenology* and for a time enjoyed immense popularity, have been roundly rejected by the scientific community for lack of any sound empirical basis, they were perhaps the first such attempt at relating brain morphometry (the geometric measurement of neural tissue) to its function.

With the advent of noninvasive, high contrast, high spatial resolution, *in vivo* brain imaging, brain morphometry has once again become a prominent field of scientific inquiry. Image processing techniques allow the estimation, for instance, of brain volume and density, as well as cortical thickness and white matter integrity. As such morphometric techniques are utilized in the current dissertation, they are outlined in this section. Although I am not so bold as to follow in the footsteps of Gall and Spurzheim, I do believe that these new, more direct investigations of living human brains might also be used to illuminate the functions – and the functional deficits – associated with localized cortical regions of interest. Such ideas will be more broadly considered in the Discussion.

### 1.6.1 Voxel-based Morphometry

Voxel-based morphometry (VBM) is the estimation of volumetric measures of brain shape or composition, based upon a brain image (see (Ashburner and Friston, 2000)). Such measurements rely upon the relationship of an individual image with a template image, constructed from a large number of individuals (see Section 1.3.4). VBM involves a number of steps: (1.) normalization of the subject image to the template image; (2.) intensity-based tissue classification; (3.) spatial smoothing; and (4.) statistical comparisons, resulting in a voxel-wise statistical parametric map (SPM).

Spatial normalization for VBM typically uses a 12-parameter affine transformation, which removes gross individual shape differences such as head orientation and global size, but preserves the local idiosyncrasies which are of interest. Tissue is classified depending on the question of interest, typically into grey matter (GM), white matter (WM), or cerebrospinal fluid (CSF) compartments. Smoothing involves a voxel-wise convolution with a Gaussian kernel, which effectively accumulates information contained by a voxel's spatial

## Introduction

neighbourhood, with a normal distribution that makes it statistically comparable to corresponding voxels in other images. The resulting value is referred to as either *density* or *concentration* (Ashburner and Friston prefer the latter term, as it distinguishes this value from that of *cell-packing density*, used in histology). The shape of the kernel (i.e., its variance component) should correspond to the magnitude of the expected differences under investigation.

An SPM is obtained by performing an independent statistical analysis for each voxel in specific tissue compartment, typically a general linear model (GLM), which can assess the effects of experimental manipulations or population demographics upon morphology. Since this usually involves performing thousands of statistical comparisons, it entails the accumulation of a large amount of family-wise error (FWE). Methods for addressing this problem are discussed in Section 2.1.9.

### ***1.6.2. Surface-based Morphometry***

Given that the neocortex is formed as a convoluted sheet with a certain thickness, it can be represented as a 3D surface mesh (or two-manifold), from which a number of geometric measures can be derived. A number of imaging algorithms have been developed for this purpose, most of which derive from 2D image processing methods. The “Snake model” (Kass et al., 1988), for instance, is a 2D method which utilizes a deformation polyline to estimate the boundaries in an image. In general, the goals of a surface approximation algorithm are: (1.) segment the image to define the boundaries of interest; (2.) define optimization constraints with which to guide the deformation of an approximating manifold; (3.) deform the manifold until it fits with an acceptable level of error (or fails). This procedure, in particular the CLASP routine used in this dissertation, is described in 2.1.7. The statistical analysis of vertex-wise effects is similar to that performed in VBM; i.e., independent vertex-wise GLMs are analyzed. This involves the same issue of FWE.

Analysis of cortical thickness is likely more sensitive to anatomical changes than VBM approaches (Apostolova and Thompson, 2007; Hutton et al., 2009), and distinct patterns of cortical thinning have been observed in Alzheimer’s Disease (AD) (Apostolova et al., 2007; Lerch et al., 2005), schizophrenia (Narr et al., 2005), and aging (Salat et al., 2004), to name only a few. Within longitudinal designs, cortical thickness has also been used to produce dynamical maps of both the development of cortex and corresponding language skills and the deterioration of cortex in AD. Such representations are also very useful for additional geometric measures such as sulcul depth, mean curvature, and surface area.

## 1.7. The Aging Brain

The notion that the functionality of the human brain decreases with old age is more or less a matter of common knowledge. This degradation includes many varieties of information processing, including “speed of processing, working memory capacity, inhibitory function, and long-term memory” (reviewed in (Park and Reuter-Lorenz, 2009)). However, the patterns of such function loss are by no means clear, nor uniform across the population. Aging is a process which affects individuals in individual ways, which are attributable both to genetics and experience; this is evident from anecdotal observations ranging from male pattern baldness, female menopause, hearing and vision loss, and memory loss, to more severe pathological conditions such as Alzheimer’s Disease and other dementias, Parkinson’s Disease, vascular degeneration, strokes, hypertension, etc. Given both an increasingly elderly population, and a growing set of methodological tools including functional neuroimaging techniques, such degenerative patterns are being investigated with increasing intensity. What follows is a brief review on our current state of knowledge about the aging brain.

### *1.7.1. Neurological and Cognitive Correlates*

#### *1.7.1.1. Memory*

The age-related neural correlates of memory (typically working memory) have been well studied using various fMRI paradigms (see (Grady, 2008), for review). While specific effects differ according to the exact paradigm used, a consistent overactivation of the left prefrontal cortex (PFC) has been observed in elderly subjects (compared to younger subjects), corresponding to an increase in task performance (Dennis et al., 2007; Grady et al., 2008). Daselaar and colleagues (Daselaar et al., 2006) report a dissociation between hippocampal and parietotemporal activity in older adults who perform as well as younger ones, with an increase in associativity between rhinal and frontal cortex. These effects have been proposed as means of compensating for decreased hippocampal function, or attentional focus, in older subjects. Such compensation, however, may have its limits in the form of working memory load. Using an  $n$ -back paradigm, which allows working memory loads to be manipulated, Mattay and colleagues (Mattay et al., 2006) observed an overactivation of dorsolateral PFC bilaterally, in older adults who performed as well as their younger counterparts on a one-back task, but this activation disappeared as the task became more difficult, and there was a corresponding drop in performance for older subjects.

#### *1.7.1.2. Executive function*

Studies of attention have also generally reported altered PFC activity in tasks requiring inhibition of distractor stimuli. Compared with younger subjects, PFC activation appears to be generally decreased for elderly adults (Jonides et al., 2000), but increased in those who successfully inhibit the distractor (Nielson et al., 2002). In a separate study, performance on two cognitive inhibition tasks presumed to require executive control, Stroop interference and stop signal responsiveness, significantly decrease with age, whereas performance on a non-executive cognitive inhibition task does not show a similar decrease (Andrés et al., 2008). Since executive function (i.e., task engagement) has been shown to involve a suppression of so-called “default mode” network activity (Weissman et al., 2006; Fransson, 2006), this suppression has also been used as a measure of cognitive control. Such task-related suppression is reportedly reduced in older adults (Grady et al., 2006; Damoiseaux et al.,

2008), and this effect has been shown to be proportional to task load: in low difficulty versions of a verb generation task, older subjects performed equally well as younger, and their default mode suppression was similar; however both relative performance and default-mode suppression decreased with increasing cognitive demand (Persson et al., 2007).

### ***1.7.2. Structural Correlates***

#### ***1.7.2.1. White matter***

The relationship of age with the integrity of white matter (WM) has been studied from a number of angles. Notably, in individuals aged 60 to 90 years, the prevalence of some degree of WM lesions (WML) has been reported at 95% (de Leeuw et al., 2001). Moreover, periventricular WML severity is related to a factor-of-three increase in the rate of general cognitive decline for this same age group (De Groot et al., 2002). Aging has been linked specifically to a reduction of myelin, or myelinated fibers (Meier-Ruge et al., 1992), and age-related WM degeneration, while global, appears to strongest in prefrontal areas (Jernigan et al., 2001), corpus callosum (Pfefferbaum et al., 2000), and periventricular areas (Nusbaum et al., 2001). Salat and colleagues (Salat et al., 2005) used DWI techniques to investigate the relationship of fractional anisotropy (FA) with age, and report a negative linear correlation of global FA with age across the most of the human life span (age 20 to 80). This effect was heterogeneous across the brain, being most prominent in prefrontal areas and posterior limb of the internal capsule (PLIC), while not significant in temporal or posterior regions. Other evidence suggests that prefrontal WM volume degenerates at a higher rate than cortical GM, particularly in adults over 75 (Salat et al., 1999).

#### ***1.7.2.2. Grey matter***

Given the theoretical localization of function within the cortex, one might expect that the specific patterns of cognitive deficits described above would have some correlates in cortical grey matter (GM) integrity. Dekaban (Dekaban, 1978), obtained brain weight measurements by compiling a large number of pathology reports, and concluded a general age-related decrease in weight, correcting for height. At a finer scale, a number of post-mortem experiments investigating neuron counts have demonstrated an age-related decline occurring more prominently in association cortex than in primary sensory cortex (Flood and Coleman, 1988). One caveat of such comparisons is that they are typically made between separate studies employing different methodologies, often resulting in contradictory findings. Moreover, the use of post-mortem human tissue, in addition to having a number of methodological drawbacks which are difficult to control (Good et al., 2001), is also limited in its ability to accurately describe the living brain.

Recent advances in MR imaging techniques have allowed for high-resolution in vivo analysis of age-related GM alterations. In particular, voxel-based morphometry (VBM; see Section 1.6.1) facilitates a volumetric analysis (typically reported in terms of tissue volume or density) of living brain tissue, providing reasonably constrained tissue classification, region-of-interest parcellation, and inter-subject comparisons (Ashburner and Friston, 2000). Using VBM, Raz and colleagues (Raz et al., 1997, 2004) report a general non-uniform age-related decrease in grey matter (GM) volume which is most prominent in lateral prefrontal cortex, and less so in sensorimotor and visual association cortices, while finding no age-related changes in primary visual, anterior cingulate, or inferior parietal cortices. Good and colleagues (Good et al., 2001) report a global age-related linear decrease in GM volume,

which is most pronounced bilaterally in the superior parietal gyri, pre- and post-central gyri, and insula/frontal operculum. An age-related decrease in GM density was also observed in the left middle frontal gyrus, bilateral transverse temporal gyri, and the left planum temporale. Sowell and colleagues (Sowell et al., 2003) found a non-linear decline in GM density with age, particularly in posterior temporal and inferior parietal cortices.

An alternative MR-based morphometric approach is that of cortical GM thickness analysis, which is based upon a geometric approximation to the boundaries of cortical GM (see Section 1.6.2). Cortical thickness analysis has been reported to provide a more sensitive measure of GM integrity than VBM (Hutton et al., 2009). Hutton et al. (2009) report a linear decrease of cortical thickness with age, for subjects aged 20 to 60 years. Salat et al. (Salat et al., 2004) investigated cortical thickness with respect to age across three age groups ranging from 18 to 93 years, and report a significant age-related cortical thinning, apparent from middle age, in prefrontal, primary motor, and calcarine cortices, and a relative sparing of temporal and parahippocampal cortex.

### ***1.7.3. Structure and Function***

Given the patterns of functional and structural changes observed in aging, it is desirable to find links between these patterns, which would provide valuable insights into their neuronal mechanisms. A number of researchers have pursued this line of inquiry. In an early study, Salat and colleagues (Salat et al., 2002) report a significant hypertrophy of the superior prefrontal cortex, which corresponded to decreased cognitive performance in elderly adults. Colcombe et al. (Colcombe et al., 2005) tested old and young subjects on a cognitive inhibition task, and observed an increased activation of left PFC for older subjects, which negative correlated with performance. Moreover, while these authors found no difference in GM density between good and poor performers, they did observe higher WM density for good performers in underlying frontal lobe and colossal fibers. While Gunning Dixon and Raz (Gunning-Dixon and Raz, 2003) similarly report a negative relationship WM hyperintensities (WMH, an MRI marker for demyelination) on the Wisconsin Card Sorting Test (a measure of “perseveration”, or the ability to adapt to changing task sets), they found no relationship between WMH and working memory. Investigations of the brain networks underlying these effects are equally informative. Achard and Bullmore (Achard and Bullmore, 2007), for instance, report a decreased network efficiency, indicated by graph theoretical measures, in older adults, particularly in orbitofrontal, lateral temporal, and medial temporal regions. Taniwaki et al. (Taniwaki et al., 2007) report an interesting decrease in functional connectivity for older adults in the basal ganglia-thalamus-motor cortex loop, but an increased interhemispheric connectivity between the motor cortices themselves.

### ***1.7.4. Compensation***

The term “compensation” has been used, often rather loosely, to refer to the observed changes in apparently compromised brain tissue, which are proposed to functionally compensate for the loss of function imposed by this compromise. In the cognitive paradigms mentioned above, for example, an localized increase in activity observed in older adults might raise the speculation of compensatory change; i.e., an increased recruitment of one part of the brain network in compensation for a deficient functionality in another part. Such an proposition was made, for instance, by (Daselaar et al., 2006), who noted a switch from

## Introduction

hippocampal-parietal encoding of memory, to a rhinal-frontal one. Grady (Grady, 2008) identifies two possible models of compensatory activation: (1.) the case in which older subjects have increased activation in a region which in younger subjects does not activate (i.e., so-called over-recruitment), and both show equal performance; and (2.) the stronger case where older adults show a differential pattern of brain activity, which is directed correlated with better performance.

*Dedifferentiation* refers to the idea that the over-recruitment of activation observed in older adults is due to decreased inhibitory processes, which normally suppress such activity. The result is a weakened ability to *differentiate* particular information streams, which is a form of attentional or concentration deficit. In support of this hypothesis, (Baltes and Lindenberger, 1997) investigated a large cohort of over 600 adults, aged 25 to 103, and found a strong connection between sensory functioning and cognitive ability, for both young and old individuals. Functionally, this theory may account for the increases in particularly bilateral PFC activation observed in older adults (for example (Reuter-Lorenz et al., 2000)). While on its face the dedifferentiation hypothesis would seem to predict a decrease in function related to such over-recruitment of activity, evidence suggests that this activity actually corresponds to increased cognitive performance in older adults (for example (Fera et al., 2005)). (Park and Reuter-Lorenz, 2009) present a “scaffolding theory” of aging, in which they propose that a normal neural mechanism exists for responding to extrinsic and intrinsic challenges. This primarily prefrontal mechanism supports learning (an extrinsic challenge) in younger individuals, gradually transferring common tasks to more specialized circuitry, while in older adults, whose specialized circuitry becomes compromised (an intrinsic challenge), the same system is recruited to compensate.

### **1.7.5. Small vessel disease**

A number of neurological pathologies are especially prevalent in older adults, among them Alzheimer’s Disease (AD), Parkinson’s Disease, neurovascular disease, and other forms of mild to severe cognitive impairment. The incidence of AD, for instance, rises dramatically with age, such that in the U.S. in 2000, ~5% of adults aged 65-74 had mild-to-severe AD, ~18% in adults aged 75-85, and ~45% in adults over 85 (Hebert et al., 2003). Given the expected increase in older adults over the next few decades, these prevalence rates, as a percentage of the total population, are expected to grow rapidly. In this dissertation, I focus on a common form of neurovascular pathology called cerebral microangiopathy, or cerebral small-vessel disease (SVD), which is a degeneration of small cerebral blood vessels whose common risk factors are age, hypertension, and possibly genetic factors (de Leeuw et al., 2002; Launer, 2003). SVD is a significant risk factor for age-related cognitive impairment and dementia (O’Brien, 2003), as well as gait impairment and behavioural, psychological, and somatic neurological symptoms (Schmidt et al., 2002; Schmidtke and Hüll, 2005). SVD may also have related morphological effects. At least one study of elderly individuals (mean age 58 years) has demonstrated a general decrease in cortical thickness for subjects with SVD compared to age-matched controls, which was associated with poorer neuropsychological performance (Preul et al., 2005). Wittstock and colleagues (Wittstock et al., 2010) have recently reported significant colossal atrophy in patients with SVD, compared to controls, and suggest that this difference may be due to demyelination in colossal fibers. Further analysis, e.g. with DWI data, could help substantiate this hypothesis.

## **2. Cortical Morphometry**

The following study investigates the morphometry – particularly cortical thickness and white matter lesion volume – and was published in (Reid et al., 2010).

### **2.1. Methods**

#### ***2.1.1. The RUN-DMC Dataset***

All MRI data collected for the morphometry reported in this dissertation was obtained by the group of Frank-Erik de Leeuw, as part of the Radboud University Nijmegen Diffusion tensor and Magnetic resonance imaging Cohort (RUN-DMC). The data collected from this cohort include:

- T1-weighted and FLAIR MRI
- Diffusion-weighted MRI (DWI)
- Resting-state fMRI
- Cognitive scores
  - Center for Epidemiologic Studies Depression Scale (CESD)
  - Mini-mental state exam (MMSE)
- Questionnaires
  - Life activity
  - Educational level
- Clinical
  - Neurological work-up
  - Gait

#### ***2.1.2. Rationale and Ethics***

Aging has substantial and universal effects upon the structure and function of the human brain, partly as a result of an apparent genetic program and partly as an accumulation of various neuropathies. Approximately 95% of individuals between the age of 60 and 90, for instance, have been reported to have some degree of white matter lesions (WML) (de Leeuw et al., 2001). Small vessel disease (SVD), or microangiopathy, is a common pathological condition in elderly individuals in which small cerebral blood vessels degenerate, resulting in microinfarctions to proximal neural tissue. It is a significant risk factor for age-related cognitive impairment and dementia (O'Brien, 2003), and is also associated with behavioural, psychological, and somatic neurological symptoms (see Section 1.7.5). Despite this, there is little in the way of epidemiological knowledge of the morphological correlates of SVD. The RUN-DMC project is intended to obtain a large body of empirical evidence from a cohort with SVD, to investigate the effects of this condition upon various aspects of morphology, as well as behavioural and neurological function.

### 2.1.3. Subjects

Data were collected from 503 individuals, who volunteered to participate with a response rate of 71.3%. This cohort consists of 284 males and 219 females aged 50-85 years, sampled consistently over this age range. None of the participants suffered from dementia on the basis of international diagnostic criteria, but all have a history of symptomatic SVD (van Norden et al., 2008). Eighteen subjects (3.5%) were excluded from the present analysis due to failures in the cortical surface generation process. Table 2.1 shows the demographics for the subset of the RUN DMC cohort included in the morphometric analysis.

*Table 2.1. Demographics for the RUN-DMC cohort.*

Age decade	Male (n=270)			Female (n=215)		
	50-60 (n=89)	60-70 (n=81)	70-85 (n=100)	50-60 (n=69)	60-70 (n=77)	70-85 (n=69)
Age at disease onset	54.6 (3.0)	63.3 (3.1)	73.9 (3.7)	53.7 (2.9)	63.9 (3.2)	74.1 (3.8)
Disease duration	1.2 (1.1)	1.3 (1.1)	1.2 (0.9)	1.7 (1.3)	1.4 (1.2)	1.7 (1.2)
Age at study participation	55.8 (2.8)	64.7 (2.8)	75.0 (3.5)	55.4 (2.8)	65.3 (2.9)	75.8 (3.7)
MMSE	28.6 (1.4)	28.3 (1.4)	27.5 (1.9)	28.8 (1.3)	28.2 (1.5)	27.4 (1.7)
Education level	5.3 (1.2)	5.1 (1.3)	4.7 (1.7)	5.0 (1.0)	4.5 (1.2)	4.1 (1.5)
WMLV (ml)	6.6 (7.0)	13.6 (18.0)	25.9 (25.1)	8.3 (13.1)	14.7 (21.6)	20.7 (15.2)

*Numbers represent means (SD). All durations are in years. MMSE: Mini Mental State Examination; Educational levels range from 1-7: 1 representing less than primary school and 7 reflecting an academic degree (Hochstenbach et al., 1998).*

### 2.1.4. Imaging Protocols

Imaging was performed by the group of Frank-Erik de Leeuw, on a single 1.5 Tesla scanner (Magnetom Avanto, Siemens Medical Solutions, Erlangen, Germany) at the Donders Center for Cognitive Neuroimaging. The protocol included T1 3D MPRAGE acquisitions (TR/TE/TI 2250/3.68/850 ms; flip angle 15°; voxel size 1.0x1.0x1.0 mm), and Fluid-Attenuated Inversion Recovery (FLAIR) acquisitions (TR/TE/TI 9000/84/2200 ms; voxel size 1.0x1.2x6.0mm (including an interslice gap of 1 mm), and DWI (TR/TE 10100/93ms, voxelsize 2.5x2.5x2.5mm, 4 unweighted scans, 30 diffusion weighted scans with b-value of 900 s/mm<sup>2</sup>). All participants were scanned on the same scanner.

### ***2.1.5. Spatial Normalization***

*Rigid-body* spatial normalization aligns a subject image to a template image, using only translation and rotation parameters. Since the normalized image is not skewed or scaled in this process, this method ensures that the real spatial relationships are preserved. In other words, the image remains in “native space”, which is essential for a morphometric analysis. Spatial normalization was performed by SPM software (SPM5, Wellcome Department of Cognitive Neurology, University College London, UK), which essentially attempts to minimize the difference in intensity distributions between the source and the template image. To facilitate cortical surface approximation, a second linear normalization was performed by the Civet pipeline, using a multi-scale, 9-parameter affine transformation (Collins et al., 1994). This second transformation included x-, y- and z-scaling parameters, which effectively skews all native spatial correspondence; however, such correspondence can be regained (i.e., for morphometric analysis) by applying the inverse transform.

### ***2.1.6. Nonuniformity Correction***

Correction of the MR image for magnetic field nonuniformities (such as result from eddy currents, bias fields, and movement artifacts) is necessary to ensure accurate morphometric results (Vovk et al., 2007). The Civet pipeline performs such a correction using the N3 method (*nonparametric nonuniformity intensity normalization*, (Sled et al., 1998)). In brief, the objective of this method is to obtain analytical approximations of the systematic bias field, as well as estimate the distribution of true tissue intensity, and use these estimates to apply global adjustments to the image.

### ***2.1.6. White Matter Lesion Delineation***

WM lesions were manually segmented on transversal FLAIR images. WML were defined as hyperintense regions on the FLAIR image, with no corresponding CSF-like hypointensity on the T1-weighted image. Due to the manual segmentation, WML could easily be differentiated from Virchow-Robin Spaces as the latter structures are hypointense on both T1 and FLAIR imaging (Kwee and Kwee, 2007). Additionally, gliosis surrounding lacunar and territorial infarctions was not considered to be WML. Segmentation was performed by two trained raters, who were blind to all clinical information. WML volume (WMLV) was calculated as lesion surface area by slice thickness (6 mm), and is reported in ml. Inter-rater variability was determined in a random sample of ten percent and resulted in an intraclass correlation coefficient of 0.99 for total WMLV. Mutual information rigid body coregistration (SPM5, Wellcome Department of Cognitive Neurology, University College London, UK) was used to align WML images with T1 images. A Talairach-based lobar atlas (WFU Pickatlas, v2.3) (Maldjian et al., 2003) was registered to T1 images in SPM, using a non-linear transformation.

### ***2.1.7. Cortical Grey Matter Thickness Estimation***

Cortical thickness (referred to as *Thickness* hereafter, to distinguish it as a variable) analysis was performed using the Civet pipeline (Figure 2.1), which uses a procedure called Constrained Laplacian Automated Segmentation with Proximities (CLASP) (MacDonald et al., 2000; Kim et al., 2005), and cortical thickness was measured as the distance, in native space, along the links between corresponding vertices created in this process (t-link). The resulting surface meshes contained 40,962 vertices per hemisphere. Finally, individual

surface meshes were resampled to a template surface, obtained using an iterative group template registration algorithm (Lyttelton et al., 2007), in order to facilitate intersubject comparisons. The middle-cortex surface obtained from this process was used to calculate two further measures using custom Java routines: 1.) cortical surface area ( $A_{surf}$ ), calculated as the sum of areas of the triangular faces; and 2.) cortical GM volume ( $V_{surf}$ ), calculated as the sum over each face of its area multiplied by its average vertex-wise thickness value.

#### ***2.1.7.1. Tissue classification***

CLASP performs two types of tissue classification : (1.) *discrete classification*, which assigns either GM, WM, or CSF to a voxel (Cocosco et al., 2003); and (2.) *partial volume classification*, which provides an probabilistic estimate of the proportion of a given voxel which contains a given tissue class. This is applied to deep sulci, where partial volume effects (PVE) contribute to uncertainty about the position of the GM/CSF surface. The resulting partial volume classification is used to create a CSF skeleton, which accurately locates the deep sulci.

#### ***2.1.7.2. Surface approximation***

After tissue classification, CLASP begins by deforming a tessellated sphere (one per hemisphere) to approximate the GM/WM, starting with a low resolution (320 vertices), deforming according to a set of minimization constraints, and subsampling on subsequent iterations, to achieve increasingly fine sampling of the anatomical image. The final surfaces contain 40,960 vertices each. The optimization is characterized by the objective function  $O$  (after (MacDonald et al., 2000; Kim et al., 2005)):

$$O(S) = \sum_{k=1}^{N_t} T_k(S)$$

where  $S$  is a surface (or set of surfaces) to be deformed,  $T_k$  is a weighted minimization constraint, and  $N_t$  is the number of such constraints. This formulation allows the importance of each factor to be weighted or thresholded, depending on an *a priori* determination of its importance.

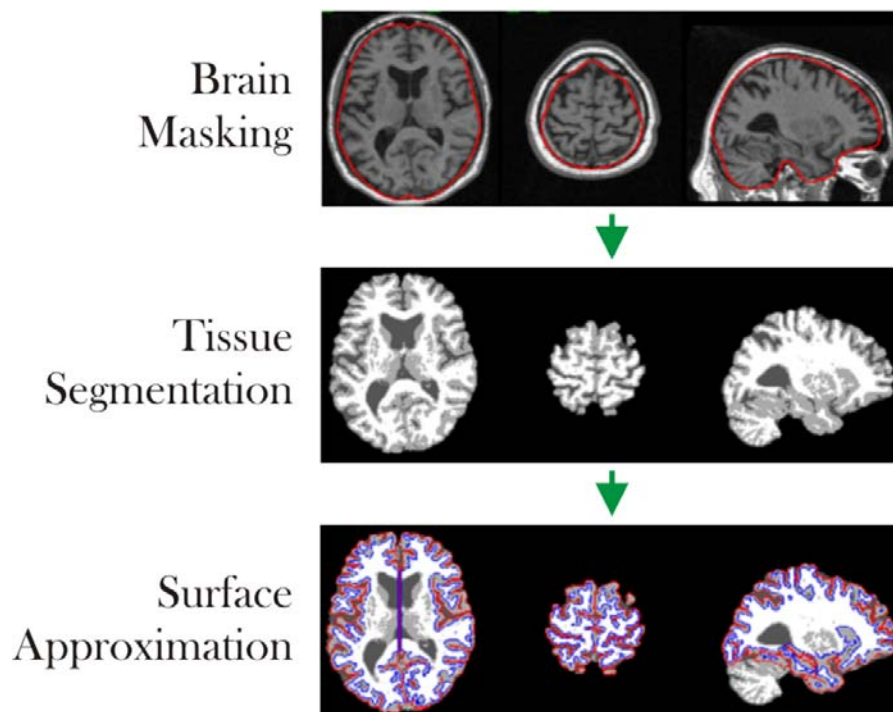


**Figure 2.1.** Surface approximation performed by the Civet pipeline: (1.) non-brain tissue, such as skull and scalp, are masked; (2.) tissue is segmented into GM, WM, and CSF compartments, with partial volume estimates; and (3.) GM and WM boundaries are approximated with a deformable tessellated sphere.

### 2.1.7.3. Deformation constraints

The four constraints used by CLASP to determine the GM/WM surfaces are:

- i. **Boundary term ( $T_{boundary-dist}$ )**  
This is the distance between a vertex  $i$  on  $S$ , and the boundary of the GM and WM image segments, along the normal vector  $N_i$  of  $i$ .
- ii. **Stretch term ( $T_{stretch}$ )**  
This constraint attempts to maintain an ideal distance, defined by an *a priori* model, between a vertex  $i$  and its neighbours, growing as the distance deviates from this ideal.
- iii. **Bending term ( $T_{bend}$ )**  
The bending term penalizes angles between adjacent mesh faces which deviate from an ideal angle, also defined by an *a priori* model. Along with  $T_{stretch}$ , this has the effect of regularizing the surface.
- iv. **Self-proximity ( $T_{self-proximity}$ )**  
This term prevents non-adjacent mesh faces from being pushed too closely together, and has the effect of preventing self-crossing of the surface.

Once the GM/WM surface is approximated, it is used as a starting point for the second surface approximation, that of GM/CSF. For this second optimization,  $T_{stretch}$  and  $T_{self-proximity}$  are used, along with two additional constraints:

i. **Laplacian ( $T_{Laplacian}$ )**

This term is based upon the Laplacian map of the image (generated between the WM segment and CSF skeleton), and guides the smooth expansion of the GM/WM surface towards the CSF surface. This approach also prevents overlapping vertex trajectories, and provides a better correspondence between linked vertices, which is important for thickness estimation (see below).

ii. **Intensity ( $T_{intensity}$ )**

This is a stopping constraint which prevents vertices from moving past the CSF skeleton.

#### 2.1.7.4. Cortical thickness estimate

Having obtained surfaces which approximate the GM/CSF and WM/GM interfaces, a measure of cortical thickness would appear to be straightforward. There are, however, a number of alternatives, which produce slightly different results, particularly in regions of high curvature. Three possible cortical thickness metrics were examined by MacDonald et al. (2000); where  $A$  represents the GM/WM surface, and  $B$  the GM/CSF surface, these metrics are: (1.)  $t-normal$ , which measures the distance to the closest point along the surface normal vector from vertex  $i$  on  $A$ , to  $B$ ; (2.)  $t-closest$ , which measures the closest point (along any vector) from vertex  $i$  on  $A$ , to  $B$ ; and (3.)  $t-link$ , which is the distance between the corresponding nodes on  $A$  and  $B$ , given that  $B$  is a deformed version of  $A$ . The  $t-normal$  measure produces distinct artifacts at sharp turns (see Figure 2.2), and the  $t-closest$  also produces artifacts, which are more evident in 3D. The  $t-link$  measure, which is based upon the Laplacian constraint, is used to obtain the results reported here.

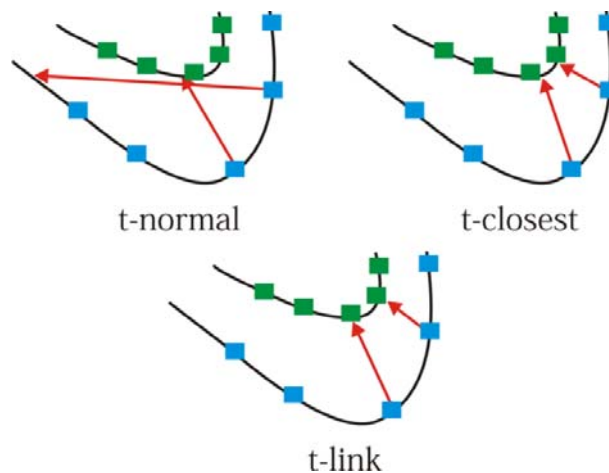


**Figure 2.2.** Three possible measures of cortical thickness.

#### 2.1.8. Cortical Parcellation

Since the cortical surfaces produced by the Civet process are comprised of 81,380 vertices, which, in combination with random field statistical techniques, allows a nice spatial

representation of effects, it is also interesting to view the effects within known anatomical boundaries such as those described by Brodmann. There are a number of reasons to use such a parcellation: (1.) these maps are widely known; (2.) their regions have been traditionally been associated with certain functions, which allows the effects to be interpreted in relation to existing theory; (3.) it permits scatterplot representations of entire cortical regions, rather than representative vertices; and (4.) it allows comparisons to be made directly between regions. However, a major caveat with using this map is the observed lack of correspondence of some Brodmann areas (BAs) with the sulcal landmarks used to deform them across individuals. This is discussed in the next section.

### ***2.1.8.1. Landmark-based deformation***

For the purposes of the present study, I utilize a pre-established version of the Brodmann parcellation delineated first manually on the Colin atlas (Holmes et al., 1998) (personal correspondence with Van Essen), and then deformed to the PALS surface (Section 1.3.4) (Van Essen, 2005). To project this parcellation onto the Civet standard surface requires a landmark-based deformation, which specifies the correspondence between vertices on the PALS surface and those on the Civet surface. It requires the manual delineation of major sulcal and gyral landmark polylines on both surfaces, and the computation of a deformation field which assigns identical spatial coordinates to points along the polylines, and interpolates along the surface mesh between these landmarks, preserving surface topology and neighbourhood relationships (Van Essen et al., 1998). The deformation from PALS to Civet was performed by David Van Essen using Caret software, and is available on the SumsDB online database (Van Essen et al., 2005) (personal correspondence with Van Essen).

As mentioned, there is a major caveat with using this approach to assign the Brodmann parcellation to individual cortical representations. Amunts and colleagues (Amunts et al., 1999), for instance, investigated the cytoarchitectonic boundaries of BA44 and BA45 for many individuals, and found a substantial interindividual variation in both regional volume and correspondence with sulcal contours, thus challenging the assumptions of sulcal landmark-based approaches. This issue was considered in (Van Essen, 2005), by comparing the regional delineations of BA17, BA44, and BA45 on the PALS surface, with the probabilistic distribution described in (Amunts et al., 1999). While correspondence, illustrated in Figure 12 of (Van Essen, 2005), is not perfect, it does appear to capture the majority of the regional variance in the probabilistic atlas. To further address this important issue, we obtained modified mean *Thickness* values by weighing the contribution of individual vertex-wise *Thickness* values according to their proximity to a regional boundary (assuming that more central vertices have less uncertainty than border vertices). This approach is similar to one reported by Bezgin and colleagues (Bezgin et al., 2008), and was done using two weighting functions (Figure 2.3): (1.) a Gaussian decay weighting all middle nodes with 1.0 and using a sigma of 0.5; and (2.) a linear decay with all border nodes weighted 0.0 and middle nodes 1.0.

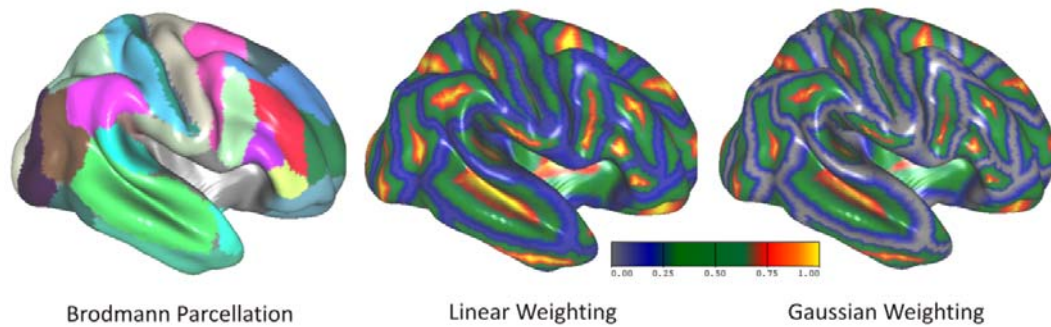


**Figure 2.3.** Weighting functions applied to Brodmann area ROIs, shown on the mean surface for the RUN-DMC cohort. Weighting was applied with both linear and Gaussian functions.

### 2.1.8.2. Intersubject surface coregistration

Once individual surface approximations and the corresponding morphometry have been performed in native space, it is desirable to align them to one another, or to some template surface, in order to allow population statistics to be calculated. This is no simple problem, since the morphology of individual brains can be highly variable. One possible solution is, again, the use of gyral and sulcal patterns as an alignment constraint. Such an approach is performed by the Civet pipeline, aligning individual surfaces to a template constructed using an iterative resampling approach (Lyttelton et al., 2007). Given that each Civet surface has the topology of a sphere, and an equal number of *coarsely* corresponding vertices, the object here is to (1.) assign a *feature field* to the surface, for a feature which we want to align (e.g., mean curvature at each vertex); and (2.) manipulate the individual sphere by moving it around, until its feature field fits as closely as possible with the template sphere. This is equivalent to remapping the vertex indices, thus altering the correspondence with the template sphere. If these steps are repeated iteratively, in a multi-scale way (such that increasingly fine resolutions are used), and for a large number of individuals, the result is a population-based template of curvature, which can be used to coregister other individuals.

### 2.1.9. Statistical Analyses

Statistical analyses of cortical thickness (*Thickness*) were performed in four ways: (1.) mean, describing effects over all vertices; (2.) vertex-wise, describing effects at each vertex; (3.) ROI-wise, describing mean effects within the subsets of vertices defined by the Brodmann parcellation; and (4.) grouped by age, to allow a comparison of effects across three age groups: 50-60, 60-70, 70+. Analyses were performed using the SurfStat Matlab library (Worsley et al., 2009) and SPSS (Release 16, SPSS Inc., Chicago).

One important issue arising from the image-based analyses summarized below is that of family-wise error (FWE); given that a typical image-based analysis will involve thousands of statistical comparisons, a large amount of Type I error (i.e., false positives) is expected. At least two correction methods are possible for such a large number of comparisons: (1.) the *false discovery rate* (FDR), which yields the expected rate of false positives per voxel; and (2.) *random field theory* (RFT), which uses the Euclidian characteristic to integrate spatial information into an estimate of Type I error. These are elaborated below:

#### 2.1.9.1. False discovery rate

The simplest correction for FWE is the Bonferroni method, which refers to simply reducing the threshold  $\alpha_0$  for rejecting the null hypothesis by a factor proportional to the number of comparisons  $m$ :

$$\alpha_{BC} = \frac{\alpha_0}{m}$$

The Bonferroni correction is extremely conservative, and is impractical for any large  $m$ , such as is inherent in voxel- or vertex-wise statistical parametric maps (SPMs, see below). FDR is a less conservative measure, and can be loosely defined as the expected rate of false positives  $V$  amongst all significant comparisons  $R$  (at threshold  $\alpha_0$ ) (Storey, 2003):

$$FDR = E \left[ \frac{V}{R} \right]$$

The difference between FDR and FWE corrections is that the former estimates an error rate from a fixed rejection area ( $R$ ), whereas the latter estimates a rejection area from a fixed error rate ( $\alpha_0$ ). FDR is perhaps most useful as an exploratory technique; when performing a large number of, for instance, drug discovery trials, it is capable of estimating which comparisons are most likely significant (Benjamini and Yekutieli, 2001). Genovese and colleagues (Genovese et al., 2002) introduced FDR as a way to correct for multiple comparisons in neuroimaging; i.e., by voxel-wise corrections to SPMs.

#### 2.1.9.2. Random field theory

RFT (Worsley et al., 1992) is based upon the observation that a neuroimage obtained from MRI is actually a *continuous field*: the intensities of neighbouring voxels are not independent of one another, but form part of a continuous function describing a physical medium (the human head). As such, effects in an SPM should actually be treated as distinct topological *features*, comprised of clusters of voxels, and the correction for multiple comparisons should be done feature-wise, rather than voxel-wise. These features can be approximated by a thresholded Euler characteristic (which estimates the number of distinct peaks in an SPM, and thus its effective dimensionality), and FWE corrections can be performed on these feature clusters (also called *resolution elements*, or *resels*) (Worsley et

al., 2004). Chumbley and Friston (Chumbley and Friston, 2009) argue against the commonly-used approach of performing voxel-wise FDR corrections on SPMs, illustrating that if FDR is to be used, it ought to be applied in a feature-wise manner.

### **2.1.9.3. Mean Analyses**

Mean (subject-wise) analyses were performed for GLMs of the form:

$$Thickness \sim Age + Sex + Age \times Sex$$

$$A_{surf} \sim Age + Sex + Age \times Sex$$

$$V_{surf} \sim Age + Sex + Age \times Sex$$

$$A_{surf} \sim Hemisphere$$

$$V_{surf} \sim Hemisphere$$

### **2.1.9.4. Vertex-wise Analyses**

Vertex-wise statistics were computed as individual linear models for each of 40,962 vertices per hemisphere. To indicate effect size, they are represented here as significant slope values, such that all non-significant slopes ( $p < 0.05$ ) are set to zero. Corrected  $p$  statistics are obtained for these vertices using random field theory.

The following GLMs were analyzed, using SurfStat:

$$Thickness \sim Age + Sex + Age \times Sex$$

$$Thickness \sim Age + WMLV + Age \times WMLV$$

### **2.1.9.5. ROI-wise Analyses**

ROI-based analysis of *Age*, *Sex*, and *Hemisphere* effects were performed by computing individual linear models for the mean of the subset of vertices in a given GM ROI. Significance thresholds were corrected for FWE using the Holm-Bonferroni method.

The following GLMs were analyzed, using SurfStat:

$$Thickness \sim Age + Sex + Age \times Sex$$

$$Thickness \sim Age + WMLV + Age \times WMLV$$

$$Thickness \sim Age + Hemisphere$$

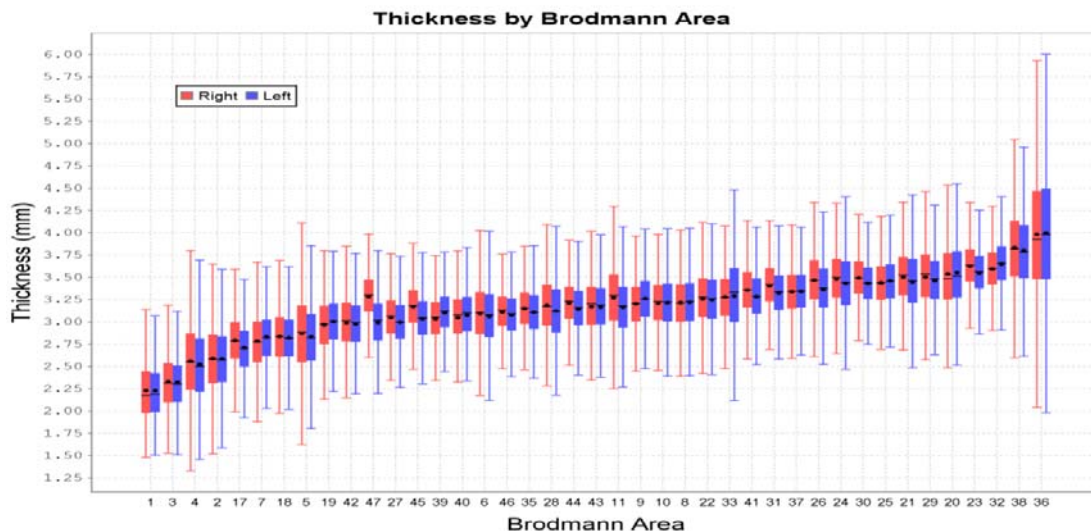
### **2.1.9.6. Grouped by Age**

Given our findings that GM ROI-wise *WMLV* was not significantly related to *Thickness* after *Age* was included as a factor, we decided to further investigate the ROI-wise correlation between *WMLV* and *Thickness* in three separate age groups: 50-60, 60-70, and 70+. Because *WMLV* is bound by zero, and consequently has a large positive skew, we applied a log transformation to these data, resulting in a bivariate normal distribution, which is necessary for a linear regression analysis. To plot the results for each group, we standardized the slope values to the statistics of the entire population. Significance was assessed using both  $p$ - and  $q$ -values (false discovery rate, FDR).

## 2.2. Results

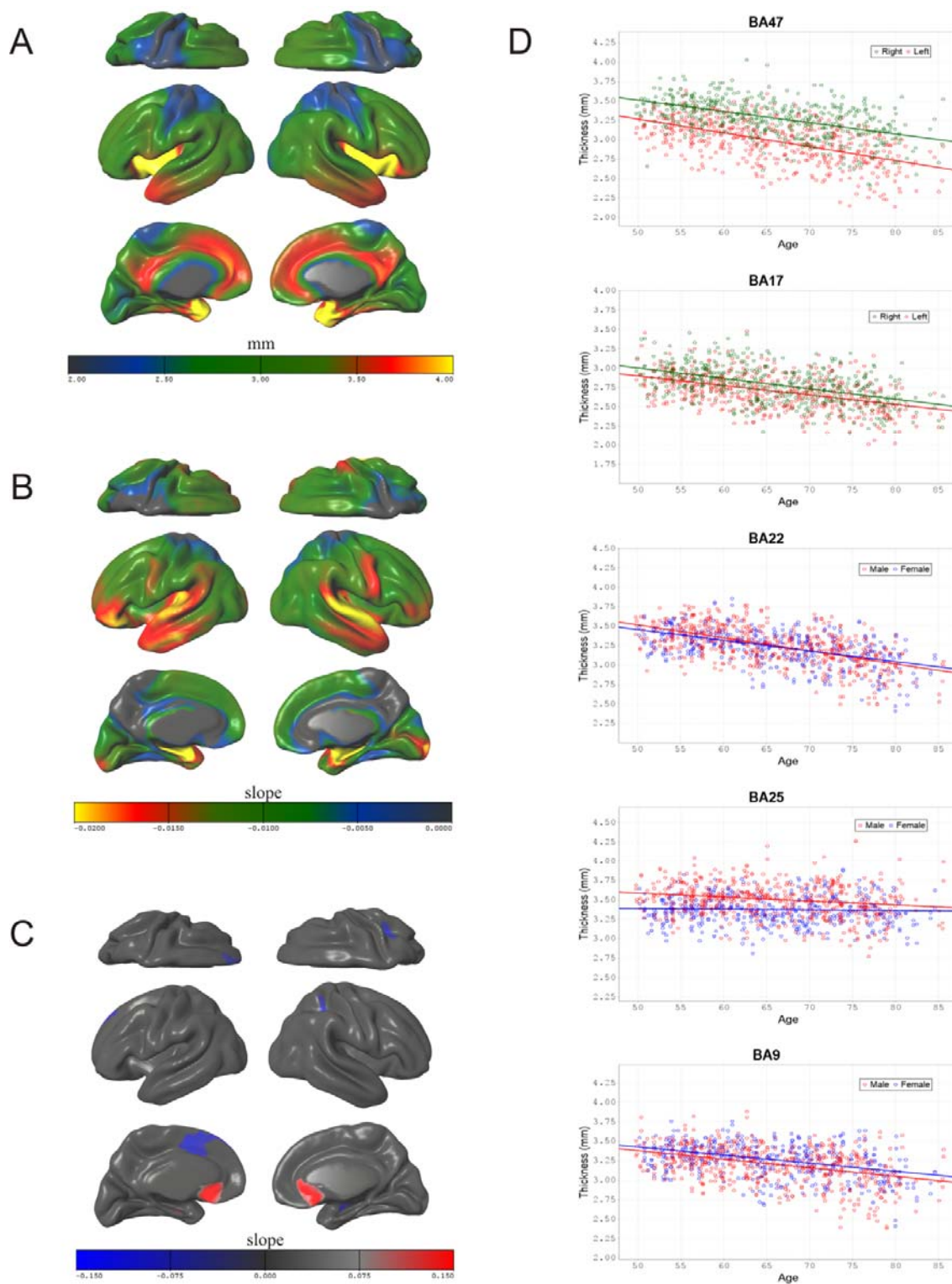
### 2.2.1. Descriptive Statistics

Figure 2.4 shows the distribution of mean *Thickness* for each Brodmann Area (BA), as box plots for each hemisphere. BA1 and BA3 were thinnest ( $\sim 2$  mm) while BA38 and BA36 were thickest ( $\sim 3.75$  mm) with a high variance. Vertex-wise mean *Thickness* is likewise distributed nonuniformly across the cortical sheet (Figure 2.4A), being thinnest in primary somatosensory and motor cortices ( $\sim 2$  mm) and thickest in the medial temporal lobe, temporal lobe, and insula ( $\sim 4$  mm or higher). The distribution of variance was also nonuniform, being highest ( $\sim 0.2$  mm) in the perirhinal region and moderately high ( $\sim 0.15$  mm) in the primary motor and somatosensory cortices as well as the temporal pole. Analysis of hemispheric differences showed a significant difference in mean *Thickness* (right > left) ( $t = -9.40$ ,  $p < 0.01$ ), and significant hemispheric asymmetry in 28 Brodmann areas (Table 2.2). The largest differences were found in the lateral prefrontal areas BA47 (Figure 2.5D), BA11, and BA45, in which the right hemisphere was thicker than the left.



**Figure 2.4.** Box plots showing the distribution of *Thickness* for each BA ROI, for each hemisphere. ROIs are sorted by increasing mean *Thickness*. Filled boxes represent quartiles 1 to 3, capped lines indicate the range of regular values, circles indicate the mean, and horizontal lines indicate the median.

## Cortical Morphometry



**Figure 2.5.** Three-dimensional renderings of vertex-wise values mapped onto the average surface and scatterplots of individual Brodmann area ROIs. **A.** Spatial distribution of vertex-wise mean Thickness in mm. **B.** Spatial distribution of the slope for Age in each vertex-wise linear model of the form  $\text{Thickness} \sim \text{Age} + \text{Sex} + \text{Age} \times \text{Sex}$ . **C.** Spatial distribution of the slope for Sex (Male - Female) in the model  $\text{Thickness} \sim \text{Age} + \text{Sex}$ ; a positive (red) value corresponds to Male > Female. **D.** Scatterplots of Age vs. mean Thickness for five Brodmann areas.

**Table 2.2.** Results of ROI-wise statistical analyses.

ROI	Asymmetry <sup>†</sup> (mm)	T-values											
		Asymmetry	Age x Hemisphere <sup>††</sup>		Sex <sup>‡</sup>		Age x Sex <sup>‡‡</sup>		WML		Age x WML		
			Age	Left	Right	Left	Right	Left	Right	Left	Right	Left	Right
BA1	0.00	0.08	0.54	-4.63 **	-4.63 **	-0.32	-0.95	0.18	0.76	1.26	1.69	-1.00	-1.48
BA2	0.00	-0.81	0.73	-4.68 **	-5.17 **	0.36	0.34	-0.54	-0.59	1.54	1.48	-1.49	-1.43
BA3	0.01	-1.24	0.52	-5.19 **	-4.69 **	-0.18	-0.39	0.06	0.26	1.52	2.47	-1.26	-2.28
BA4	0.03 (R>L)	-6.05 **	0.80	-4.86 **	-4.26 **	-0.51	-0.88	0.37	0.79	1.97	2.85	-1.59	-2.60
BA5	0.04 (R>L)	-5.67 **	-0.55	-2.39 **	-2.34 **	-1.79	-1.31	1.66	1.22	2.28	1.74	-1.89	-1.40
BA6	0.03 (R>L)	-6.19 **	-1.67	-6.38 **	-5.33 **	0.03	-0.52	-0.24	0.36	1.71	2.05	-1.66	-2.07
BA7	0.05 (L>R)	8.48 **	-0.05	-3.41 **	-3.75 **	-0.67	-0.77	0.60	0.60	2.20	1.94	-2.08	-1.85
BA8	0.00	0.75	-1.26	-5.92 **	-5.04 **	-0.67	-0.97	0.33	0.83	1.63	2.18	-1.54	-2.21
BA9	0.06 (L>R)	10.82 **	-1.64	-5.78 **	-4.88 **	-0.54	-0.53	0.17	0.17	1.66	1.45	-1.89	-1.79
BA10	0.00	0.32	-1.16	-6.06 **	-5.91 **	0.75	-0.22	-0.78	0.11	1.54	1.22	-2.09	-1.79
BA11	0.11 (R>L)	-22.09 **	-4.07 ** (L>R)	-6.11 **	-4.34 **	1.78	0.92	-1.50	-0.78	0.91	1.47	-1.41	-1.96
BA17	0.09 (R>L)	-14.18 **	1.54	-8.22 **	-8.42 **	0.04	0.49	-0.03	-0.46	0.22	0.08	-0.26	-0.32
BA18	0.01	-2.03	-0.40	-7.47 **	-6.74 **	-0.13	0.37	0.25	-0.29	1.21	1.46	-1.12	-1.47
BA19	0.04 (L>R)	8.09 **	0.76	-5.63 **	-5.96 **	-0.18	0.63	0.39	-0.39	1.77	2.00	-1.82	-2.12
BA20	0.01	2.22	-1.59	-7.11 **	-6.37 **	2.00	1.43	-1.93	-1.33	0.32	0.70	-0.54	-0.86
BA21	0.05 (R>L)	-7.05 **	-3.42 * (L>R)	-8.15 **	-6.49 **	1.80	1.33	-1.60	-1.23	0.77	1.90	-0.93	-2.12
BA22	0.01	-1.38	-1.42	-9.81 **	-8.62 **	1.55	0.99	-1.44	-0.87	0.27	0.92	-0.74	-1.27
BA23	0.08 (R>L)	-10.08 **	0.10	-0.96 **	-0.16 **	2.37	2.22	-2.09	-1.90	-0.37	0.49	-0.29	-1.21
BA24	0.05 (R>L)	-6.97 **	-2.70	-2.47 **	-1.36 **	1.43	1.81	-1.45	-1.63	0.95	0.28	-1.28	-0.58
BA25	0.02 (L>R)	3.18 *	-2.51	-1.91 **	0.48	2.10	2.94	-1.10	-2.01	0.19	0.80	-0.44	-1.26
BA26	0.11 (R>L)	-8.20 **	0.49	-0.64 *	-0.30 **	2.18	2.80	-1.93	-2.43	0.63	1.73	-0.98	-2.23
BA27	0.06 (R>L)	-6.52 **	-0.12	-2.64 **	-2.48 **	2.18	1.80	-1.90	-1.44	0.76	1.64	-1.03	-1.91
BA28	0.06 (R>L)	-5.59 **	0.92	-10.80 **	-9.49 **	2.05	1.13	-1.96	-1.09	-2.07	-0.24	1.92	-0.10
BA29	0.04 (R>L)	-4.10 **	2.42	0.14	-0.86 **	1.27	2.40	-0.93	-2.08	0.86	1.74	-1.27	-2.24
BA30	0.06 (R>L)	-7.86 **	4.18 ** (R>L)	-0.36 *	-1.92 **	0.35	2.29	-0.03	-2.00	1.45	1.99	-1.77	-2.54
BA31	0.08 (R>L)	-14.59 **	-0.71	-1.76 **	-1.28 **	-0.07	1.10	0.13	-1.01	0.99	0.81	-1.12	-1.04
BA32	0.06 (L>R)	9.09 **	-1.10	-3.33 **	-3.47 **	1.76	1.23	-1.89	-1.40	1.56	0.94	-2.10	-1.43
BA33	0.01	0.76	-2.06	-0.52	0.62	0.34	1.52	-0.06	-0.95	0.48	0.11	-0.68	-0.20
BA35	0.04 (R>L)	-6.14 **	0.63	-2.67 **	-3.08 **	2.42	1.59	-2.16	-1.43	1.20	1.52	-1.56	-1.86
BA36	0.02	1.46	-1.69	-9.84 **	-7.88 **	2.23	2.29	-1.96	-2.26	-0.35	0.35	0.15	-0.56
BA37	0.00	0.52	-1.22	-4.55 **	-5.03 **	0.63	1.07	-0.48	-0.81	1.02	0.29	-1.33	-0.48
BA38	0.03 (R>L)	-3.83 **	-1.90	-8.42 **	-7.20 **	1.82	1.55	-1.60	-1.42	0.24	0.52	-0.49	-0.72
BA39	0.07 (L>R)	10.79 **	-1.43	-6.13 **	-5.66 **	0.39	0.94	-0.46	-0.86	0.51	1.14	-0.94	-1.40
BA40	0.02 (L>R)	3.47 **	-1.21	-6.30 **	-6.30 **	1.21	0.81	-1.41	-0.86	0.56	0.76	-1.11	-1.19
BA41	0.07 (R>L)	-10.28 **	-1.49	-6.59 **	-5.62 **	2.52	1.93	-2.56	-1.72	-0.02	1.21	-0.79	-1.61
BA42	0.02	-2.19	0.32	-9.94 **	-10.16 **	2.08	1.97	-1.98	-1.88	-0.37	-0.70	-0.37	0.20
BA43	0.00	-0.64	1.43	-6.02 **	-6.44 **	1.63	1.04	-1.43	-0.88	-0.34	0.02	-0.06	-0.39
BA44	0.07 (R>L)	-9.41 **	-1.54	-5.97 **	-4.18 **	-0.20	-0.12	0.25	0.17	0.82	1.14	-1.19	-1.66
BA45	0.14 (R>L)	-16.74 **	-3.17	-7.02 **	-4.96 **	-0.27	0.20	0.39	-0.03	1.24	0.37	-1.73	-0.96
BA46	0.03 (R>L)	-5.56 **	-2.67	-7.13 **	-6.16 **	0.06	0.04	-0.10	-0.06	1.21	0.22	-1.56	-0.69
BA47	0.29 (R>L)	-32.81 **	-3.18	-8.84 **	-8.00 **	0.81	-0.36	-0.88	0.59	0.92	0.13	-1.43	-0.68

† Indicates the thicker hemisphere and mean interhemispheric difference in mm

†† Indicates the hemisphere in which the age effect is stronger

‡ For a male-female comparison; a positive t-score indicates male thicker than female

‡‡ For a male-female comparison; a positive t-score indicates that the age effect is stronger for males than females

\* Significant at the  $\alpha=0.05$  level (corrected for multiple comparisons)

\*\* Significant at the  $\alpha=0.01$  level (corrected for multiple comparisons)

### 2.2.2. Age

There was a significant mean negative effect of *Age* on *Thickness*, for both left ( $t = -13.16, p < 0.01, R_{adj}^2 = 0.262$ ) and right ( $t = -12.73, p < 0.01, R_{adj}^2 = 0.244$ ) hemispheres. Figure 2.5B shows the spatial distribution of the vertex-wise GLMs analyzed for *Age*, and corrected with RFT. Most of the cortical sheet showed a significant decrease of *Thickness* with *Age*, with the greatest effects apparent in the ventrolateral prefrontal cortex (BA45, BA46, BA47), the primary and secondary auditory cortices (BA41, BA42), Wernicke's area (BA22), medial temporal lobe (BA36, BA28, excluding the hippocampal formation and amygdala), and the primary visual cortex. Analysis of individual Brodmann ROIs provides an alternative picture of this distribution. In three Brodmann areas (BA11, BA21, and BA30), the effect of *Age* on *Thickness* was asymmetrical, as indicated by a significant

## Cortical Morphometry

*Age × Hemisphere* interaction (Table 2.2). There were no significant mean, vertex-wise, or ROI-wise quadratic effects of *Age* on *Thickness*. The complete set of scatterplots for *Age × Thickness*, separated by hemisphere, can be found in the Appendix.

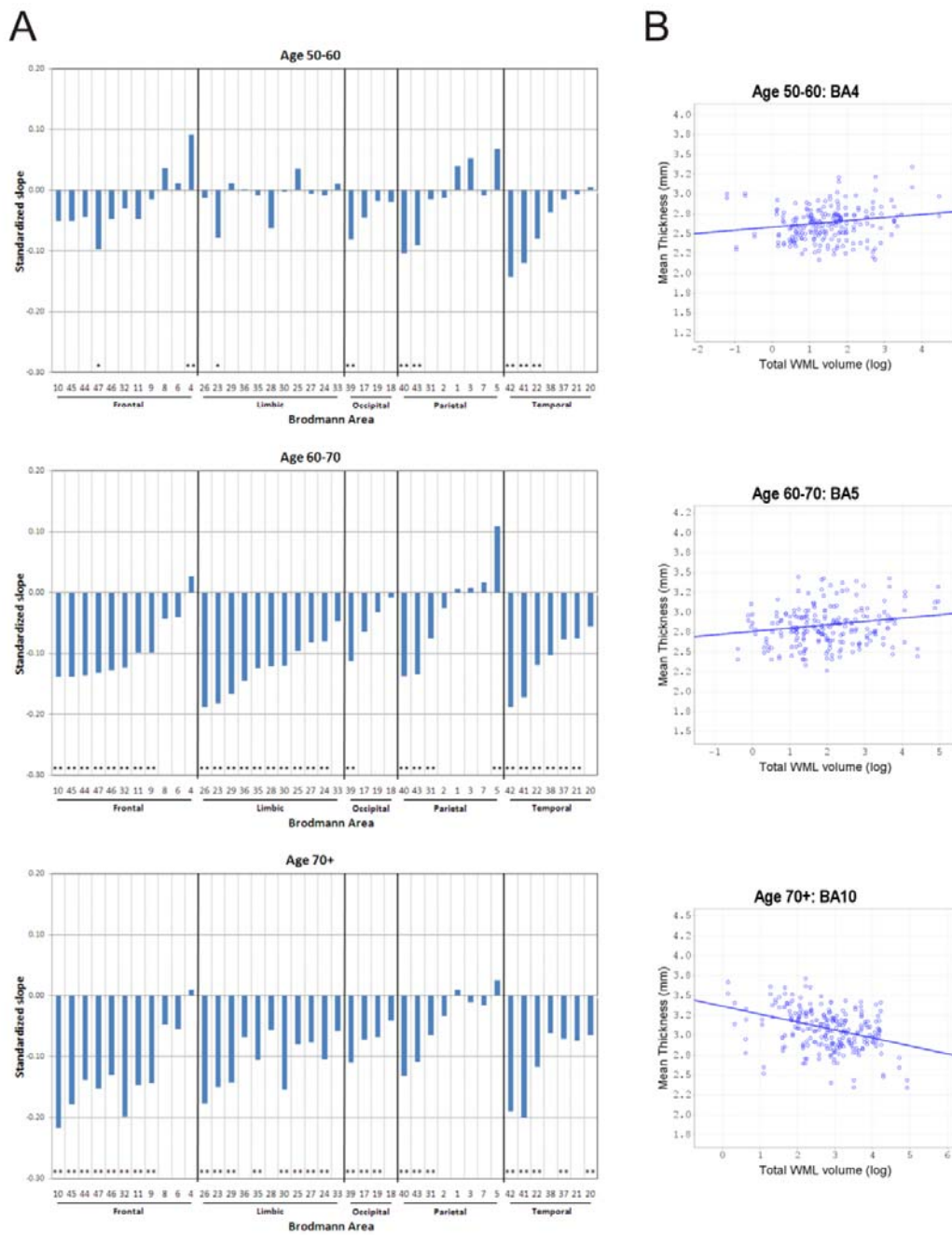


**Figure 2.6.** Correlations between WMLV and Thickness, for each BA, across three age groups. **A.** Standardized slopes for all BAs, sorted by lobe, then slope from the 60-70 age group. (\* = significant at  $\alpha = 0.05$ ; \*\* = significant at  $\alpha = 0.01$ ). **B:** Scatterplots of  $\log(\text{WMLV})$  versus mean Thickness, for selected BAs from each age group.

### 2.2.3. Sex

While no significant mean effect of *Sex* on *Thickness* was found for either hemisphere, vertex-wise GLMs highlight moderate effects, which were only significant after removal of the  $Age \times Sex$  interaction term (Figure 2.5C): there was a significant bilateral effect (Male > Female) in the subgenual area (BA25), and a unilateral effect (Female > Male) in the left anterior cingulate cortex (BA32). Analyses of Brodmann area ROIs did not result in any significant ROI-wise effects of *Sex*, after correction for multiple comparisons. There was also no significant mean interaction effect of  $Age \times Sex$  on *Thickness*, nor any pattern of significant vertex-wise or ROI-wise interaction effects (Table 2.2).

### 2.2.4. White Matter Lesions

No significant ROI-wise effects were found after correction for multiple comparisons, for either *WML* or  $Age \times WMLV$ , in the model  $Thickness \sim Age + WMLV + Age \times WMLV$ . After splitting the cohort into three age groups (50 to 60, 60 to 70, and 70 to 85), we tested the model  $Thickness \sim \log(WMLV)$  for each. The resulting correlations are shown in Figure 2.6A, with selected scatterplots shown in Figure 2.6B. 8 BAs show significant negative correlations in the 50-60 group ( $p < 0.05$ ,  $q < 0.05$ ), 28 BAs in the 60-70 group, and 27 BAs in the 70+ group. BA4 shows a significant positive correlation for the 50-60 age group, as does BA5 for the 60-70 age group.

### 2.2.5. Accuracy of Brodmann Parcellation

Given the question of correspondence between sulcal landmarks and Brodmann areas, we tested the effect of weighing vertex-wise values by their proximity to regional borders, both with Gaussian and linear weighting functions. The results of this weighting on mean *Thickness* are shown in Figure 2.7. Neither the mean or standard deviation of *Thickness* change substantially with either weighting function, indicating that the uncertainty of regional borders does not have a significant impact upon the resulting statistical distribution of their *Thickness* values.

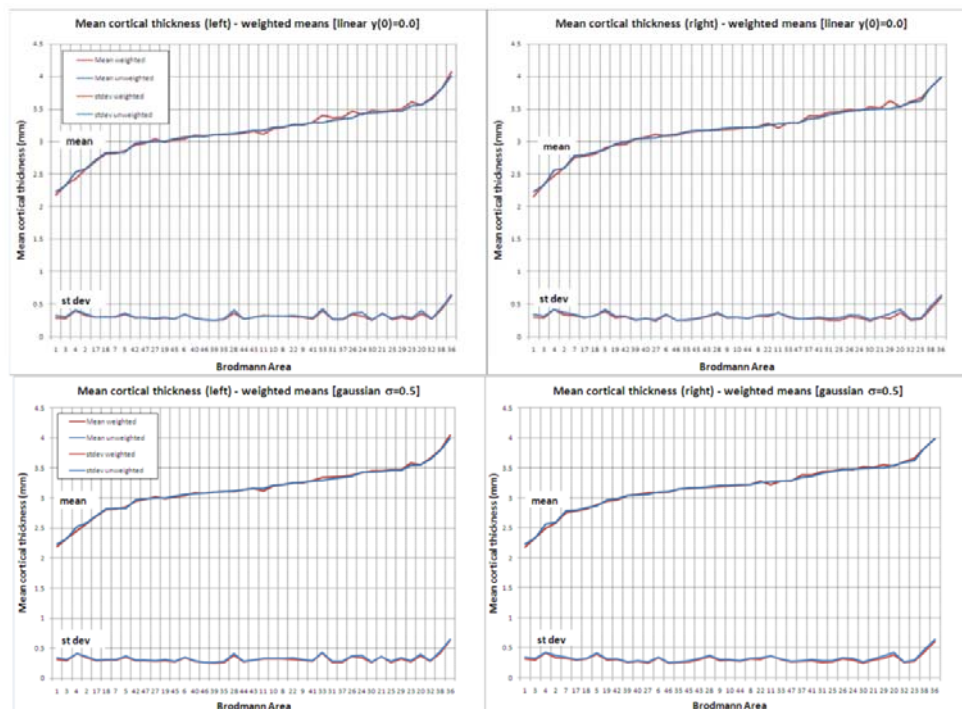


**Figure 2.7.** Weighing vertices by proximity to borders. Means and variances for Thickness by Brodmann ROI are shown, obtained by (1.) no weighting, and (2.) weighting by proximity to regional borders, using either Gaussian or linear weighting functions.

## 2.3. Discussion

The interpretation of the results reported here is greatly enhanced by the fact that they are derived from an exceptionally large cohort with a variety of data modalities: 503 elderly adults, evenly sampled by age, and matched for sex; four types of MRI acquisitions using identical protocols on the same scanner; and a variety of information regarding neurology, cognition, and life history. Moreover, the RUN-DMC cohort is controlled by excluding cases of clinical dementia, and including on the basis of observable small vessel disease, which is a very common condition in elderly adults (although its prevalence is difficult to estimate due to the necessity of an MR scan for diagnosis), and is a risk factor for more severe vascular pathologies. Here I discuss the implications of our results within the context of existing literature and technology.

### 2.3.1. Distribution of Cortical Thickness

Cortical thickness has a clear heterogeneous distribution across the cortex in our population, which is illustrated in Figure 2.4 and Figure 2.5A. Superior primary motor and sensory areas are comparatively thin (2.0 to 2.5 mm), and the temporal pole and medial temporal cortex is comparatively thick (3.5-4.0 mm). BA36 has a particularly high mean thickness as well as a wide variance, with values as high as 6 mm (Figure 2.4). While BA36 is indeed a thicker region, it is conceivable that, given its convoluted structure and the poor contrast of tissue types in this region (see Figure 2.8), some of its variance is attributable to measurement artifact. For the rest of the brain, however, the distribution of thickness values seems reasonable, and similar to that reported in at least one study (Hutton et al., 2009),

albeit globally higher than values reported in another (Salat et al., 2004), a difference which may be attributable to differing methods, which is worthy of further investigation.

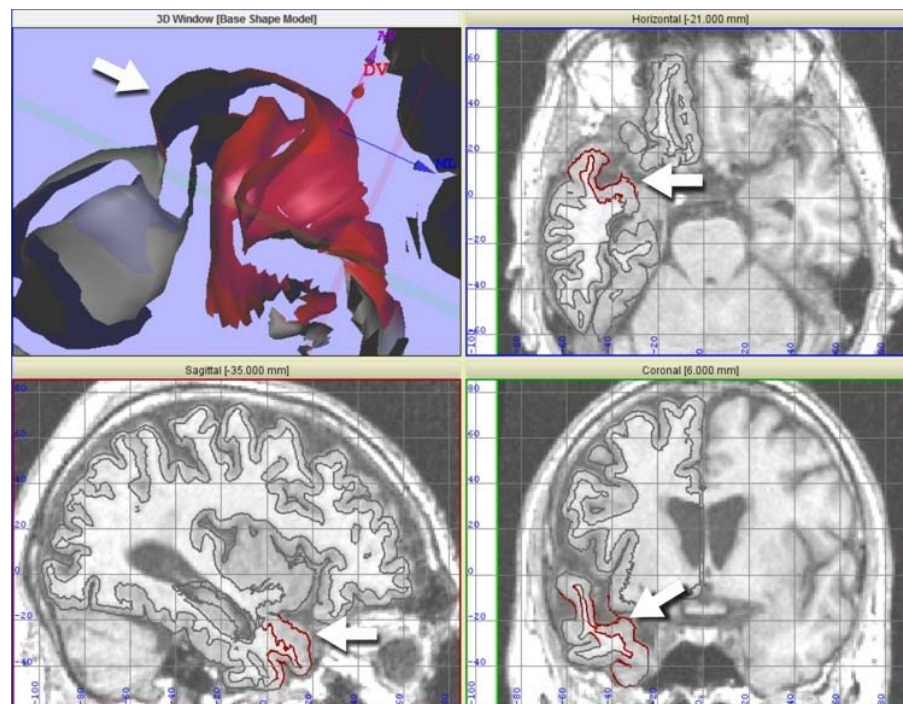


**Figure 2.8.** Delineation of BA36 (in red), shown as a 3D rendering and 2D sections.

The insula has been excluded from the analyses, because the accuracy of delineating this structure, which lies in close proximity with basal ganglia and is difficult to differentiate even by eye, remains questionable. Kim and colleagues (Kim et al., 2005) have made a direct attempt to address this issue with their CLASP algorithm, using partial volume labelling which includes a subcortical compartment in regions close to the insula, identified probabilistically (see their Figures 4 and 5). Unfortunately, based upon our own results, the delineation of insula resulted in exceptionally large thickness (~6 mm) and variance, and in combination with visual inspection of a few subjects (for example, Figure 2.9), this led us to exclude the region from our final results.

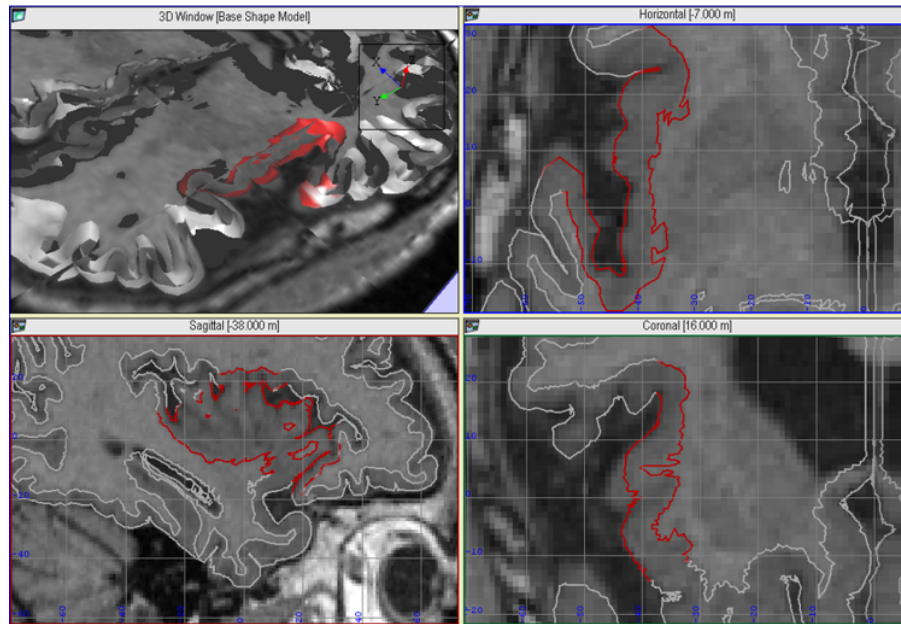


**Figure 2.9.** Delineation of the insula (shown in red). Note the proximity to subcortical GM, which creates an added difficulty for tissue classification.

### 2.3.2. Age-related Cortical Thinning

In our cohort of elderly adults diagnosed with SVD, we find that cortical thickness decreases with age across most of the cortical sheet. The largest age effects were observed in the ventrolateral prefrontal cortex, the primary and secondary auditory cortex, Wernicke’s area, the medial temporal lobe, and the primary visual cortex (Figure 2.5B). Interestingly, the age effect in primary visual cortex is focused in the posterior region, which corresponds to foveal innervations (Wandell, 1999). This distribution of age effects is similar to that of GM density reported in one study (Good et al., 2001), but differs somewhat from another study of cortical thickness, in which the authors report thinning primarily in the primary motor cortex, where we find only a moderate significant effect, and apparent sparing of the ventrolateral prefrontal and temporal cortices, where we find the largest age effects; although these authors do report a similar thinning of visual cortex (Salat et al., 2004). This discrepancy might be due to the considerable differences between cohorts: (1.) the RUN-DMC cohort ranges in age from 50-85, while the Salat et al. cohort ranges from 19 to 93. The observed difference would suggest that the effect of age is nonlinear across the human life span, which is supported by findings from (Sowell et al., 2003). (2.) There was most likely a higher incidence of SVD in our cohort, although SVD was also present to some extent in the latter population (personal correspondence with Salat); given the tight relationship between age and SVD, it is difficult to disentangle these two factors. In at least one report (Preul et al., 2005), a decreased mean cortical thickness was observed in individuals with SVD versus aged-matched controls, but the distribution of this effect across the cortex has not been investigated.

Age-related thinning of primary auditory and visual cortices may represent a morphometric correlate to the hearing and visual deficits commonly reported by elderly adults. Similarly, the moderate thinning of inferior parts of motor cortex may predict a degree of motor deficits

(such as gait problems or head motion), although both of these speculations remain to be definitively investigated. Although the present study does not include the hippocampal formation or amygdala, a separate study has reported that age-related subjective cognitive failures are negatively related to hippocampal volume (van Norden et al., 2008), which may be closely associated with the preferential thinning of medial temporal cortex observed here. Finally, the age-related thinning of prefrontal and lateral temporal cortex has been noted variously in VBM studies (Good et al., 2001; Sowell et al., 2003; Raz et al., 2004), and also corresponds with fMRI evidence linking activity in these regions to cognitive deficits, including impaired memory and executive function, in elderly adults (reviewed in (Grady, 2008); see also Section 1.7).

### ***2.3.3. Sex Differences***

We find a sex difference in cortical thickness in our cohort only for the vertex-wise analysis, and only after removing the interaction term from the model. This suggests a rather moderate local effect, but one which merits a brief discussion. As shown in Figure 2.5B, there is increased cortical thickness for males bilaterally, in BA25, and an increased thickness for females unilaterally in the left anterior cingulate (BA32). The former effect is interesting since it is the target of deep brain stimulation, as a treatment for major depression (MD) which is unresponsive to conventional treatments (Mayberg et al., 2005). Given that MD has a substantially higher lifetime prevalence amongst females than males (Steffens et al., 2000), this morphological finding may also be related to MD. Since depression data (CESD scores) are available for this cohort, we tested this possibility with the vertex-wise GLM  $Thickness \sim Age + CESD$ , but did not find a significant effect of CESD at any part of the cortical sheet (unpublished findings).

### ***2.3.4. Relating White and Grey Matter Morphometry***

Combining the observation that 95% of adults aged 60-90 have some degree of WML (de Leeuw et al., 2001), and the observed patterns of cortical GM thinning reported here, and considering that cortical GM is connected through subcortical WM, the obvious question is: how are the two related? The answer to this question has important implications both for clinical practice, and basic research into the connectivity of the human brain. As a preliminary step, we investigated the relationship of total WMLV with GM thinning, and found no effect after accounting for age. However, since age is tightly coupled to WML incidence (de Leeuw et al., 2002), it is interesting to investigate it further. To do this, the RUN-DMC cohort was separated into three age groups, and the correlations of total WMLV with thickness in each Brodmann area were analyzed.

The results shown in Figure 2.6 suggest that, for the 50-60 group, there appears to be only a weak negative correlation of WMLV with thickness, in a small number of regions. In contrast, negative correlations are substantially increased across most BAs for both of the older age groups, indicating a tighter coupling of the two morphological factors over the age of 60. The strongest of these relationships is found in structures associated with executive function (BA10), speech production (BAs 44 and 45, or Broca's area), emotionality (BAs comprising cingulate cortex), and auditory processing (BAs 41 and 42). We also find positive correlations in the youngest group for BA4 (primary motor cortex), and in the middle group for BA5 (a secondary somatosensory area). These somewhat counterintuitive results may indicate a common compensatory and/or dedifferentiation mechanism in these regions,

similar to a reported hypertrophy of prefrontal cortex, which was associated with decreased cognitive performance (Salat et al., 2002). This is elaboration in the next section. The functional implications of an increased BA4 and BA5 are unclear, although the former may be related to one report of alterations to motor circuitry, including decreased subcortical-cortical connectivity and *increased* connectivity within and between motor cortices, in older adults (Taniwaki et al., 2007).

### ***2.3.5. General Considerations***

The results of the present morphometric analyses provide a clear picture of cortical GM distribution in elderly adults with SVD, and a distinct pattern of GM degeneration across the cortical sheet. Since the RUN-DMC cohort does not include any individuals without SVD, it is difficult from these findings to disentangle the effects of this condition and “normal” aging. On the other hand, given the high prevalence of WML in elderly adults (95% according to de Leeuw et al., 2001), the notion of “normal” aging is perhaps ill-defined to begin with. Our results have an interesting pattern which focuses upon all the usual suspects implicated by functional studies: visual, auditory, and some motor regions, the parahippocampal region, and prefrontal and lateral temporal cortex. Given the wealth of data in the RUN-DMC data set, and the prospect of obtaining longitudinal data in the future, these findings are rather preliminary ones, which set a groundwork for questions which are perhaps more interesting, including: (1.) How well can current morphometric parameters predict future morphometry, and what do these patterns look like at the population level? (2.) To what extent can cortical GM thickness be predicted by WM morphometry, particularly DWI-based tractography? (3.) How does the pattern of degeneration in both GM and WM relate to functional activations (i.e., the resting-state fMRI data which is also available for these individuals)? Can we predict, for example, the functional consequences of WML? (4.) How does all this relate to behavioural measures, such as cognition, depression, memory, motor skills, and sensation? Can we show, for instance, that an active lifestyle or continuing education are related to enhanced function or preserved morphology? These questions are revisited in the General Discussion, below.

### ***2.3.6. Conclusions***

We demonstrate the population-wide distribution of cortical thickness and WML in a large cohort representative of elderly adults with SVD. There are clear effects of age upon cortical thickness, which are targeted to specific cortical regions associated with vision, audition, memory, and executive function, all of which capacities have been observed to degrade with aging. These findings correspond to some extent with existing VBM literature; however, that the pattern differs from that reported in another cortical thickness study (Salat et al., 2004) is somewhat worrisome, as one possible explanation could be the different cortical thickness approximation algorithms used (CLASP versus Freesurfer). Fortunately, these algorithms have been compared by (Lee et al., 2006a), using a brain image “phantom” approach to assess the degree of error in the surface representation. Their results indicate that the CLASP surface has slightly more geometrical accuracy than that produced by Freesurfer (~0.5mm RMS error versus ~0.8mm); no local differences were assessed, however, and it is thus difficult to say how much this slight difference might affect the final morphometric results. The most likely interpretation is that the observed differences were due primarily to real discrepancies between the cohorts.

Given that the RUN-DMC is a prospective follow-up study, the prospect of obtaining longitudinal data presents the possibility of investigating the dynamic progression of cortical thinning both within and across subjects, which would add a very informative temporal aspect to this picture. This has been done previously, for example by in Alzheimer patients, who demonstrate a clear spatiotemporal pattern of degeneration that is highly informative of the cortical regions where this disease typically originates, and how it tends to progress over time. A similar design may demonstrate the origins of the age- and SVD-related thinning reported here, and could potentially help elucidate the interactions between WM and GM degeneration that can only be addressed through correlation in the present cross-sectional state of the data set. An anatomical model of compensatory changes might also be forthcoming from these longitudinal data.

### 3. Shapley Values for Brain Networks

This section describes a novel graph theoretical method for estimating the importance of cortical regions in a structural network, to the global connectivity of that network. This method and its results are published in (Kötter et al., 2007).

#### 3.1. Methods

##### *3.1.1. The Shapley Function*

The Shapley rating (which I shall refer to synonymously with Shapley *value*) was proposed by Lloyd Shapley (Shapley, 1953), within the context of game theory, as a means of fairly assigning the collective profit attained by a *coalition* of players, based upon the relative contribution of each to that profit. We can express this more formally by designating  $N$  as a subset of players in some game  $G$ , and  $S \subseteq N$  to be a subset of players who form a coalition. We can further specify a function  $f : P(N) \rightarrow \mathbb{R}$  which assigns a real-valued profit to the coalition.  $f$  is referred to abstractly as the *characteristic function*; in line with our objective, we want  $f$  to represent network connectivity. By definition, for any  $f$ ,  $f(\emptyset) = 0$ , where  $\emptyset$  is the empty set. A Shapley value is assigned to a vertex by a Shapley function  $\phi_f : N \rightarrow \mathbb{R}$ , where the subscript  $f$  refers to the particular characteristic function, and  $\phi$  is uniquely defined according to the following axioms (Shapley, 1953):

**i. Efficiency**

All profits must be distributed:  $\sum_{i \in N} \phi_f(i) = f(N)$ .

**ii. Symmetry:**

If players  $i$  and  $j$  are interchangeable, their Shapley values must be equal:  $\phi_f(i) = \phi_f(j)$ .

**iii. Additivity:**

The collective profits of two games, defined by characteristic functions  $f$  and  $g$ , are mutually exclusive. The Shapley values obtained from two separate games are thus independent, and the values must be added player by player:  $\phi_{f+g} = \phi_f + \phi_g$ .

A Shapley value for player (or cortical region)  $i$  can be determined by considering the coalition-wise profits for all permutations of  $N$  with and without  $i$ . More intuitively, suppose  $\pi$  is a permutation of the set of all players  $N$ ; if all the players were placed in a queue, then  $\pi$  represents one possible ordering of this queue. Next suppose that, for any given  $\pi$ , a coalition  $p\pi_i$  was formed, consisting of all players in front of  $i$  in the queue. The contribution of  $i$  to  $p\pi_i$  is then the collective profits of this coalition with  $i$ , minus the collective profits without him. As a formula:

$$f(p\pi_i \cup i) - f(p\pi_i)$$

Applied to a single permutation of  $N$ , this distribution scheme would be quite unfair, as it considers only those players ahead of  $i$  in the queue, and is thus not representative of all players. However, Shapley demonstrated that if such a measure is averaged over the set  $\Pi$  of all possible permutations of  $N$  (of which there are  $|N|!$ ), the result is a fair distribution

according to individual contributions. For a characteristic function  $f$ , the Shapley function is given by:

$$\phi_f(i) = \frac{1}{N!} \cdot \sum_{\pi \in \Pi} [f(p\pi_i \cup i) - f(p\pi_i)]$$

### 3.1.2. The Shapley Function for Cortical Networks

Our object here is to formulate the original Shapley rating to refer to cortical networks; i.e., to obtain a measure of how important an individual cortical region is to the connectivity of the entire network. The Shapley function was developed originally for the analysis of game-like systems, but can be abstracted to representations of different types of systems that can be represented as directed graphs, including cortical networks. Such a measure could help elucidate the roles of individual cortical regions within their larger networks, predict the “reachability” of one vertex to all other vertices, or estimate the effect of localized lesions upon the global connectivity of the network.

A method for assigning Shapley values to cortical networks has been proposed previously (Abraham et al., 2006). Since we want to assess a region’s contribution to the global connectivity of the network, we must formulate the characteristic function  $f$  such that it measures global connectivity. This can be done as follows: (1.) We can model our brain network of interest as a directed graph  $G = (V_G, E_G)$ , whose set of vertices  $V_G$  represents the set of cortical regions comprising the network, and whose set of edges  $E_G$  represents the projections connecting them. (2.) We define the concept of *strongly connected components*, in order to describe global connectivity. A graph  $G$  is considered strongly connected if there is a path from every vertex  $i$  ( $i \in V$ ) to any other vertex  $j$  ( $j \in V$ ); that is, if there is a series of projections connecting every cortical region to every other region. If a subgraph of  $G$  is denoted  $G' = V', E'$ , with  $V' \subset V_G$  and  $E' \subset E_G$ , then the set  $SCC(G)$  is an enumeration of all maximal subgraphs  $G'$  which are strongly connected; each of which is called a strongly connected component of  $G$ . Importantly, all such components are by definition disjoint.

$SCC(G)$  can be used to derive a measure of the connectedness of  $G$ . If  $|SCC(G)| = 1$ , then there is a path from any vertex  $i$  to any vertex  $j$  in  $G$ ; i.e., any cortical structure can communicate information to any other through some path of projections. If, on the other hand,  $G$  is comprised of  $n$  disconnected components, the value of  $|SCC(G)|$  is at least  $n$ . Moreover, if we remove a vertex  $i$  from  $G$  (simulating a localized lesion), the value of  $|SCC(G)|$  may change, and we can thus assess the contribution of  $i$  to this value. In general, the number of strongly connected components can be said to be proportional to the global connectivity of the network, and thus can serve as our characteristic function. More formally, for a given vertex set  $V' \subset V_G$ , and edge set  $E'$  comprised of all edges connecting vertices in  $V'$ , we have a corresponding graph  $G' = V', E'$ , for which the characteristic function  $f_g$  is given by:

$$f_g(V') = |SCC(G')|$$

The corresponding Shapley function is:

$$\phi_f(i) = \frac{1}{|N|!} \sum_{\pi \in \Pi} [ |SCC(p\pi_i \cup i)| - |SCC(p\pi_i)| ]$$

## Shapley Values for Brain Networks

Based on the nature of this characteristic function, it is important to note that smaller values of  $\phi_f$  actually correspond to a higher importance to connectivity; thus the Shapley value for brain networks is an inverse measure. A remarkable general feature of this measure is that, if  $G$  itself is strongly connected, then the sum of all Shapley values will be one. Thus, for a randomly connected graph with  $n$  vertices, the expected value of  $\phi_f$  can be described by:

$$E[\phi_f] = 1/n$$

Shapley values for brain networks can thus be assigned meaning relative to this value.

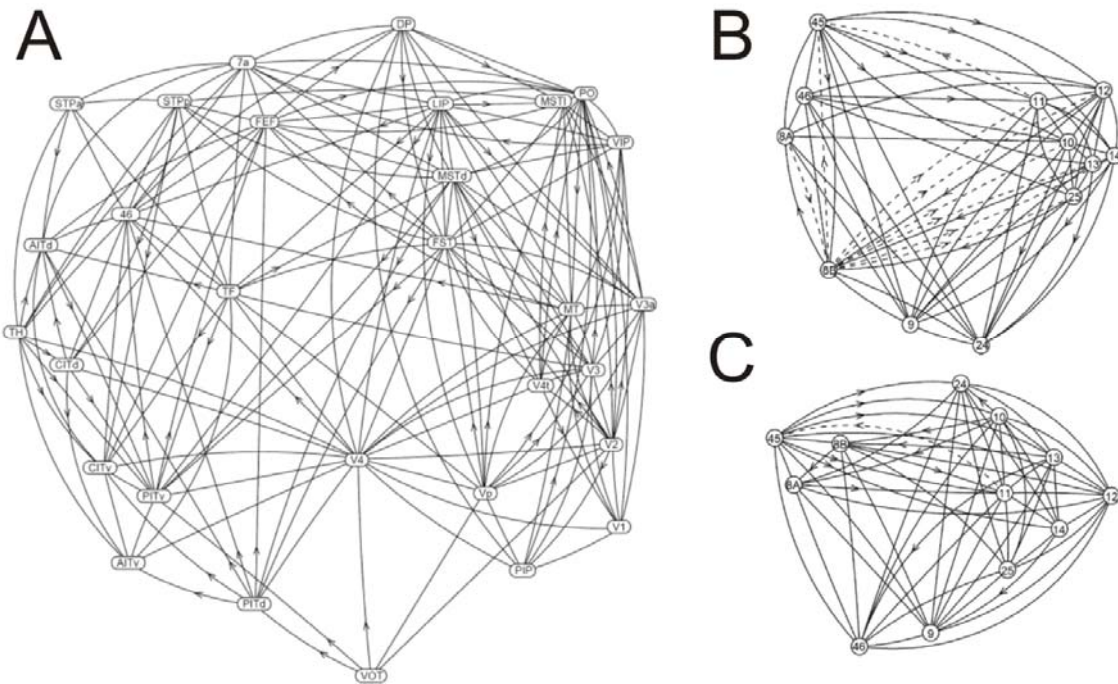


**Figure 3.1.** Cortical networks analyzed for Shapley values. **A:** Visual cortical network from Young (1992) (Y91), showing only connections known to exist. **B:** Original Walker (1940) variants W40-0 and W40-1. **C:** W40-2 variant, assuming that all unknown edges exist. The positions of the vertices are determined using a multidimensional scaling routine (Kötter & Stephan, 2003).

### 3.1.3. Empirical Data

Shapley values were obtained for two separate macaque cortical networks, compiled from tract tracing experiments, and previously described in literature: (1.) a connectivity matrix of visual cortex (Y92) (Young, 1992), comprised of 30 vertices including V1 and several parietal (7a), temporal (TH), and prefrontal regions (Figure 3.1A); and (2.) three variations on a connectivity matrix representing prefrontal cortex (W40) (Walker, 1940), updated from information in the CoCoMac database (Kötter, 2004) (Figure 3.1B,C). The variations are based upon previous publications (Kötter and Stephan, 2003; Passingham et al., 2002; Stephan et al., 2001) as follows: (i.) assuming that an absence of connectivity data corresponds to an actual absence of a connection (W40-0); (ii.) assuming, on the contrary, that all unknown connections actual do exist (W40-1); and (iii.) a third variant, in which the

network connections were specified using an updated version of both the database and the algorithm used to infer connections from unrelated brain maps (W40-2). The W40-2 network had only a single unspecified connection, from area 11 to area 45, which was assumed to be absent.

### ***3.1.4. Statistical Comparisons of Vertex Indices***

A large variety of vertex-wise graph theoretical measures already exist, which describe slightly different aspects of the vertex and its relationship to the network. Kötter and Stephan introduced a number of vertex-wise measures called network participation indices (NPIs), which represent some aspect of a vertex's participation in the network of which it is a member (Kötter and Stephan, 2003). Three indices were proposed: (1.) the *density* of a vertex's connections, or how interconnected it is within the network; (2.) its *transmission* rate, which refers to the ratio of its outgoing connections (outdegree) incoming connections (indegree); and (3.) *symmetry*, which measures how many of a vertex's connections are reciprocal (i.e., include both incoming and outgoing edges). Additionally, for the present dissertation, two versions of symmetry have been defined: (1.) *symmetry-exists*, which only considers existing symmetrical connections; and (2.) *symmetry-all*, which includes the reciprocal *absence* of any connections. Finally, three other measures are considered here, two of which have already been introduced in Section 1.4.5: (1.) the *clustering coefficient* (Watts and Strogatz, 1998), which describes the degree to which a vertex's neighbours are interconnected; (2.) *betweenness centrality* (Freeman, 1977; Honey et al., 2007), which describes how central a vertex is within the network; and *dynamical importance*, which evaluates the effect of a particular vertex upon the maximum eigenvalue of the connectivity matrix, a value which has been used to describe global connectivity in a variety of network paradigms (Restrepo et al., 2006).

Given the substantial number of graph theoretical vertex-wise measures that have been proposed to analyze network connectivity, and the ambiguity of the relationships between them, which their qualitative descriptions are often insufficient to resolve, it is interesting to compare them in a quantitative, statistical manner. Therefore, the relationships of the aforementioned graph measures to the Shapley value was examined in two ways: (1.) by obtain Pearson correlation coefficients for each; and (2.) by performing a stepwise multiple linear regression analysis (using Matlab R2008, Mathworks Inc., Natwick, MA), in which the measures are treated as factors in a linear model predicting the Shapley value, and each factor was added stepwise until their addition no longer resulted in a significant change in the model's predictive power. These analyses were performed for the Y92 network, the W40 network, and on a set of 5000 randomly generated 4- to 11-vertex networks.

### ***3.1.5. Lesioned Networks***

One potentially important application of Shapley values is their application to clinical situations, for instance to predict the consequences of focal brain lesions upon network connectivity. To assess the impact of such lesions on the distribution of Shapley values in a network, we removed single regions from the W40-2 network and recomputed Shapley values for the remaining vertices.

## 3.2. Results

### 3.2.1. Intact Networks

Here I report Shapley values calculated for intact versions of the four networks introduced in above.

#### 3.2.1.1. Y92 network

The Y92 network is comprised of 30 cortical regions; therefore, the expected Shapley value is  $1/30 \cong 0.333$ . The Shapley values of Y92 are shown in Figure 3.2. V4 has the most negative value (which indicates the highest importance to global connectivity), having a value which is more than twice that of the next important region, FEF. Other regions with similarly low values are 46, V2, VP, MSTd, and 7a. Both PITd and VOT have relatively high Shapley ratings, indicating that their existence in the network does not contribute substantially to its overall connectivity. Other regions with high Shapley values are PITd, CITd, V4t, STPa, PITv, and AITd.

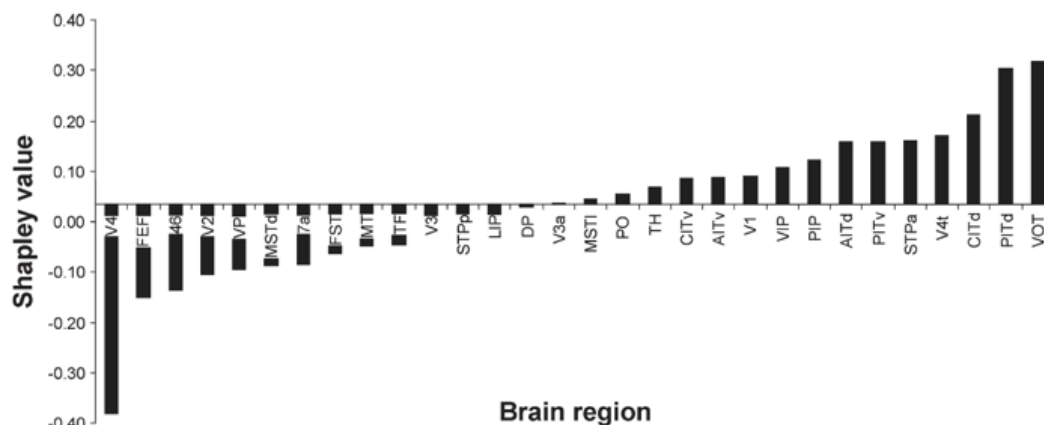


**Figure 3.2.** Shapley values for the Y92 network. The x-axis is located at 0.333, which is the expected value for a 3-vertex graph.

#### 3.2.1.2. W40 networks

Since each of the W40 variants have 12 regions, the expected Shapley value for these networks is  $1/12 \cong 0.083$ . The Shapley values for the W40 networks are shown in Figure 3.3. The choice of connection type (existing or not) for unknown relationships, as captured in these variants, appears to have significant effects upon the role of its nodes in supporting global connectivity. Notably, both areas 9 and 24, which have a high relative importance in the W40-0 network, have substantially less importance in the other two variants. Area 12, conversely, increases its importance in these two networks. Area 8B and to a lesser extent area 45, which have high relative Shapley value in W40-0, gain in importance in W40-1 and W40-2.

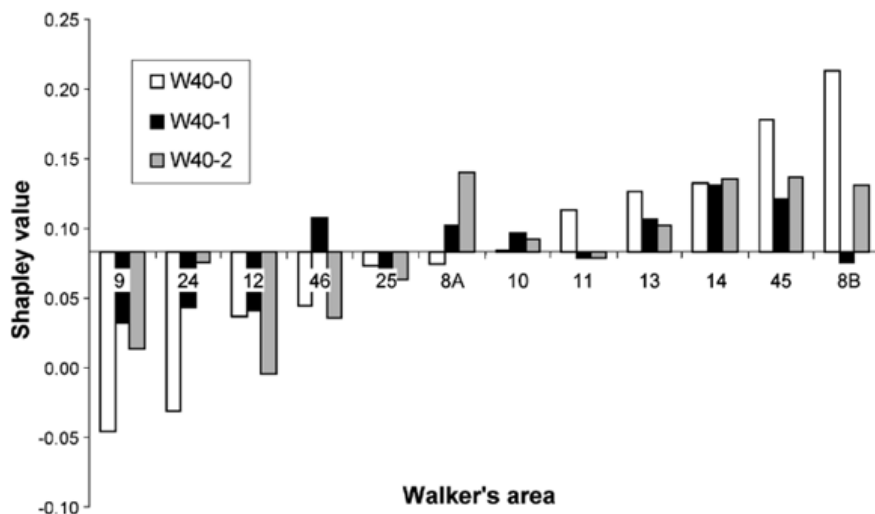


**Figure 3.3.** Shapley values for the three W40 variants, sorted by the values for W40-0. The x-axis is located at 0.083, the expected value for a 12-vertex graph.

### 3.2.2. Comparison with Other Measures

Correlations between Shapley values and other vertex-wise measures of network connectivity (introduced in 3.1.4) are shown in Table 3.1, for both the Y92 and W40 networks, as well as for values obtained from 5000 randomly-generated 11-vertex graphs. Remarkably, only transmission does not show a significant correlation for any of the three versions, while symmetry is insignificant at the  $\alpha = 0.05$  level for the Y92 network. Three of the measures (density, symmetry, and centrality) show a negative correlation with Shapley values, which might be considered positive due to the inverted nature of the measure. Two other measures (clustering and dynamical importance) are positive correlated (the latter is also an inverted measure of importance).

**Table 3.1.** Comparison of network measures. Pearson correlation coefficients ( $r$ ) and associated  $p$ -values, for six vertex-wise network measures with the Shapley value, for Y92, W40, and random graphs.

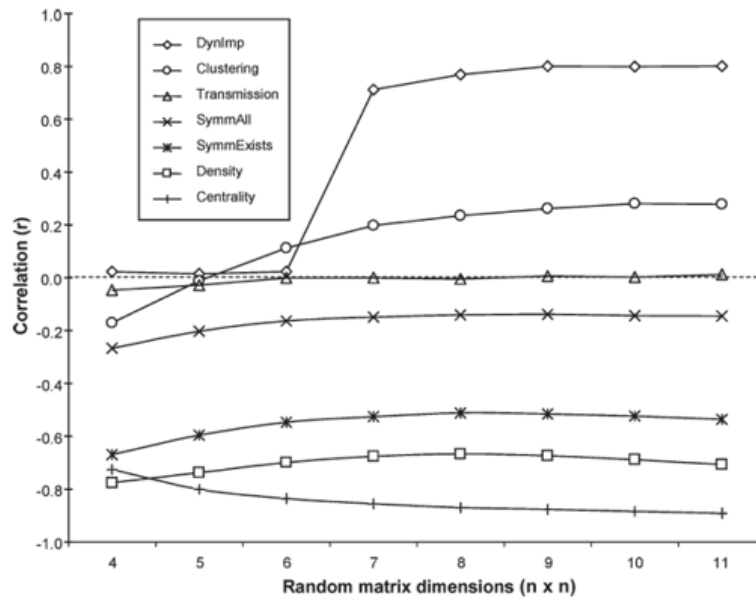
NPI	Network					
	Y92 (Visual)		W40 (Prefrontal)		Random (11 nodes)	
	$r$	$p$	$r$	$p$	$r$	$p$
Transmission	-0.452	0.069	0.277	0.408	0.012	0.700
Density	-0.873	0.000	-0.914	0.000	-0.707	0.000
Symmetry	-0.362	0.153	-0.747	0.018	-0.537	0.000
Clustering	0.702	0.002	0.707	0.012	0.278	0.000
Centrality	-0.846	0.000	-0.908	0.000	-0.891	0.000
DynImp	0.797	0.000	0.943	0.000	0.801	0.000

Values are shown for both of the two empirically based networks presented in this paper, as well as a set of 5000 randomly generated 11-node networks.

The relationship of these correlations with the size of the network were further investigated by varying the size of the randomly-generated graphs. The result of this is illustrated in

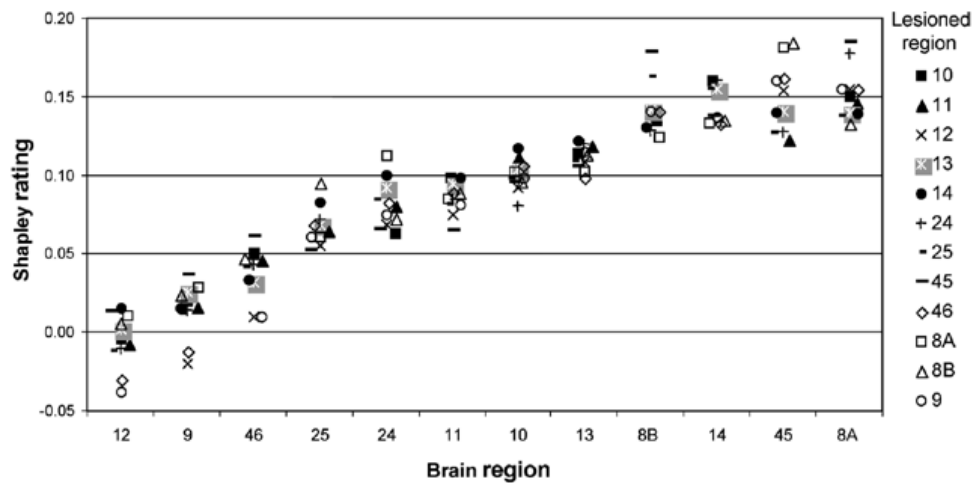
## Shapley Values for Brain Networks

Figure 3.4. While correlations for graphs of size 7 and higher appear to be stable, graphs below this size are not. This is particularly the case for the dynamical importance measure.



**Figure 3.4.** Correlation coefficients calculated between six vertex-wise graph measures, for random networks of sizes ranging from 4 to 11.

Given the strong correlations between some of these measures, it is also of interest to investigate the extent to which they can (alone or in combination) account for the variance in the Shapley value. This was tested with multiple linear regression (performed interactively in Matlab), using data obtained from the random 11-node graphs, which identified betweenness centrality as the measure best explaining Shapley values ( $R^2 = 0.789$ ). Individually, density, symmetry, and dynamical importance added similarly to the power of the betweenness centrality model ( $R^2 = 0.838$ ,  $0.855$ , and  $0.816$ , respectively), whereas clustering coefficient and transmission added virtually nothing to the model.



**Figure 3.5.** Simulated focal lesions. Shapley values for each brain region in the network after one of the other regions (indicated by the symbols at right) is removed (or “lesioned”).

### 3.2.3. Lesioned Networks

Figure 3.5 shows the vertex-wise Shapley values for the W40-2 network, after single regions had been removed from the network (thus simulating a focal lesion of that region). The expected value for this new network is  $1/(12 - 1) \cong 0.091$ . Three areas (12, 19, and 46) always had the lowest Shapley values, regardless of the removal of other areas; two of these three areas also increased in importance if one of the others was lesioned. When all Shapley values in the graph are considered, it is interesting to note that the loss of 8A, 12, 46, 8B, and 9 all result in an increase in the range of values, whereas the loss of 45 results in a decrease (Figure 3.6). The range of values does not show a clear relationship to the Shapley value for the removed vertex, however.

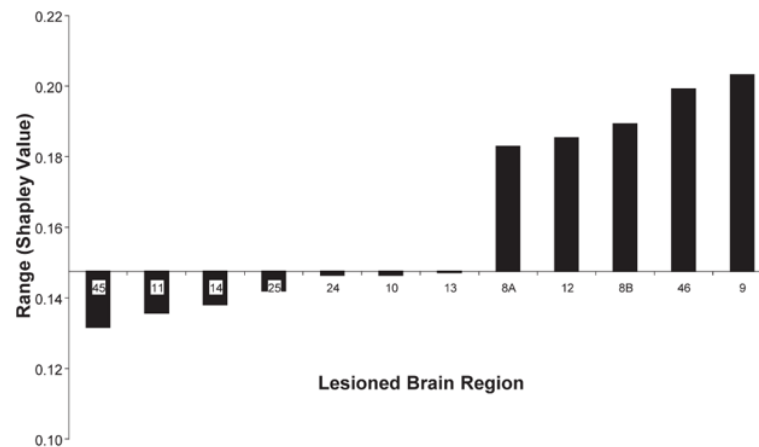


**Figure 3.6.** Ranges for the Shapley values of the remaining regions, after a region (shown on abscissa) is removed from the network. The level of the abscissa is the value of the Shapley value range for the intact network.

## 3.3. Discussion

With the increasing complexity of connected brain network models derived from ever-improving data acquisition methods, there is a corresponding rise in the demand for novel theoretical methods with which to analyze them. The adaptation of graph- and game-theoretical methods is naturally suited to such a purpose. The Shapley value was initially introduced as a means of analyzing the contribution of individuals to some coalition within a game, which abstraction was more or less intended for applications within economics. The value of mathematical abstraction, however, is that it allows a theory to be applied in fields where it was never originally intended: in the present case, to structural brain networks. In this section I discuss the results of analyzing a number of brain networks with the Shapley value, how this relates to existing graph theoretical measures, and the implications of such a measure in the broader context of neuroscientific research and clinical practice.

### ***3.3.1. Intact networks***

#### ***3.3.1.1. Y92 network***

Analysis of the Y92 network shows that area V4 has a substantially lower value than any of its counterparts (Figure 3.2) (recall that a negative score indicates a higher importance for global connectivity). This result accords with reports that V4 is a particularly densely connected region within the visual network (Felleman and Van Essen, 1991), has a high betweenness centrality (Honey et al., 2007), and that its removal results in a decrease of the small-worldness of the remaining network (Sporns et al., 2007). After V4, frontal eye field (FEF) and area 46 (lateral prefrontal cortex) are next in importance, although as these are the only frontal regions in the network, their importance must be considered in context to the limited network under investigation (i.e., their values might change considerably with the inclusion of other frontal regions). Other regions with low Shapley values include the densely connected structures of the prestriate cortex (V2, V3, VP) and regions associated with the dorsal visual stream (MSTd, 7a, MT, STPp, LIP, DP). Regions with high Shapley values include V1 (whose subcortical input is not included) and ventral visual stream regions, notably subregions of inferotemporal cortex (IT), possibly because of the high degree of redundancy between these subregions.

#### ***3.3.1.2. W40 networks***

The first version of the W40 network (W40-0) followed previous convention by omitting any connections for which there was no empirical evidence. This macaque prefrontal network has been previously investigated by (Passingham et al., 2002). In that study, the authors introduced the idea of a “connectional fingerprint”, which can uniquely identify a region through its connectivity pattern; furthermore, these fingerprints could be used as a basis for organizing regions into clusters. The three most negative regions (9, 24, and 12) and the three most positive regions (8B, 45, and 14), each belong to separate clusters defined in that (Passingham et al., 2002), which suggests that the Shapley value may provide a means of assigning the importance of these regions in terms of their ability to communicate with clusters external to their own. Moreover, it is possible that small differences in connectional fingerprints can result in substantial differences in their importance to global connectivity. Another interesting observation is that two of the four regions with the lowest Shapley values in this variant, 24 and 46, are among the most regularly activated across a variety of functional imaging paradigms, and have also been reported to activate less in individuals with attention deficit hyperactivity disorder in children and adolescents (Dickstein et al., 2006).

A second variant of W40, W40-1, resulted from making the opposite assumption that all unknown connections do exist. This had a number of effects on the resulting Shapley values. Firstly, the overall range of values decreased, due to the increased connectivity of the graph (and thus the less importance of any one vertex). Region 8B, whose connections were primarily affected by this change, had its value change from very positive to slightly negative, indicating that this choice of assumption regarding uncertain connectivity has a non-negligible impact on the resulting graph measure. A third variant, W40-2, was obtained by integrating updated mapping data in the CoCoMac database, resulting in a somewhat different connectivity structure (see Figure 3.3B). This modified structure had the effect of reducing the importance of 9, 24, and 8A, and increasing the importance of 12, 45, and 8B. It is tempting to speculate that these changes are attributable to one additional edge between

8B and 45, which appears to reorganize the clustering of this network, although an edge-based graph measure could more conclusively address this.

### ***3.3.2. Comparison of Vertex-wise Graph Measures***

Given the large number of available metrics which are meant to capture different aspects of a graph's connectivity, it is interesting to assess the degree of dependence between these measures and the Shapley value. Based upon the results in Table 3.1, it appears that, of the measures tested, only transmission is completely uncorrelated with the Shapley value. Both betweenness centrality and dynamical importance correlate very highly (-0.891 and 0.801 respectively, for random graphs), while density and symmetry show more moderate correlations. This accentuates the notion that betweenness centrality is a useful measure of a vertex's importance to graph connectivity, and this appears to hold true for graphs of size 7 or larger (Figure 3.4), although it is important to note the ~20% residual variance, which indicates that the measures are capturing slightly different aspects of the graph structure (i.e., they are not completely redundant). Additionally, combining any two measures does not substantially raise the amount of explained variance ( $R^2$ ) in the Shapley values (from 0.789 to 0.838 at most).

### ***3.3.3. Lesioned Network***

One potential application of the Shapley value is to assess the effects of a localized lesion to part of the network. We simulated such lesions by removing each region from the W40-2 network, and recalculating Shapley values for the remaining network. Two observations are particularly striking from these results (Figure 3.5): (1.) Regions 12, 9, and 46 retain the lowest Shapley values for almost every lesion (with the exception of 45), and these values increase significantly for two of these regions when the other is lesioned. (2.) Removal of area 45 has the most profound effects on the network. Firstly, it reduces the importance of area 46, which suggest that a large part of this importance is as a connector for 45. Secondly, it reduces the values of both 8A and 8B, supporting the speculation made above, that the 45-to-8B connection is indeed responsible for much of the differences in Shapley values seen in W40-2, compared to its counterparts. As a result of these changes, removal of area 45 also results in a decrease in the range of Shapley values across the entire network. In general, these results predict that the prefrontal network would be most sensitive to lesions in area 45, a prediction which is supported by its high transmission index (Kötter and Stephan, 2003). Given its low Shapley rating, a lesion to this region would not be expected to greatly affect global connectivity, but may instead have functional implications for specific regions in the remaining network, particularly areas 46, 8A, and 8B, which share similar connectional fingerprints.

### ***3.3.4. General Considerations***

The brain of humans, macaques, and other organisms have been shown to have small world properties (Watts and Strogatz, 1998) as well as being "scale-free" networks, a property which affords them general robustness to degradation, at the cost of having a number of "hub" nodes whose degradation is catastrophic (Albert et al., 2000). Such hub nodes can be identified by a number of static graph measures such as betweenness centrality, or by assessing the cost to connectivity of their removal, which is the effective purpose of the Shapley value as described here. These observations are particularly relevant to the study of focal lesions, as well as the more distributed type of degradation observed in the aging brain

(see Section 1.7.2). In the latter case, the investigation of cortical regions should be augmented by a consideration of the projections between them, especially given that 95% of adults aged 60 to 90 have some degree of WML (de Leeuw et al., 2001) and that WML severity is related to a factor-of-three increase in cognitive impairment (De Groot et al., 2002). Thus, it would be useful to extend the Shapley value introduced here to graph edges, an approach which may complement existing measures of edge importance, such as the four measures proposed by Kaiser and Hilgetag (Kaiser and Hilgetag, 2004).

This dialogue also ties in closely with the morphometric analyses of the RUN-DMC cohort, in which I utilize empirical methods to measure cortical thickness, WML volume, and anisotropic diffusion, and thereby obtain estimates of both GM and WM integrity. Realistic structural networks constructed with such methods can be used to alter the corresponding “canonical” network, such as the Y92, W40, or FVE91 networks presented in this dissertation. Theoretical measures of node or edge importance can then conceivably be compared against structural or even functional observations, and the utility of a given measure can be assessed in terms of its predictive power. These ideas will be further expanded in the general discussion, below.

### ***3.3.5. Conclusions***

The Shapley value graph measure introduced here is a novel means of assessing the relative importance of a cortical region to the connectivity of the brain network of which it is a part, and is closely related to, but appreciably distinct from, both betweenness centrality and dynamical importance. Here I report Shapley values for two cortical networks, derived from macaque tract tracing information: (1.) a visual network from Young (1992); and (2.) a prefrontal network from Walker (1940). For the latter network, the resulting highest and lowest values are found in regions which have been previously differentiated into clusters by (Passingham et al., 2002), thus adding new insight into the anatomical organization of this network. We also find that the assumptions regarding unknown connections (i.e., whether they should be considered absent or present), has a substantial impact upon the range and ordering of the resulting Shapley values, emphasizing the importance of a data completeness for these types of analyses. Finally, this measure is used to investigate the effect of simulated focal lesions on the connectivity of the W40-2, confirming the importance of areas 12, 9, and 46 to the global connectivity of the prefrontal network, and also highlighting area 45 as a region which can account for much of the importance of the other regions.

## 4. Optimization of Cortical Hierarchies

### 4.1. Methods

This section describes a method which extends the ideas of Felleman and Van Essen (1991), Hilgetag et al. (1996), and others (introduced in Section 1.4.4). The following methodology and results are published in Reid et al. (2009).

#### 4.1.1. Graph Representation and the Hierarchy Function

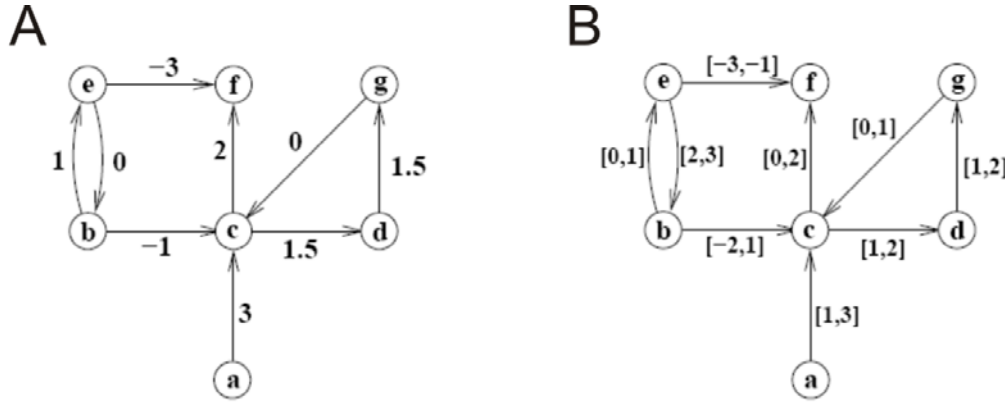


**Figure 4.1.** Two directed graph representations of a hierarchical cortical network. **A:** Real-valued edge weights represent absolute hierarchical distances. **B:** Real-valued intervals represent a range over which hierarchical distances can vary.

We start by representing a cortical network of interest as a weighted, directed graph  $G$ , with vertex set  $V$  and edge set  $E$ . If  $(i, j) \in E$  is the edge from vertex  $i \in V$  to vertex  $j \in V$ , we can assign a weight  $x$  to each such edge representing the *hierarchical distance* from  $i$  to  $j$  (Figure 4.1). The sign of  $x$  represents its direction (ascending or descending), and  $x = 0$  means that  $i$  and  $j$  are on the same level. Given this model, we can define a function  $h : V \rightarrow \mathbb{R}$ , such that:

$$h(i) + x = h(j)$$

where  $h$  is called the *hierarchy function*.

We can refine this model to allow a more flexible representation of hierarchical distance, by replacing the weight  $x$  with a continuous range of values. In this refinement, for every edge  $(i, j)$ , there is an interval  $[x, y], x, y \in \mathbb{R}$  (Figure 4.1). This interval defines a constraint bounding the hierarchical distance from  $i$  to  $j$ , and results in a modification of the hierarchy function to a pair of inequalities:

$$h(i) + x \leq h(j) \quad \text{and} \quad h(i) + y \geq h(j)$$

Finally, we can further modify  $h$  to accommodate the uncertainty of the empirical data, with the inclusion of a deviation term  $\Delta$ . For a single-weighted edge, the hierarchy function becomes:

$$h(i) + x - \Delta \leq h(j) \quad \text{and} \quad h(i) + x + \Delta \geq h(j)$$

For a range-weighted edge, it becomes:

$$h(i) + x - \Delta \leq h(j) \quad \text{and} \quad h(i) + y + \Delta \geq h(j)$$

These inequalities allow us to obtain an optimal hierarchy for  $G$ , by minimizing  $\sum \Delta_{ij}$  over all edges in  $E$ , where  $\Delta_{ij}$  is the deviation for edge  $(i,j)$ . This optimization is performed using linear programming (see, for instance, (Papadimitriou and Steiglitz, 1998)). In brief, the aim of linear programming is the optimization of a linear objective function, subject to linear equality and inequality constraints, such as we have defined above.

### 4.1.2. Empirical Data

For the optimization constraints we can adopt the following notation:

- A+ *Strongly ascending*
- A *Ascending*
- D *Descending*
- D+ *Strongly descending*

We performed linear programming optimization (QSOPT Linear Programming Solver, 2008) on two published data sets: (1.) the original data from Felleman and Van Essen (1991) (FVE91), excluding regions MDP and MIP, for which no constraints are defined; and (2.) a second data set, which examines the connectivity of the macaque visual system using cell-counting techniques, and thus permits the use of the SLN% value (Barone et al., 2000) (see Section 1.4.4).

#### i. FVE91

Constraints for FVE91 were defined by assigning ranges to projections, in one of two ways: (1.) based upon assumptions implied in the original paper, specifically D:  $[-99,1]$ , L:  $[0,0]$ , and A:  $[1,99]$ ; and (2.) a modified version of the original classification scheme, incorporating the idea that the specific laminar pattern can provide distance, as well as direction information (Kennedy & Bullier, 1985; Barone et al., 2000; Batardière et al., 2002). This modified scheme is illustrated in Figure 4.2. To investigate the effect of range size and overlap upon the resulting optimization, ten constraint sets were defined, by systematically expanding range limits by increments of 0.1, with the exception of the comparatively large outer limits, which we set at 32 (the total number of cortical regions). The resulting constraint sets are shown in Table 4.1.

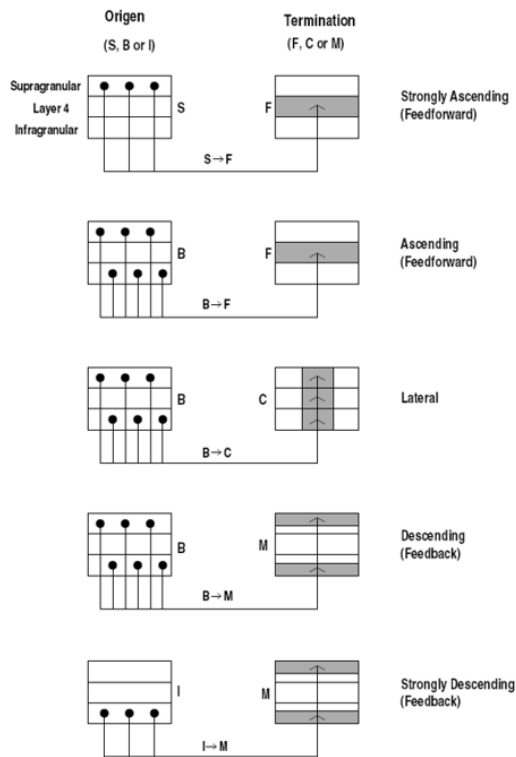


**Figure 4.2.** Modified projection scheme from FVE91, add strongly ascending and descending constraints.

## ii. SLN%

Using cell counting techniques, Barone et al. (2000) report that the proportion of retrogradely labelled neurons in the supragranular layers of visual cortical areas (referred to as SLN%) correlates strongly with the hierarchical rank (according to FV91) of the target structure. This suggests that the SLN% measure can be used as a real-valued hierarchical distance parameter specifying a more refined constraint on the cost function used to determine the optimal hierarchical model. This possibility was investigated using a second visual network, obtained from Barone et al. (2000), based on the assumption that SLN% values are directly comparable, and thus assigning these values directly as edge weights.

**Table 4.1.** Constraint sets specifying ranges for the modified FVE91 scheme.

Class	Set 0		Set 1		Set 2		Set 3		Set 4		Set 5		Set 6		Set 7		Set 8		Set 9	
	From	To	From	To	From	To	From	To	From	To	From	To	From	To	From	To	From	To	From	To
A+	-32	-2	-32	-1.9	-32	-1.8	-32	-1.7	-32	-1.6	-32	-1.5	-32	-1.4	-32	-1.3	-32	-1.2	-32	-1.1
A	-1	-1	-1.1	-0.9	-1.2	-0.8	-1.3	-0.7	-1.4	-0.6	-1.5	-0.5	-1.6	-0.4	-1.7	-0.3	-1.8	-0.2	-1.9	-0.1
L	0	0	-0.1	0.1	-0.2	0.2	-0.3	0.3	-0.4	0.4	-0.5	0.5	-0.6	0.6	-0.7	0.7	-0.8	0.8	-0.9	0.9
D	1	1	0.9	1.1	0.8	1.2	0.7	1.3	0.6	1.4	0.5	1.5	0.4	1.6	0.3	1.7	0.2	1.8	0.1	1.9
D+	2	32	1.9	32	1.8	32	1.7	32	1.6	32	1.5	32	1.4	32	1.3	32	1.2	32	1.1	32

### 4.1.3. Interregional Correlations

To get an idea of the stability of interregional hierarchical distances across constraint sets, we obtained correlations for each interregional pair across all ten constraint sets. Given a network graph  $G$ , and cortical regions  $i$  and  $j$  ( $i \neq j; i, j \in G$ ), and denoting the hierarchical distance between them as  $d(i, j)$ , the vector  $\mathbf{d}_i$  is then the enumeration of all such distances:

$$\mathbf{d}_i = [d(i, 0), \dots, d(i, k), \dots, d(i, 9)]$$

From each pair  $\mathbf{d}_i$  and  $\mathbf{d}_j$ ,  $i \neq j$ , we can obtain a correlation  $r_{ij} = \text{corr}(\mathbf{d}_i, \mathbf{d}_j)$ , which is an indication of the stability of the relative positions of  $i$  and  $j$  across different constraint sets.

## 4.2. Results

### 4.2.1. FVE91 Original

Figure 4.3 shows a comparison between the original hierarchy from Felleman and Van Essen (1991), and the hierarchy produced here, by minimizing  $\sum \Delta_i$ , the sum of deviations from the constraints described in Section 4.1.1. Due to the nature of our constraints (i.e., steps of either 0 for lateral, or at least 1 or -1 for non-lateral projections), the hierarchy obtained through this optimization is expressed on discrete levels, like the original. While the two hierarchies have in general a close correspondence, a number of discrepancies are notable. Particularly, AITd is located at the top of our hierarchy, whereas it is substantial lower in the original. V4 is placed on its own level in the new hierarchy, whereas it shares a level with other regions in FVE91. Comparing the hierarchies quantitatively, we find that within the framework of our constraint set the resulting optimal hierarchy has  $\sum \Delta_i = 11$  and 9 total

## Optimization of Cortical Hierarchies

violations (projections having  $\Delta_i > 0$ ), while the original FVE91 has  $\sum \Delta_i = 17$  and 12 total violations.

	Minimizing $\sum \Delta_i$		Hierarchy from [FE91]
$\sum \Delta_i$ :	11		17
number of constraints with $\Delta_i > 0$ :	9		12
	Hierarchy levels		
	AITd	10	
	46 TH	9	46 TF TH
	FEF TF STPa	8	STPa AITd AITv
	7a STPp CITd CITv	7	7a FEF STPp CITd CITv
	DP VIP LIP MSTd MSTl FST PITd PITv	6	VIP LIP MSTd MSTl FST PITd PITv
	AITv PO MT VOT V4t	5	DP VOT
	V4	4	MDP MIP PO MT V4t V4
	PIP V3A	3	PIP V3A
	V3 VP	2	V3 VP
	V2	1	V2
	V1	0	V1

**Figure 4.3.** Optimization of FVE91 with original constraints. **Left:** Hierarchy obtained by minimizing  $\sum \Delta_i$ . **Right:** Original hierarchy from Felleman and Van Essen (1991).

### 4.2.2. FVE91 Modified

The results of using modified constraints, as introduced in Section 4.1.2, are shown in Figure 4.4. Mean hierarchical positions across the ten constraint sets are qualitatively stable, with a small degree of variation; V1 appears at the bottom and AITd at the top for all hierarchies generated. Notably, groups of regions appear to form clusters in which they are interchangeable, while clusters are distinguishable from one another. As is clear from Figure 4.4, the number of discrete violations for a region is not related to its hierarchical level ( $r = 0.0097$ ,  $t = 0.051$ ,  $p > 0.05$ ).

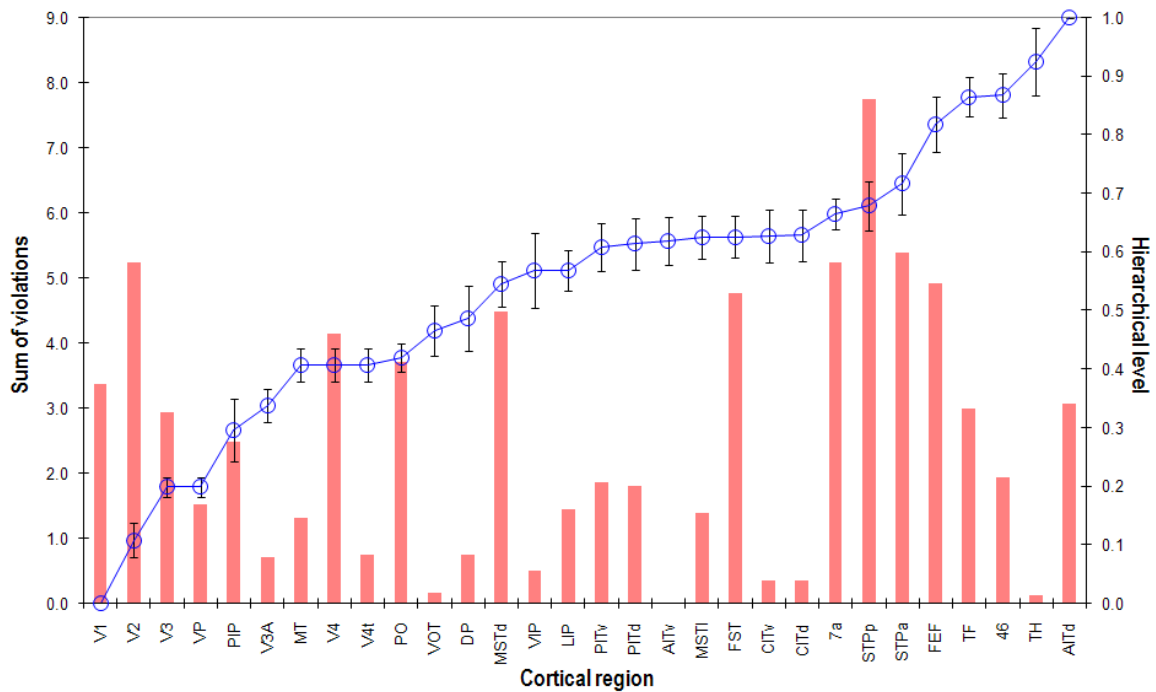


**Figure 4.4.** Hierarchies obtained through the modified constraints for FVE91, across 10 constraint sets (see [Table ?](#)), sorted by mean hierarchical position. **Blue line:** the mean hierarchical position across sets (right ordinate axis), with standard deviation. **Pink bars:** the sum of violations,  $\sum \Delta_i$ , for each cortical regions, across all sets (left ordinate axis).

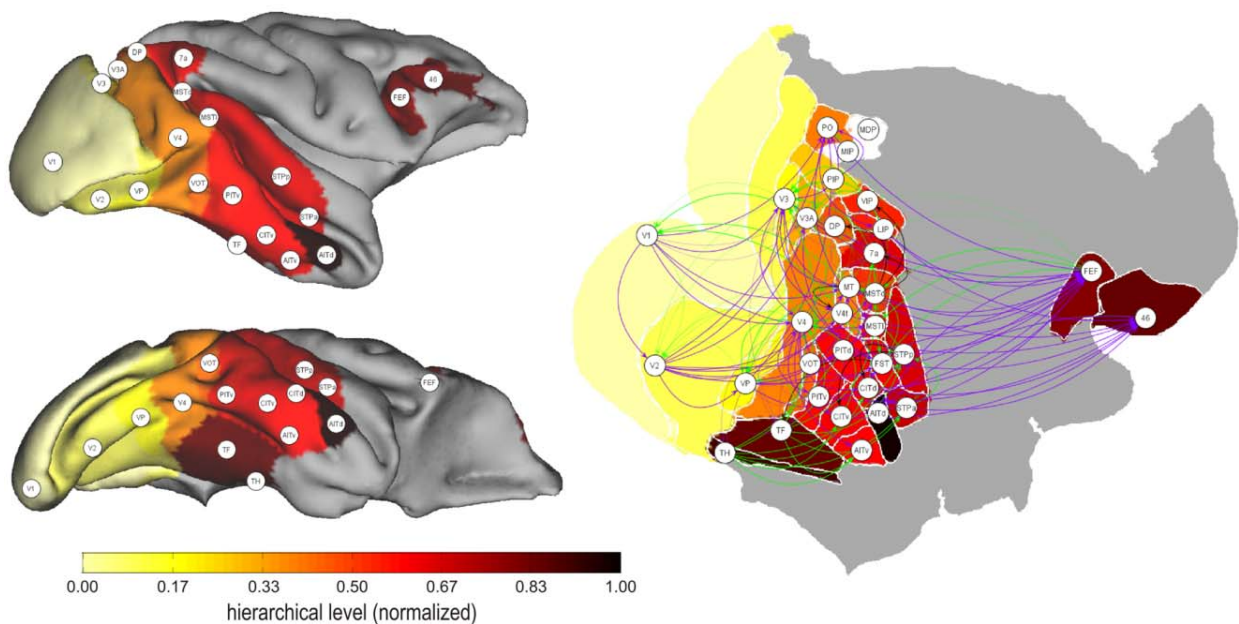


**Figure 4.5.** The mean cortical hierarchical level distributed across the macaque cortex (F99UA1). Means are obtained by optimizing with modified constraints for FVE91. Both fiducial and flat map representations are shown. Arrows represent hierarchical relationships: green = descending, black = lateral, purple = ascending. Hierarchical distance is represented by edge transparency.

Figure 4.5 illustrates the geometrical distribution of the mean hierarchy, both as three-dimensional cortical surfaces and a flat map representation, which also portrays the structural connectivity of the visual network. Figure 4.6 shows correlations across all ten constraint sets, of the normalized hierarchical distance between cortical regions. All correlations are quite high, given the consistency of the ordering as seen in Figure 4.4, but their variance can be compared to get an idea of interregional consistency across differing constraints. Two clusters of regions,  $\{V3, VP\}$  and  $\{MT, V4, V4t\}$  are perfectly correlated, and have zero distance and zero variance, indicating that they always lie on precisely the same level. The distances between subdivisions of cortical region CIT (CITv and CITd) have a high correlation ( $r = 0.9997$ ), and relatively small mean distance (0.0018) and standard deviation (0.0054). Similarly, the subdivisions of region PIT (PITv and PITd) are highly correlated ( $r = 0.9976$ ) and have a relatively small mean distance (0.0054) and standard deviation (0.0161). By contrast, the two subregions of region AIT (AITv and AITd) now fall widely apart with  $r=0.9859$  with a mean distance of 0.381 and standard deviation of 0.0389.

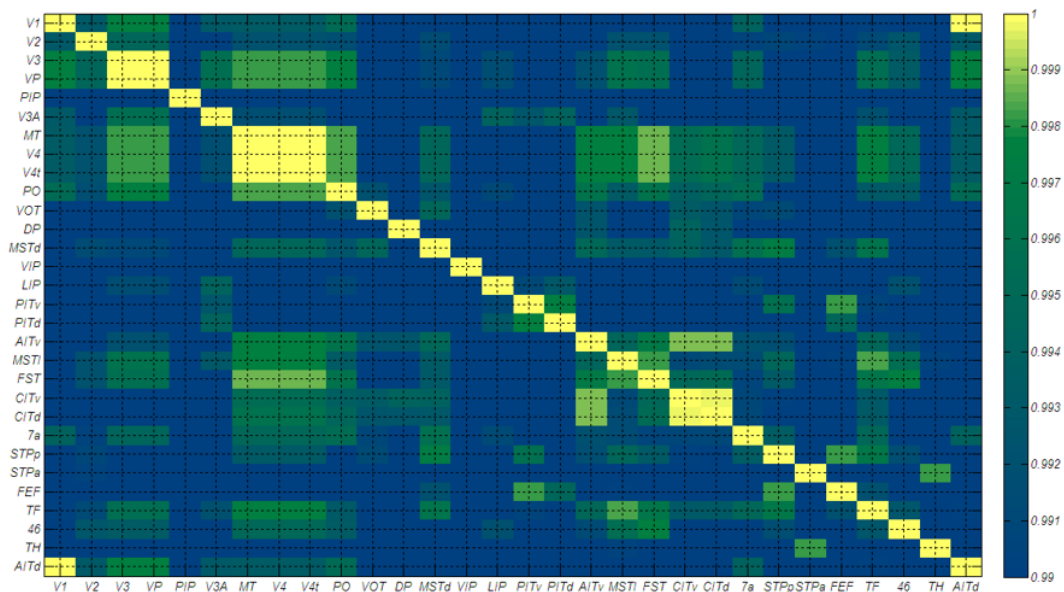


**Figure 4.6.** Correlations across ten constraint sets, of interregional distance

#### 4.2.2.1. Alternative optimization criteria

So far we have utilized the sum of constraint deviations  $\sum \Delta_i$  as the sole criterion for our optimization. While this choice seems logical, others are possible, including: (1.) the number of violations (i.e., instances where  $\Delta_i > 0$ ), and (2.) the maximal deviation  $\Delta_{max}$ . To test the effect of adding these objectives to the optimization, we obtained two additional sets of hierarchies, adding (with appropriate weights) (1.) the number of violations as a second objective, and (2.) all three criteria together (Krumnack et al., 2010). The inclusion of these criteria did result in smaller values for their respective factors, but did not result in any substantial changes to the resulting hierarchy. Nine constraints in particular were identified as consistent offenders across all minimization objectives, which are shown in Table 4.2.

**Table 4.2.** Projections which produced violations in all constraint sets, for all objective criteria.

Origin	V4	AITd	STPp	STPp	V2	V2	PO	PO	FST
Termination	V1	7a	FEF	FST	V3	VP	MSTd	LIP	TF
D+	-	-	-	1	-	-	-	-	-
D	1	1	1	-	-	-	-	-	-
L	-	1	-	-	-	-	-	-	1
A	-	1	-	-	-	-	-	-	-
A+	-	-	-	-	1	1	1	1	-

#### 4.2.3. Barone et al. Network

Figure 4.7 shows the hierarchy resulting from the optimization of the Barone et al. (2000) visual network, expressed in normalized arbitrary units. While the resulting hierarchy is similar to that reported earlier with these data (Vezoli et al., 2004), a number of large discrepancies are apparent between the original SLN% values and the resulting hierarchical distances. These differences are largest for the uppermost regions of the network (THTF, FST, LIP, TE).

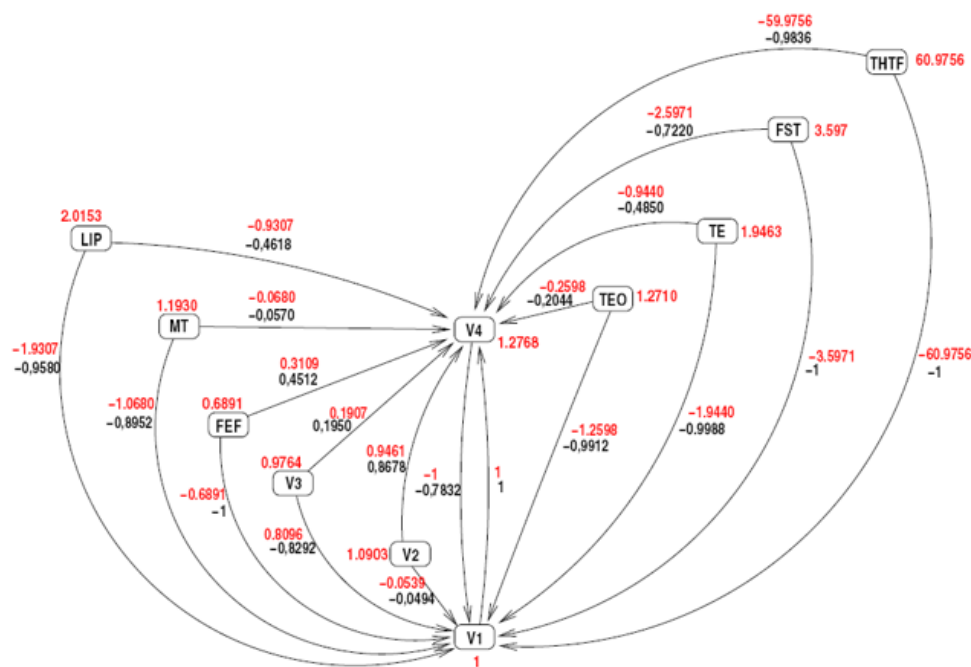


**Figure 4.7.** Hierarchy produced from Barone et al. (2000), using SLN% as a hierarchical distance constraint, and minimizing  $\sum \Delta_i$ . Black numbers indicate the original SLN% value, and red numbers indicate hierarchical distance (for edges) and position (for regions) following optimization.

### 4.3. Discussion

Since its initial proposal (Maunsell and Van Essen, 1983), and implementation (Felleman and Van Essen, 1991), the observation that the laminar source and termination patterns of interregional projections could describe relative hierarchical positions has been a popular

one. A cortical hierarchy constrained by anatomical observations has the potential for establishing a data-driven functional organization of neocortex, which can then be directly compared to model-driven predictions; i.e., it can be potentially used to “reverse-engineer” the computational machine that we call the primate brain. Since the original proposals by Felleman and Van Essen, the study of cortical hierarchies has advanced somewhat: while Hilgetag et al. (1996) demonstrated an apparent indeterminacy with the methodology, given the available data, others have suggested a refinement of the anatomical constraints, using relative supra- or infragranular labelling as a measure of hierarchical *distance*. My colleagues and I (Reid et al., 2009) have attempted to extend this dialogue, by replacing discrete levels with continuous values, and by refining the constraint set to include a representation of hierarchical distance. Here I discuss our results and their implications for the future.

### ***4.3.1. Optimization of the FVE91 Network***

#### ***4.3.1.1. Comparison with original hierarchy***

Minimizing the sum of deviations for the FVE91 network graph with respect to a constraint set analogous to that used by Felleman and Van Essen (1991), and identical connectivity information, yielded a hierarchy with 9 constraint violations; the original hierarchy, by comparison, violated 12 constraints (Figure 4.3). While the two hierarchies are similar, two notable differences are the placement of anterodorsal inferotemporal cortex (AITd) firmly at the top of the hierarchy, while it is placed on the second highest level in the original, and the placement of anteroventral inferotemporal cortex (AITv) much lower than its original position. These results are interesting in light of two findings by Saleem and colleagues: (1.) that AITv projects more densely to perirhinal cortex than does AITd (Saleem and Tanaka, 1996); and (2.) that AITd receives denser projections from the upper bank of the superior temporal sulcus (STS), also known as the superior temporal polysensory area (STP), while AITv receives denser projections from the lower bank (Saleem et al., 2000). This differential parallel projection pattern, derived from information which was unavailable in the original publication, predicts that AITd and AITv may assume different hierarchical roles. On the other hand, (Tamura and Tanaka, 2001) report that single cell recordings from both these areas show little difference in either minimal response latencies or sharpness of stimulus selectivity, on which basis they argue for a hierarchical equivalence between these regions (but see Section 4.3.3, below).

#### ***4.3.1.2. Modified constraint set with hierarchical distance***

In a refinement of the original constraints, we utilize ranges to represent hierarchical distances, based upon the relationships shown in Figure 4.2. The choice of ranges, however (i.e., their extents, and degree of overlap, if any), is not a trivial one, and has potential impact upon the optimization. We therefore defined ten constraint sets, systematically varying their size and overlap (Table 4.1), and normalized each resulting hierarchy to make them comparable. The resulting “mean” hierarchy (Figure 4.4) shows that the results are fairly stable across constraint sets, with V1 consistently at the bottom and AITd consistently at the top. Interestingly, AITv maintains its position at  $\sim 0.6$  in the hierarchy, providing further support for the differentiation of it and its dorsal counterpart. With respect to constraint violations, STPp, a subdivision of STP, emerges as the worst offender. Young (Young, 1992) has proposed that STP may serve as a point of reconvergence of the dorsal and ventral visual streams. It may thus prove informative to empirically investigate the reasons

for such consistent violations by this and other regions, and how this affects the original assumptions relating laminar patterns to hierarchical relationships.

#### ***4.3.1.3. Alternative optimization criteria***

The method described above utilizes the sum of constraint deviations  $\sum \Delta_i$  as the sole criterion for the minimization performed by linear programming. This seemed to us the most logical choice; however, others are possible, including: (1.) the number of violations (i.e., instances where  $\Delta_i > 0$ ), and (2.) the maximal deviation  $\Delta_{max}$ . In a recent publication (Krumnack et al., 2010), we tested the consequences of adding these criteria to  $\sum \Delta_i$  to the optimization routine. While these factors were significantly lowered by their inclusion as minimization criteria, the resulting hierarchies are remarkably similar to that reported here, suggesting that the hierarchical structure is not particularly sensitive to their inclusion. Additionally, nine projections were identified as producing constraint violations across all constraint sets, for each of the three objective criteria (see Table 4.2). Such consistent violations have at least three interpretations: (1.) that the data for these connections, which produce their constraint violations, may be erroneous; (2.) that the conflict suggests a particularly region may consist of distinct subregions, with differing connectivity patterns; or (3.) that these consistent violators constitute exceptions to the anatomical assumptions underlying the optimization (namely, that laminar projection patterns correspond directly to hierarchical position).

#### ***4.3.2. SLN% as a Hierarchical Distance Constraint***

As explained in 1.4.4, the SLN% is a further refinement of the hierarchical distance rule, which stipulates that the *proportion* of cells labelled supragranularly corresponds to the hierarchical distance of the projection (Barone et al., 2000), thus yielding a real-valued constraint, rather than a range. We tested this possibility by applying the SLN% reported in (Barone et al., 2000), as constraints for our optimization. The resulting hierarchy, shown in Figure 4.7, yields unacceptably large deviations, particularly for the highest hierarchical region, THTF. This result does not support the initial assumption, and forces one to consider the problem in more detail. A critical observation is that the SLN%, being a proportion, should actually be treated as a *relative* constraint, rather than an absolute one, as we have treated it here. This point is demonstrated by the asymmetry (0.7832 versus 1.0) of the only reciprocal projection in the network, V1 to V4, and is illustrated aptly by a baseball analogy. Supposing a 12-year old little-league player and a major-league outfielder were to be asked to stand next to one another and throw a baseball at either 50% or 100% of their capacity. Barring some miracle, the boy will throw the ball a fraction of the distance that the major leaguer does, on each throw (Figure 4.8). Supposing the major-leaguer can throw twice as far as the boy, then in absolute terms, the boy's 100% will be equal to the man's 50%.

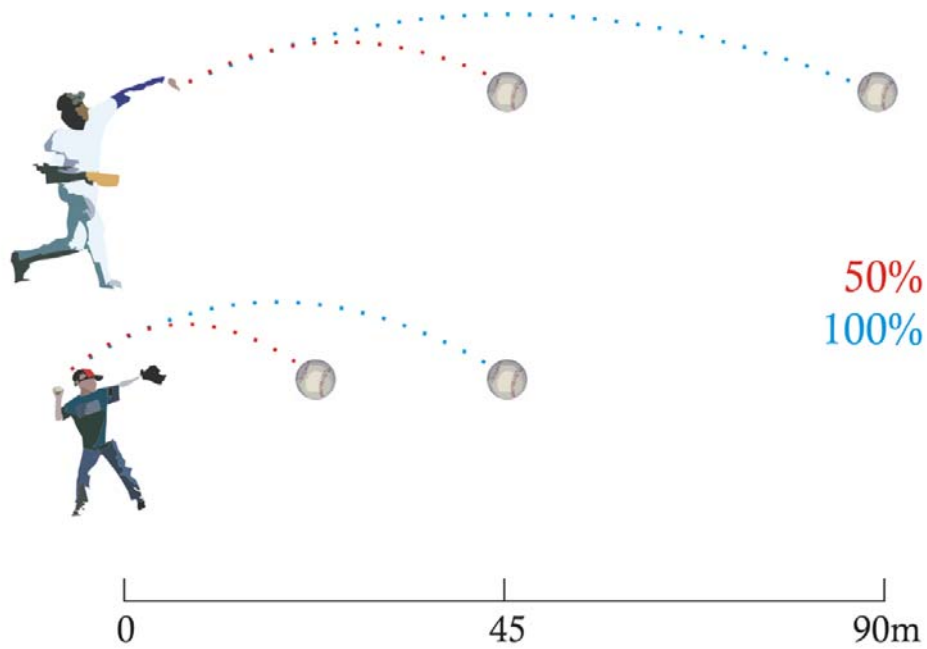


**Figure 4.8.** Absolute versus relative measures as a baseball analogy. Suppose a major league player throws twice as far (90m) than a little leaguer (45m). If the man throws at 50% of his capacity, and the boy at 100%, they will throw the same distance in absolute terms (45m).

This simple analogy may apply equally to SLN% values, which for a given region *A* should be considered as relative to the total range of *A*'s projections within the hierarchy. If, for instance, a second region *B* projects twice as far within the hierarchy, its SLN% values actually represent twice the hierarchical distance as for *A*. To derive absolute constraints from relative SLN% values requires a sufficient number of reciprocal connections, whose relative differences can be used to derive weights for each cortical region. Such a solution can be illustrated with a simple three-region example, shown in Figure 4.9.

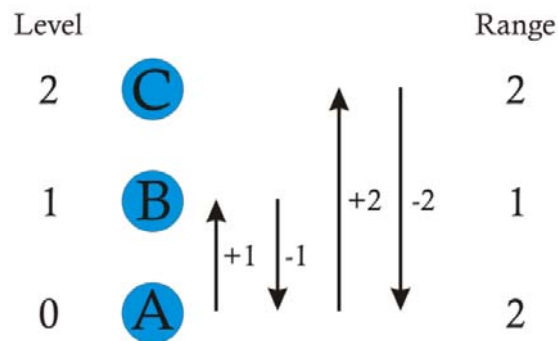


**Figure 4.9.** Toy example for calculating relative SLN% weights. A simple three-vertex graph representing a hierarchy with three levels, where edge weights represent absolute hierarchical distance. The range of a region's ascending and descending projections is shown at right.

Since SLN% is a proportional value, each vertex in this network should produce SLN% values relative to the range of its projections within the hierarchy (here we translate the SLN% such that 50%  $\rightarrow$  0.0):

$$A \rightarrow B: +1/2 = +0.5$$

$$B \rightarrow A: -1/1 = -1.0$$

$$A \rightarrow C: +2/2 = +1.0$$

$$C \rightarrow A: -2/2 = -1.0$$

From the set of reciprocal connections, we can derive a system of two equations, representing the relative weights  $w_i$  of each region  $i$ :

$$w_A = 2 \cdot w_B \quad (1)$$

$$w_A = w_C \quad (2)$$

Given that  $A$  and  $C$  are the largest values in this graph, we can assign them each a value of 1.0, from which we can obtain our set of weights:

$$w_A = 1.0$$

$$w_B = 0.5$$

$$w_C = 1.0$$

This is, of course, only a toy example. To apply this approach in practice would require that SLN% values were obtained from a sufficient number of reciprocal projections to fully determine weights for all cortical regions; such a data set does not yet exist, to my knowledge. In general, given  $n$  regions with unknown weights, we need  $n - 1$  reciprocal connections (at least one for each vertex in our graph) to ensure our system is not underdetermined (since we assign a value of 1.0 to the region with the largest projection range). In practice, however, there can be as many as  $n \cdot (n - 1)/2$  reciprocal connections, resulting in an overdetermined system. This suggests an optimization approach would best be applied to minimizing error in the set of solutions.

### 4.3.3. General Considerations

One motivation for establishing a functional cortical hierarchy from purely anatomical information may be the potential of such a model for generating falsifiable hypotheses about the way the cortex processes information. Such a model ought to predict, for instance, such functional parameters as the latency from stimulus to activation onset in a given region, or the relative degree of stimulus selectivity observed in a neuronal recording. One of the most prominent of our results is the consistent displacement of regions AITd and AITv across out hierarchies, despite their being placed on the same level in the original FVE91 hierarchy. These two regions have differential projection patterns with a number of regions, including hippocampus, superior temporal sulcus (STS) (Saleem et al., 2000), and perirhinal and entorhinal cortex (Saleem and Tanaka, 1996). Tamura and Tanaka (2001) investigated the response properties of areas TEav and TEad, which have a close correspondence with AITv and AITd, respectively. While they report no significant difference in *minimal* stimulus onset latencies, they report a significantly longer latency in TEav than in TEad for *significant* excitatory responses ( $133.2 \pm 68.2$ ms versus  $115.9 \pm 52.0$ ms); they also found that TEav responded more effectively to specific objects than TEad. These functional differences do

suggest some difference between these two regions. A more definitive approach to this question may be possible using higher resolution field recordings from *in vivo* multi-electrode arrays (MEAs) (Guo et al., 2008; Charvet et al., 2010).

A second motivation for cortical hierarchies is the possible identification of regions which appear to violate the hierarchical organization scheme, which highlight them as regions of interest for anatomical investigations. As a supplement to (Hilgetag et al., 1996), the authors make a number of predictions about anatomical parcellations, based upon their optimization results. One prediction was that region FST, which had a high variance and a bimodal distribution, may actually consist of two subregions. While we observe that FST is associated with a high number of violations, it does not appear anomalous within our optimal hierarchies, nor does it have especially high variance. They further suggest that four regional subdivisions ought to be considered distinct areas, since their interregional distances are variable. We find this to be true in all cases but one (PITv and PITd), which we find to have a high interregional distance correlation, and a small mean distance and variance. Our results are consistent with two other predictions, that V4t and MT are closely linked, as are CITd and CITv (see Figure 4.6). Finally, V3 and VP, a pair which is mentioned by Hilgetag et al. as one of particular interest for their potential analogy to dorsal and ventral hemi-regions, are also always placed at the same level in our hierarchies. (Felleman et al., 1997) demonstrate that the subdivision of V3 and VP is justified by a number of observed differences in intracortical projection patterns. Our present results, as well as independent comparisons using multivariate analyses of neurotransmitter receptor distributions (Kötter et al., 2001), suggest that, despite these differences, these two regions may share an identical hierarchical position.

### ***4.3.4. Conclusions***

A novel methodology is presented for obtaining an optimal hierarchy from anatomical observations of laminar source and termination patterns of interregional projections, building upon the research findings of Felleman and Van Essen (1991) and others. It is noteworthy that the functional significance of such a hierarchy is unclear; indeed, its relevance has been challenged by (Hegd e and Felleman, 2007), who point to the degree of complexity in cortical dynamics (which includes parallel processing streams, oscillatory modulation, and multisensory inputs) observed by modern methods, which cannot be adequately captured by the simplicity of the anatomical hierarchy concept. The authors propose an alternative Bayesian inference framework, incorporating these functional properties, as an alternative to the hierarchical model. Such an approach is certainly attractive, although it does not preclude the idea of utilizing a hierarchical representation as an anatomical prior; informational hierarchies do clearly exist, at least within subnetworks of the brain. Indeed, this suggests the necessity of an automated, observer independent computational method for generating hierarchies from the whole-brain networks that would presumably be required to represent cortical processing in this way. This idea, combined with a refined distance measure in the form of SLN% measurements, suggests a clear way forward for the investigation of cortical organization.

## **5. Structural Integrity of Corticocortical Connections**

### **5.1. Methods**

One important application of structural MR data is the estimation of structural integrity in individual subjects, particularly those with WML. Such an integrity measure can be useful for both clinical diagnoses of neurological symptoms, as well as measures of effective connectivity, or the testing of forward models of brain activation. With the RUN-DMC data set, it is possible to integrate the structural connectivity information contained in both the FLAIR-based WML delineations, DWI-based diffusion data, and cortical surface parcellations. Accordingly, my colleagues and I have devised a measure of *connection integrity*, which can describe the extent to which any connection between cortical regions A and B has been disrupted by a WML. The process of obtaining such measures from the RUN-DMC data set is described below.

#### ***5.1.1. Image Preprocessing***

Due to its use of high gradient fields, DWI data is particularly subject to a number of artifacts. Eddy currents, for instance, are produced by turning the Z gradient field off or on, which induces a current in the metal parts of the imager itself. This can result in significant image artifacts, which must be corrected after acquisition. Head motion is likewise a common problem. Diffusion data obtained from the RUN-DMC project were pre-processed using the Donders Institute Diffusion Imaging package (DIDI), a Matlab tool developed at the Donders Center for Cognitive Neuroimaging (Radboud University Nijmegen; [www.ru.nl/neuroimaging/diffusion](http://www.ru.nl/neuroimaging/diffusion)), which corrects for cardiac and motion artifacts using the “Patching the Artifacts from Cardiac and Head motion” (PATCH) algorithm. This is done by first estimating the diffusion tensor model (Section 1.5.2.2), which can be used to correct simultaneously for both eddy current and subject motion artifacts, using an algorithm which minimizes the residual error in the model (Andersson and Skare, 2002).

#### ***5.1.2. Surface-to-Volume Projection of Cortical Parcellation***

To obtain an appropriate volumetric parcellation, there are at least two possibilities: (1.) use a volume-based atlas such as the Automated Anatomical Labelling atlas (AAL) (Tzourio-Mazoyer et al., 2002), or probabilistic atlases (Amunts and Zilles, 2001; Eickhoff et al., 2005b; Shattuck et al., 2008), which are already aligned to the same stereotaxic space as the RUN-DMC images; or (2.) use a surface-based parcellation, such as is represented on the PALS surface (Van Essen, 2005), and project from this surface onto the volume. The former option is simplest, since these atlases are already aligned and can be used directly. However, this suffers from at least two drawbacks: (1.) in both cases, a sulcal boundary issue exists, such that individual variations in sulcal patterns can result in non-contiguous ROIs (i.e., parcellations which “jump” across sulci, and thus do not respect neighbourhood relationships); and (2.) in the case of the histology-based probabilistic atlas, the cortical representation is not yet complete.

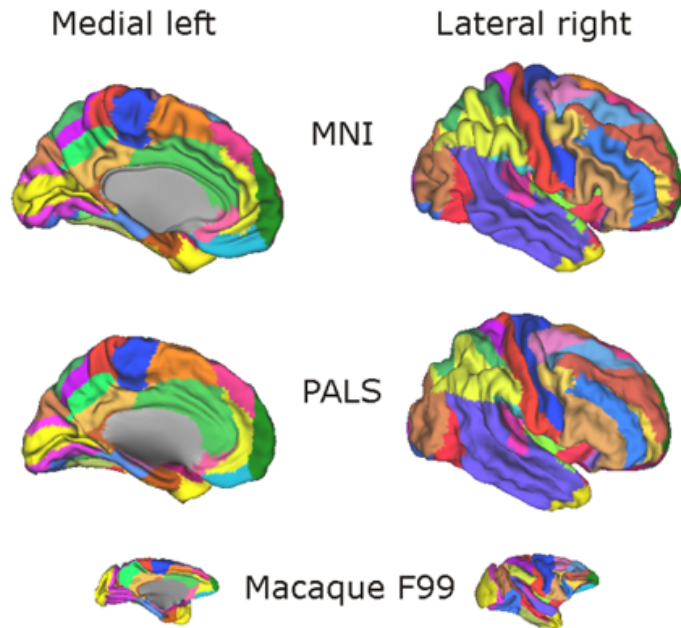


**Figure 5.1.** The regional map (RM) painted on three surface templates. RM was manually delineated on the F99UA1 surface, and subsequently deformed, firstly to the PALS-B12 surface, and secondly to the MNI (Civet) template surface. Figure courtesy Gleb Bezgin.

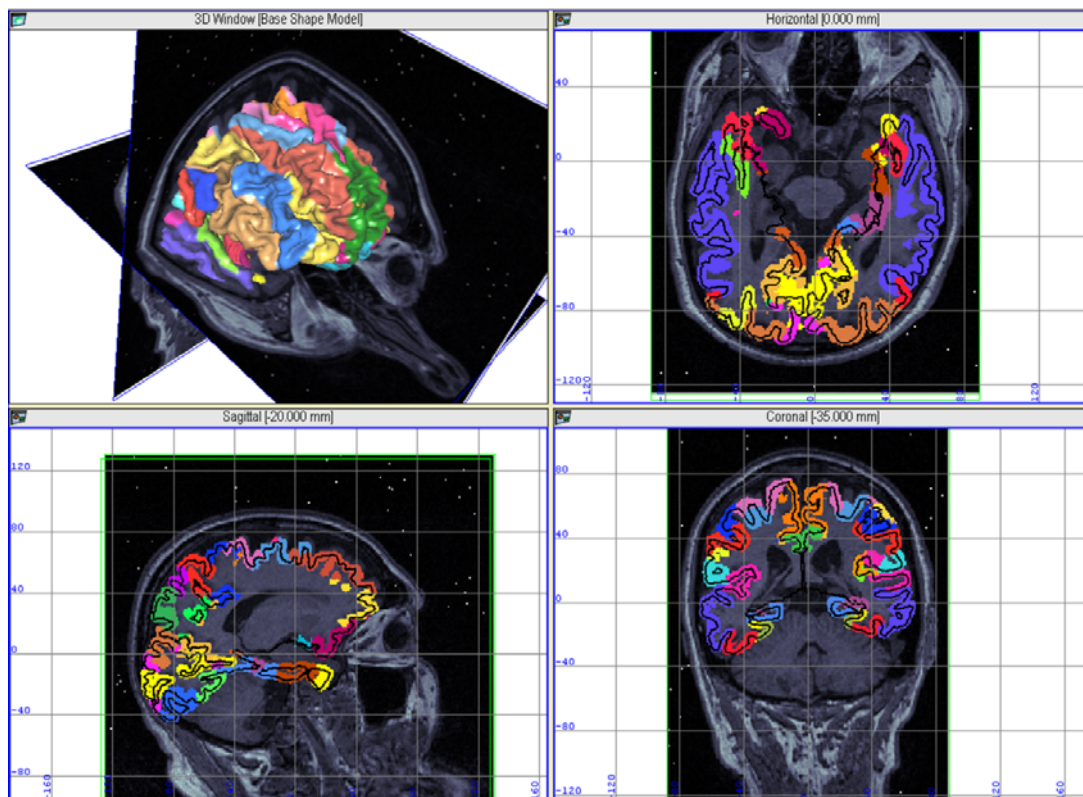


**Figure 5.2.** Projection of the surface-based RM parcellation into native volume space, shown for a single subject overlaid on a structural T1-weighted image.

For these reasons, we chose to use the surface-based “regional map” (RM) parcellation of (Kötter and Wanke, 2005). This whole-cortex parcellation consists of 38 regions per hemisphere, and was devised to accommodate, on a coarse scale, the degree of known or presumed interspecies correspondence between primate cortices (i.e., with respect to microstructure, function, and topography). The names of the various RM regions, therefore, correspond to “general functional (e.g., V1, M1, FEF), structural (e.g., amyg, HC) or topographic (e.g., PFCdl, PCip, TCpol) area names that are widely recognized and convenient to use”. The RM was manually delineated ((Bezgin et al., 2008); and personal correspondence) onto a template macaque cortical surface representation (F99-UA1), using Caret software (Van Essen, 2005), subsequently deformed to the PALS-B12 human atlas, and finally to the Civet template surface, using two landmark-based deformations. The correspondence between these three surface parcellation is shown in Figure 5.1.

Given the vertex-wise correspondence between individual cortical surfaces in the RUN-DMC cohort obtained through the Civet pipeline, once deformed to the Civet template surface, the RM parcellation can be projected from individual surfaces to a set of voxels. This was done in native space, using the Caret “surface-to-volume” command, which projects vertex-wise paint values from a surface mesh to voxels along vertex normal vectors. Values were projected 1.5 mm to either side of the middle cortical surface (generally representing layer 4), resulting in the volumetric parcellation shown in Figure 5.2.

### ***5.1.3. White Matter / Grey Matter Interface***

Since we are interested in the connection along WM from brain region A to brain region B, it is desirable to start our tractography at the interface between GM and WM. This involves two steps: (1.) tissue classification using the FMRIB’s Automated Segmentation Tool (FAST) from the FSL package (Zhang et al., 2001); and (2.) expansion of the WM tissue compartment. The resulting overlap of expanded WM and GM compartments was assigned as the GM/WM interface, which served as a mask for the RM seed regions.

### ***5.1.4. Tractography***

Probabilistic tractography was performed by FSL’s Diffusion Toolbox (FDT), using the Bayesian Estimation of Diffusion Parameters Obtained using Sampling Techniques with Crossing Fibers (BEDPOSTX) technique (Behrens et al., 2003). This involves two main steps: (1.) Estimation of diffusion model parameters; and (2.) probabilistic tractography:

#### **i. Estimation of diffusion model parameters**

Parameters for the diffusion model can be estimated from DWI data using the Bayesian prior probability density, yielding orientation probability distributions, or ODFs. In practice this involves a numerical solution called Markov Chain Monte Carlo (MCMC) sampling. This requires ~24 hours of processing on a single processor, but is parallelizable and thus runnable on a computing cluster.

#### **ii. Probabilistic tractography**

A single tractography sample involves starting a path at the center of a seed voxel, and propagating it through subsequent voxels at discrete distance steps, sampling from the ODF at each step to determine the next direction. This is repeated until a stopping criterion is met, such as a low probability, a high

direction angle, or a labelled voxel (indicating, for instance, that a target region has been reached). A fixed number of such runs is made, and this sample represents a probabilistic distribution of tract trajectories which originate in the seed region.

Probabilistic tractography was performed using 2000 samples on each pair of regions in the Regional Map, for a total of  $38 \cdot 2 = 76$  regions;  $76 \cdot (76 - 1) = 5700$  runs;  $5700 \cdot 2000 = 1.14 \cdot 10^8$  samples. This number was actually substantially higher, since (1.) each pairwise run involved specifying each voxel in the WM/GM-masked RM source regions as a seed voxel, multiplying the number of runs by the number of voxels in the region, and (2.) this was done twice for each subject, such that in the second run a WML “waypoint” mask was specified, which was used to estimate the number of single tracks which passed through a WML mask. Thus, after all processing was performed, the result was a voxel-wise count of tracks starting in brain region  $i$  and terminating in brain region  $j$ , and a second count for the number of these that went through a WML.

### 5.1.5. Structural Integrity Estimation

To obtain a score of structural integrity for each pair of regions  $\{i, j\}, i, j \in M, i \neq j$ , where  $M$  represents the set of all regions in RM, we can do the following. First, we obtain a total connectivity score  $c_{total}$ , which is the sum of all tracks from  $i$  to  $j$ , and all tracks from  $j$  to  $i$ :

$$c_{total}(i, j) = \sum_{k_i}^{N_i} t_{ij} + \sum_{k_j}^{N_j} t_{ji}$$

where  $N_i$  is the total number of voxels in region  $i$ , and  $t_{ij}$  is the total number of tracks from  $i$  to  $j$ . Next, we obtain the sum  $c_{wml}$  for the number of tracks which pass through a WML mask:

$$c_{wml}(i, j) = \sum_{k_i}^{N_i} w_{ij} + \sum_{k_j}^{N_j} w_{ji}$$

where  $w_{ij}$  is the total number of tracks from  $i$  to  $j$  which pass through a WML waypoint. The integrity  $I$  of the connection from  $i$  to  $j$  can then be estimated as simple proportion:

$$I_{ij} = 1 - \frac{c_{wml}(i, j)}{c_{total}(i, j)}$$

### 5.1.6. Mean Symmetry

Mean symmetry is graph measure which indicates the proportion of a graph’s projections which are reciprocal. In an undirected graph, such as that produced by DWI tractography, this value will necessarily be 1.0. However, a real cortical network is directed, and thus may have a high degree of asymmetry. Thus, the usefulness of a connectivity matrix derived from a DWI method, as presented above, may result in a graph which fails to represent this asymmetry, weakening any conclusions which may be drawn from it. Since directional data are available from macaque tract tracing studies, compiled in the CoCoMac database, it is possible to derive a measure of mean symmetry for the RM parcellation used in this study.

To do this, we define a graph  $G$ , representing the Regional Map, with 38 vertices, representing the 38 regions found in one hemisphere. Making the assumption that both

hemispheres are identically connected, a mean measure derived from one hemisphere can be used to represent both. If we fully connect  $G$ , we can weight its edges such that  $c_{ij} = 0$  indicates no projection between vertex  $i$  and vertex  $j$  ( $i, j \in G$ ), and  $c_{ij} = 1$  indicates the existence of a connection. Given this representation, the number of reciprocal connections  $c_{reciprocal}$  can be calculated as:

$$c_{reciprocal}(i) = \sum_k^{n_i} c_{ik} \cdot c_{ki}$$

where  $n_i$  is the number of  $i$ 's neighbours. The sum of all connections  $c_{total}$  is:

$$c_{total}(i) = \sum_k^{n_i} c_{ik} + \sum_k^{n_i} c_{ki}$$

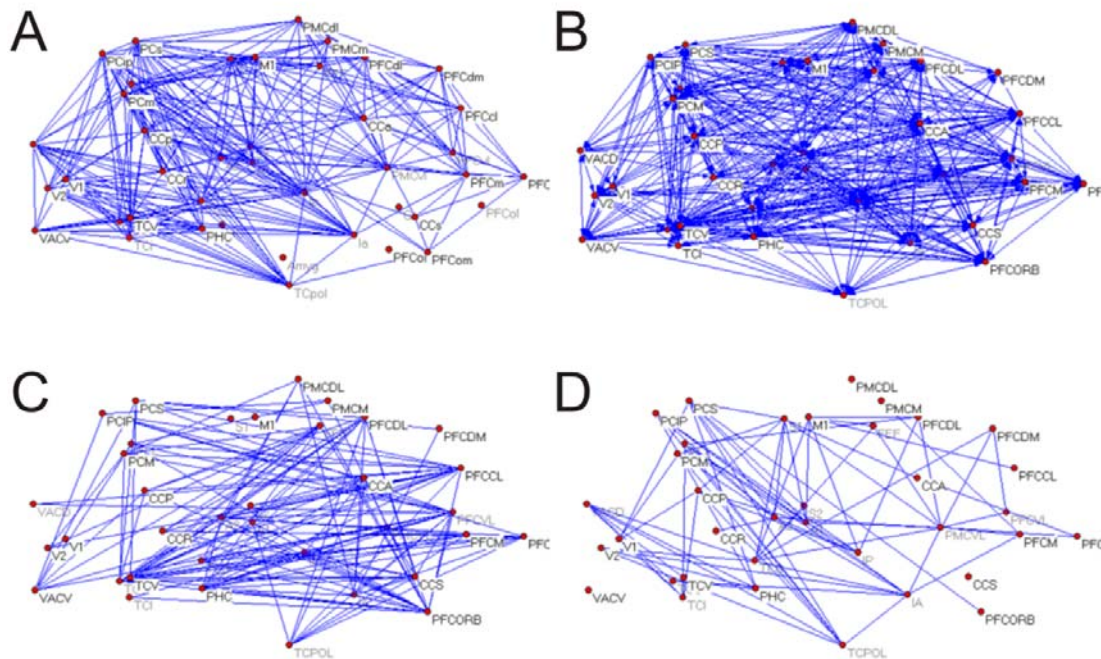
Finally, the mean symmetry  $S$  is:

$$S(G) = \frac{2 \cdot \sum_i^n c_{reciprocal}(i)}{\sum_i^n c_{total}(i)}$$

## 5.2. Results

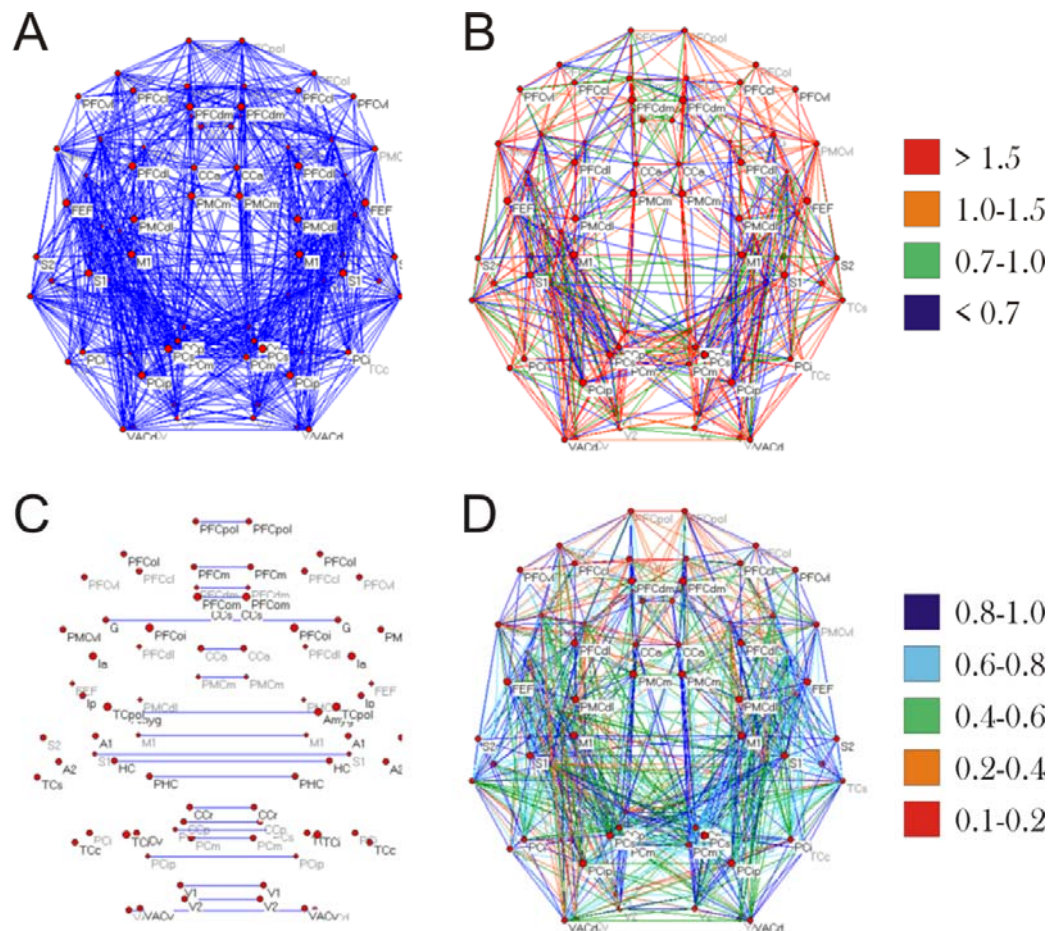
### 5.2.1. Connectivity

Figure 5.3 shows preliminary results of our DWI tractography method, derived from six subjects, and plotted using real geometric centroids derived from the Civet template surface. A quick visual comparison of Figure 5.3A, which shows the DWI-derived connectivity, and Figure 5.3B, which is the connectivity predicted by the CoCoMac database, reveals that the former is substantially sparser. Figure 5.3C shows the edges which are known to exist, in CoCoMac, and are not found by the DWI tractography; there are 131 of these, for the right hemisphere. Many of these are long-distance projections, although a number of longer-distance connections are found by the tractography. Conversely, Figure 5.3D shows edges representing projections which are known *not* to exist, according to CoCoMac.



**Figure 5.3.** Preliminary results for DWI tractography. Graphs depict the right hemisphere only, and are shown from the right lateral aspect, with positions determined from the centroids of the RM ROIs. **A:** Undirected connectivity derived from DWI tractography, averaged over six subjects. **B:** Directed connectivity derived from the CoCoMac database. **C:** Edges which are known to exist in the CoCoMac database, but are not found with DWI tractography. **D:** Edges which are found with DWI tractography, but are known not to exist in the CoCoMac database.

The same DWI-based connectivity is shown in Figure 5.4A, from the superior aspect. In Figure 5.4C, only projections to a region's contralateral counterpart are shown. We find that only 20 of 82 interhemispheric pairs are connected with the DWI tractography. Long-distance connections are particularly absent, although as with intrahemispheric connectivity, distance does not appear to strictly predict connection probability.



**Figure 5.4.** Superior view of DWI-derived connectivity, showing **A:** all projections. **B:** the same, with edges coloured by the log of the average number of tracks per voxel (as per colour scale as shown). **C:** only contralateral projections to homologous regions. **D:** connections coloured by the average integrity score (as per colour scale as shown).

The output of the probabilistic tractography routine specifies the number of tracks originating in a seed voxel and terminating in a target region. Figure 5.5 shows the frequency histogram for connections per voxel, for all connections with at least one connection per voxel. ~700 of 1042, or 67% of voxels had less than 20 connections out of a sample of 2000; i.e., less than 1% of tracks originating in that voxel reached the target area. The remaining 33% of voxels have somewhat higher connection probabilities, but none greater than 0.45. Figure 5.4B shows the distribution of these values in the network (values are log-transformed, due to the large skew as seen in the histogram). Edges with low probabilities tend to occur within the core of the network, while edges with higher ones occur more superficially. Additionally, there is a significant negative correlation between interregional distance and connection probability ( $r = -0.4129$ ,  $p < 0.001$ ).

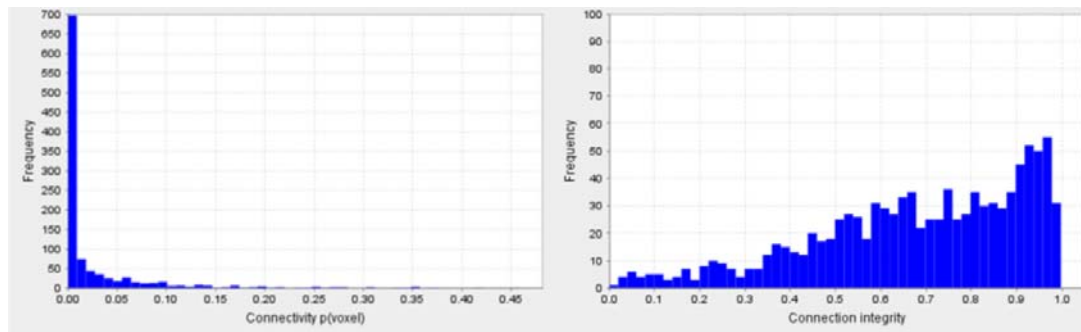


**Figure 5.5.** Histograms of DWI-derived data, showing the distribution of voxel-wise connection probabilities (left) and the distribution of connection integrity (right) across the DWI network.

### 5.2.2. Integrity Measures

Figure 5.4D shows the connection integrity measures, derived by our method. This value indicates the degree to which a projection is occluded by a WML. Frontal connections appear to have generally lower integrity values (orange and red) than the rest of the network. There is also an apparent bias towards the left hemisphere. Figure 5.5, right, shows the distribution of integrity values across the entire network, indicating a right-skewed distribution.

### 5.2.3. Mean Symmetry

The mean symmetry  $S$  was introduced in Section 5.1.6 to obtain an indication, based upon connectivity information from the CoCoMac database, of the degree to which the connectivity of the RM may be asymmetrical, and thus differ from the non-directed graph representation produced by our DWI approach. The mean symmetry of RM, based upon a 38-vertex graph representation of a single hemisphere, is 0.7766. This indicates that ~23% of the cortical connections represented in this graph are asymmetrical, based upon existing knowledge (it is notable that ~14% of interregional relationships are unknown).

## 5.3. Discussion

The results reported here for the DWI connection integrity scores are very preliminary, being derived from only six subjects, of the total 485 for whom data are available. Nonetheless, it is possible to derive trends from these early results, as well as identify methodological issues which require further consideration before the data set can be fully processed. I discuss these issues in the following sections.

### 5.3.1. Connectivity

The connectivity derived from our DWI tractography method is considerably sparser than that predicted by the CoCoMac database, which is based upon macaque tract tracing literature. As Figure 5.3 illustrates, there are 131 connections per hemisphere that are known to exist, on the basis of CoCoMac evidence, yet are not discovered by the tractography. Moreover, only 24% of regions were found to have connections with their contralateral counterparts. These results are problematic, as they limit the network with which we can work, and also suggest a bias that calls into question the validity of our

integrity measures. These issues require further consideration, and a number of facts may help establish the reason for this discrepancy:

**i. Edge length**

Visually, many of the missing edges appear to be more long-distance ones (see Figure 5.3C), and there was indeed a substantial negative correlation between interregional distance and connection probability, for edges that did exist, although this explained only part of the variance. Distance also appears to be a factor for contralateral projections (see Figure 5.4C).

**ii. Edge location**

Figure 5.4B reveals an interesting pattern, in which internal edges appear to have more frequently small connection probabilities than external ones. This may also be a factor of distance (longer connections may tend to be more internal), but it highlights the possibility that specific spatial configurations of projection trajectories may be less probable (in terms of tractography) than others.

This connectivity issue has been well reported in tractography literature, and has been attributed to a number of factors, including the presence of multiple fiber directions within a voxel, although the FDT routine used for tractography includes many optimizations meant to address many of these factors (Behrens et al., 2007). The problem of distance, however, is inherent in the tractography approach. The term “connection probability”, which I have already used, actually refers to the probability that a track starting at a given seed voxel will terminate in a certain set of labelled voxels elsewhere (the region of interest). This is necessarily a factor of distance – among other factors such as the degree of dispersion (Lazar and Alexander, 2005) – because with every new voxel there is a chance that the track will deviate or terminate. This results in low probabilities even for well-known projections (Sherbondy et al., 2009). Possible ways to address this issue will be discussed below.

### ***5.3.2. Integrity Scores***

Despite the incompleteness of the DWI-derived connectivity matrix, the preliminary average connection integrity results (Figure 5.4D) are somewhat promising. The most compromised edges appear to be between frontal areas and edges which project close to the midline (while these edges connect centroids and are not geometrically equivalent to WM tracts, they can be considered to approximate their trajectories to a very rough extent). There also appears to be more compromised connections for the left hemisphere than for the right. While it must be reiterated that these results are derived from only six subjects, the overall pattern of integrity loss is consistent with the pattern of GM degeneration described in Section 2.2. The distribution of integrity scores across the entire network is equally interesting (Figure 5.5, left), exhibiting a right-skew which indicates that the bulk of connections have over 50% integrity; although the overall numbers of compromised fibers is higher than might be expected. It will be an important step to investigate the ways in which this distribution interacts with age, as well as additional factors such as total WML load, cortical thickness, cognitive performance, region of interest, etc.

### ***5.3.3. Mean Symmetry***

The finding that ~23% of connections between regions in the RM are asymmetrical is also cause for concern, considering that lack of directional information in DWI data preclude any knowledge of asymmetry. This suggests that any attempt to utilize the connectivity information derived from the method we present here should also be informed by tract tracing data, which can be used as a constraint on the construction of graph edges. This would address another problem, namely that the tractography algorithm identifies connections between regions which are known not to exist (Figure 5.3D).

### ***5.3.4. General Considerations***

The results discussed here suggest that our novel connection integrity method has the potential to produce very interesting information about whole-brain structural connectivity, which can have many benefits for further investigation into cortical circuitry, normal and pathological aging, and brain function in general. On the other hand, the inconsistency of our DWI-derived connectivity matrix with that constructed from tract tracing data indicates that this part of the method will require some improvement. The size of the tractography sample is an obvious starting point; here we have utilized 2000 samples per voxel, due to computational concerns, whereas a number closer to 5000 is more commonly used. Another, more involved potential solution is to incorporate as *a priori* evidence, the existence or absence of particular interregional connections, based upon tract tracing literature. This would shift the focus of our method away from the *discovery* of a connection towards a more accurate *description* of its trajectory, which is in any case our main concern in the production of an integrity estimate. A method for determining the most probable path between two ROIs has already been proposed by (Sherbondy et al., 2009), who sample from a probability distribution of possible connection paths, and determine the most probable path using the diffusion data. An alternative solution might be to inform the tractography algorithm based upon CoCoMac evidence. In this case, for a connection which is presumed to exist, the position of the target region can be used as a Bayesian prior which helps “guide” the track towards its target.

## 6. General Discussion

### 6.1. The Blind Men and the Elephant

*I.*

*It was six men of Indostan  
To learning much inclined,  
Who went to see the Elephant  
(Though all of them were blind),  
That each by observation  
Might satisfy his mind*

*MORAL.*

*So oft in theologic wars,  
The disputants, I ween,  
Rail on in utter ignorance  
Of what each other mean,  
And prate about an Elephant  
Not one of them has seen!*

– John Godfrey Saxes. *The Blind Men and the Elephant. A Hindoo Fable.*

The fable of the blind men and the elephant is a favourite presentation device of my colleague Ingo Bojak which, in both our opinions, is very aptly applied to the field of neuroscience. The poem excerpt above is derived from an Indian fable in which six blind men attempt to describe an elephant by touching very different parts of it, resulting in a predictable dispute not dissimilar to some of the disputes which have arisen over the evolution of neuroscientific research. The moral, of course, is that through an integration of disparate forms of observation we can arrive at a more complete understanding of the phenomenon of interest than would be possible if we were to exclude ourselves to narrow fields of view. There are few disciplines where this applies more strongly than for neuroscience, as the present dissertation attempts to demonstrate. None of the research methods described herein could have been possible without the integration of the seemingly disparate fields of cellular biology, anatomy, physiology, neurology, mathematics, physics, computer science, informatics, and so on. The functional interpretations, moreover, are greatly enriched by considerations deriving from the field of psychology, which is my own background.

In the remainder of this discussion I will attempt to draw parallels between the different lines of research I have pursued in my Ph.D. tenureship, and present ways in which these findings can be integrated in future research. The elephant I wish to comprehend will require an integration of structural information with a graph theoretical framework, which can be analyzed both statically and dynamically. The ultimate goal would be to combine these results with functional and behavioural data and forward modelling approaches, in an attempt to challenge some of the prevailing theories of cognition and aging, such as the scaffolding theory of (Park and Reuter-Lorenz, 2009), which make certain falsifiable predictions about effective connectivity.

### 6.2. The Brain as a Computer

John Von Neumann was a Hungarian-born polymath who, among many other remarkable achievements, invented the Von Neumann architecture, which remains the foundational basis of modern computer engineering. In his later years, Von Neumann published a book called *The Computer and the Brain* (Von Neumann, 1958), in which he speculated about the connections between the two, drawing parallels between their control structures and

apparent digital processing. Being dated, a number of these parallels turn out to be either false or grossly oversimplified, but the comparison is a fine one, and worth further consideration. I have been scolded in the past for referring to the human brain as a computer, given the vast differences between the Von Neumann architecture which resides in our notebooks and desktops, and which we commonly refer to as a computer, and the bogglingly complex architecture and communicative mechanisms of the organ that resides in our skull casings. However, in the more abstract Turing conceptualization of the computer, there is no doubt that our brains qualify.

The progression of modern computer technology is further testament to this: both in the movement towards parallelized hardware and network configurations, and the advance of computer programming into object-oriented designs. The latter is perhaps most striking with respect to its resemblance of brain organizations, in that it is modularized into distinct objects, which specify the nature of the input they expect and the output they produce, in much the same way as (one might speculate) brain regions do. Moreover, like brains, this organization of software emerged through a sort of evolutionary process, building upon the trial and error of programmers and software engineers, in response to the ever-expanding demands of human users. Today's software projects have assumed an organization that bears an uncanny resemblance to that of the brain: the use of "tiered", or hierarchical structures, in which low-level code takes care of tedious tasks such as parsing and assembling instructions and data, and passes on its output to increasingly specialized modules that, in the end, execute banking orders, serve up web pages, produce thesis dissertations, or process MRI data sets.

This comparison between computers and brains is, in my opinion, more than a simple analogy. Through an understanding of the same concepts that permit the engineering of complex computational structures, we can gain a better comprehension of the ways in which the brain must process information to accomplish the goals that its genome has set for it. The methods I describe here are a start: graph theory and neuroanatomy are ways to examine the architecture of the system, which is a required basis for advancing further, more functional inquiries, just as a knowledge of computer architecture, software languages, protocols, and engineering principles is a prerequisite for understanding and producing new forms of software. The study of various states of brain degradation, moreover, is as informative to its function as the act of "debugging" is to software design: it is sometimes difficult to understand why something functions until you can understand why it *doesn't* function. In the end, as I will expand upon in the final section, I would like to see these first steps lead into new steps, in which the functional and effective connectivity of the RUN-DMC data set, and others like it, can be investigated based upon statistical and simulation techniques such as dynamic causal modelling, or more biophysically fiducial efforts such as mean-field or single-cell models. This integration of theoretical and empirical methods are possibly the most promising conduit for understanding how our organic computers function.

### 6.3. Lessons from the Aging Brain

Based upon behavioural observations of a cohort of over 600 adults with ages ranging from 25 to 103, (Baltes and Lindenberger, 1997) report a lifetime-wide association between early sensory processing and higher intellectual function. The dedifferentiation hypothesis they have proposed suggests a relationship between the efficiency with which early specialized neural circuitry can handle perceptual or multisensory challenges, and the ability of higher-

level cognitive functions to respond to task involving these challenges. Such dedifferentiation has also been linked to the aging process; as low-level neural circuitry degrades, a higher demand is placed upon executive regions, and in particular the PFC, to compensate. (Park and Reuter-Lorenz, 2009) refer to this sort of compensation as *neurocognitive scaffolding*. Here I have reported an age-related thinning of parts of primary visual and auditory cortices, which agrees with results from (Salat et al., 2004), and would appear to correspond to the dedifferentiation hypothesis. Such a connection, however, would require more targeted investigation, the nature of which I will speculate upon here.

While a simple task-related functional imaging design would be ideal to investigate the relationship between structure and function, such data are not available in the RUN-DMC study. Functional data are available, however, in the form of resting-state fMRI, which has been used to identify a commonly-activated “default mode” network in the brain (reviewed in (Raichle and Snyder, 2007)). Default mode activity is associated with a behaviourally “resting” state, and is suppressed when the brain is challenged by a cognitive task, showing an inverse relationship with prefrontal activity (Greicius et al., 2003). Moreover, this suppression is reportedly reduced in older adults, and the degree of this reduction is correlated with performance on some cognitive tasks (Grady et al., 2006; Persson et al., 2007). It would be possible, therefore, to examine the default mode activity in the RUN-DMC cohort. While the resting-state paradigm is not associated with task demands, the functional results can be used to investigate functional connectivity within and between functional networks including the default mode network. This functional connectivity can, moreover, be combined with the structural results obtained from DWI data, to investigate effective connectivity using the methods described in Section 1.4.3. This will be formulated more specifically below.

In their review of neurocognitive scaffolding, (Park and Reuter-Lorenz, 2009) propose a number of questions for future research. A number of these open questions can potentially be addressed with the RUN-DMC data set:

- i. What is the relationship between structural degradation and functional activation, and does this support the notion of scaffolding?
- ii. Can the presence of early-onset scaffolding predict the development of cognitive impairments or dementias? This prognostic question can be best answered with longitudinal data.
- iii. Can experience (life activity, cognitive engagement, education, etc.) help prevent the development of cognitive impairment and brain degradation?
- iv. Are certain patterns of functional activation support cognitive scaffolding more than others? Phrased differently, can the specific patterns of GM or WM degradation predict the degree of compensation?

## 6.4. Large, Longitudinal, Human Data Sets

As has been stated and reiterated throughout this dissertation, the RUN-DMC is a large cohort, with a wide variety of data modalities, including imaging data obtained at the same site, using the same scanner, and identical acquisition protocols. This gives it a distinct advantage over other attempts to collect epidemiological data, which typically combine data from multiple sites, incurring a number of difficult comparison issues. Other large human

## General Discussion

data sets have arisen, due largely to the increased availability of dedicated research scanners, and an enhanced interest in such large-scale designs which, while they cannot typically address specific questions about brain function, have on the other hand superior statistical power to detect population-wide effects. Many of these projects, moreover, are longitudinal in nature, providing not on a cross-sectional analysis of a population, but important insights into how the brain evolves over time, both through normal aging and over the course of pathological conditions. In addition to their obvious clinical advantages, such data sets are hugely promising for advancing our fundamental understanding of how the brain functions both as a computer and as a genetically constrained organism.

## 6.5. Future Considerations

### *6.5.1. Informing Models of Effective Connectivity*

As introduced in Section 1.4.3, an analysis of effective connectivity requires two models: (1.) a model specifying the architecture and structural connectivity of the system, and (2.) a mathematical model specifying its dynamic behaviour. In the case of dynamic causal modelling (DCM), this includes both a biophysical model of the brain, and a statistical framework with which to fit parameters and compare models. The RUN-DMC data set, combined with the CoCoMac database and the results presented in this dissertation, provide the necessary basis for analysis of effective connectivity, which I will outline here. It is important to note that a DCM will necessarily be limited to a small subset of regions. Therefore, such an approach should be targeted at specific questions about connectivity, such as those which arise from the neurocognitive scaffolding hypothesis.

A structurally connected network can be derived in a variety of ways. The simplest approach, perhaps, is to use the connectivity specified by the macaque tract tracing literature compiled in the CoCoMac database, with respect to the Regional Map (RM) parcellation introduced in 5.1.2. In its current state, CoCoMac specifies connectivity for ~86% of the possible interregional projections. A second approach may be to utilize the DWI information available for each subject to obtain a connectivity matrix. However, this approach has at least two difficulties: (1.) the problem of detecting long-range or highly-bending projections, as discussed in Section 5.3.1.; and (2.) the lack of direction information; given that the mean symmetry of RM, according to CoCoMac, is only ~78%, this suggests a nontrivial ambiguity with respect to the directionality of any connectivity matrix derived solely from DWI data. A better solution would be to combine the information from both modalities, either by assigning directionality directly from CoCoMac or, preferably, utilizing CoCoMac information as a prior constraint on the tractography algorithm itself.

The complexity of the network model is dependent upon the nature of the question being addressed through this analysis. Therefore, it is useful to specify a specific question at this point, even for the purpose of a speculative example. One question of interest arises from the work of Daselaar and colleagues (Daselaar et al., 2006), who report a double dissociation in older adults between activity in the left hippocampus and both a left parietotemporal region and rhinal cortex, and suggest that this may be compensated by a corresponding increase in associativity between left rhinal and bilateral frontal cortex. While this study used an task-related design, it might be interesting to investigate this dissociation using our resting-state BOLD activity; more precisely, we are interested in whether our anatomical observations can predict a shift in *effective* connectivity, corresponding to this functional change. Since information on hippocampal volume is already available in the RUN-DMC cohort (van Norden et al., 2008), we can construct a DCM which integrates this knowledge with cortical thickness information, and the structural connectivity evidence provided by our WM integrity scores. Our model can thus be comprised of eight regions, four for each hemisphere (see Figure 6.1): (1.) hippocampus, (2.) parietotemporal cortex, (3.) rhinal cortex, and (4.) frontal cortex.

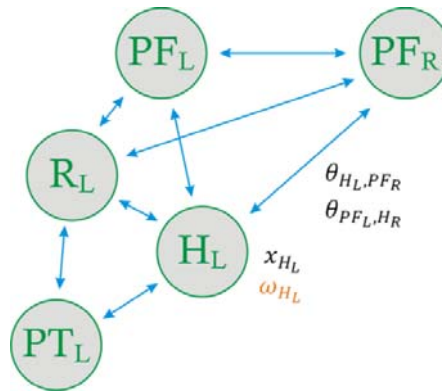


**Figure 6.1.** Example DCM formulation, to investigate effective connectivity with resting state fMRI data from the RUN-DMC cohort. The network is derived from (Daselaar et al., 2006), who report a function reorganization of this circuit in aging.  $\theta_{H_L,PFR}$  is the connection weight from  $H_L$  to  $H_R$ ,  $x_{H_L}$  is the activation state of  $H_L$ , and  $\omega_{H_L}$  is the structural integrity weight for  $H_L$ .

Since the BOLD signal is temporally blurred, with a latency of  $\sim 2$ s, the complexity of the underlying biophysics can be relatively low. Activity in region  $i$  can then be represented as a single state variable  $\hat{x}_i$ , representing neuronal activity (a so-called neural-mass model). The set of free parameters  $\theta$ , representing the effective connectivity between regions, can be assigned to each edge in the model. Our next task is to include our structural knowledge. For regional GM integrity, hippocampal volume and cortical thickness can be added as additional fixed parameters  $\omega$  on the model nodes; the activity of a region will then be multiplied by this value, where 1.0 indicates an intact, “normal” state (determined perhaps by the maximum value across subjects), and 0.0 indicates a complete lesion. WM integrity can be incorporated in the form of the prior probability term  $p(\vartheta | m)$  (see Section 1.4.3.3). Resting state activity can be simulated as external input to single regions of the network.

### 6.5.2. Mean Field Modelling

The DCM example of the previous section provides an interesting means of investigating specific questions of network connectivity. Larger-scale, more comprehensive computational models are possible however, whose purpose is typically to address more general questions of brain function, for which the RUN-DMC data set is also well-suited. Mean field models (MFMs) comprise a class of such large-scale forward models, which aim to simulate brain signals such as fMRI, PET, EEG, or MEG, in a realistic way which can subsequently be compared to and constrained by empirically observed evidence. An MFM is based upon the assumption that, at least in the cortex, individual and highly nonlinear neuronal activity can be approximated by taking a mean over a discrete region of the cortical sheet (depending on the resolution of the empirical data, typically 1-2mm for fMRI). To date, such models have been expressed on tessellated two-dimensional sheets with only local *extrinsic* connectivity between individual vertex-wise models and their neighbours, with a connection probability that decays exponentially with distance (Liley et al., 2002; Bojak and Liley, 2005). As shown in Figure 6.2, each vertex model is comprised of an excitatory and an inhibitory component, with excitatory and inhibitory connections between them referred to as *intrinsic* connectivity. The real brain has a three-dimensional convoluted cortex, an anatomically distinct parcellation, and specific patterns of long-range connectivity. Thus, an adaptation of this model is to include long-range connections between cortical regions; such connections are exclusively excitatory.

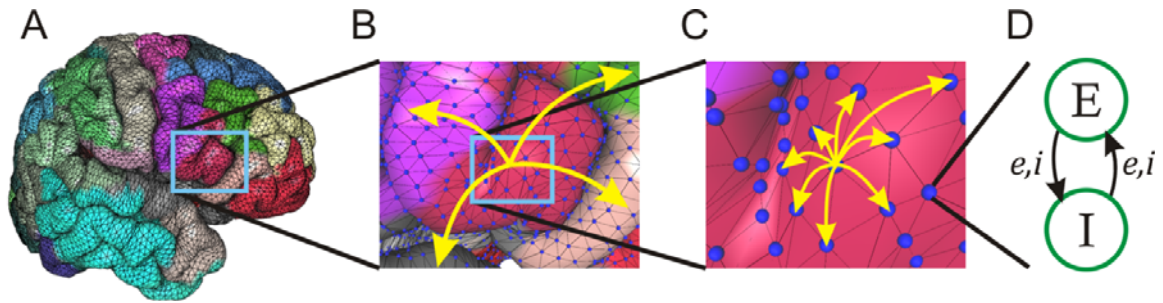


**Figure 6.2.** Mean field model (MFM) with realistic geometry. **A:** Individual cortical surface obtained using the Civet pipeline. Each vertex defines an individual MFM, and each MFM has three types of connectivity. **B:** Long-range (interregional) extrinsic connectivity connects a vertex to vertices in other cortical regions. **C:** Short-range (local) extrinsic connectivity connects a vertex to its neighbours with a strength that decays exponentially with distance. **D:** Intrinsic connectivity consists of excitatory ( $e$ ) and inhibitory ( $i$ ) connections between  $E$  and  $I$  pools of neurons.

Cortical surface representations, along with diffusion tractography and tract tracing information, provide a natural means of extending MFMs with realistic geometry and connectivity. Recently, my colleagues and I (Bojak et al., 2010) have proposed an implementation of such a realistic MFM, which requires a number of components, minimally: (1.) an accurate cortical surface representation, with a resolution that compromises between spatial fidelity and computational complexity; (2.) an accurate cortical parcellation, such as the RM, discussed in Section 5.2.1; (3.) a transfer function which maps from neuronal activity to observable signals (for BOLD, this is a hemodynamic response function; for EEG, this is a model of how signals are conducted through tissue volumes, including skull and scalp); (4.) a connectivity matrix, describing the patterns of long-range structural connectivity between cortical regions, such as can be obtained via CoCoMac or DWI tractography (or likely a combination of these); (5.) an estimate of signal transmission latency through these long-range connections. Additionally, such a model requires the specification of connection strengths, which are very difficult to obtain through direct empirical means; the closest approximation to this is a measure of projection density obtained from macaque tract tracing, but this approximation fails to model synaptic strength or multiple axonal terminations.

Connection strengths, and other undeterminable biophysical variables, can be treated as free parameters, to be estimated on the basis of model inversion. Thus, once the realistic MFM has been constructed, the next step is to simulate signals and then estimate connection strengths on the basis of real signals observed from the individual from whom the geometry was obtained. The resting state fMRI data that is available with the RUN-DMC data set can be used for this purpose; however, a modality with higher temporal resolution, such as EEG or MEG, which can capture oscillatory behaviour, is also desirable. Given the vast number of parameters to fit, and the relatively few mean field signals, such an inversion is a daunting task even with such a rich set of data; thus further simplifying assumptions are likely necessary.

A realistic MFM of the whole human brain, constrained by empirical evidence, would have incredible benefits for both basic research and clinical practice. Such a model formulation can be experimentally manipulated in basically any conceivable way, many of which manipulations are impossible or severely limited for human or even animal subjects. Having trained the model on intact brains, for instance, the degree to which the model can predict

the functional outcomes of focal GM lesions, or WM degradation, can be assessed. An accurate predictive model can generate any number of falsifiable hypotheses, prior to animal or clinical research. Moreover, the biophysics of the model can be extended to include neuromodulation, synaptic plasticity, or other forms of increased complexity, without the need to alter the underlying framework. Such large-scale models can also be used to test the validity of more targeted DCMs, since the underlying ground truth is known *a priori* (Lee et al., 2006b).

### ***6.5.3. Longitudinal Data***

The prospect of a follow-up study for the RUN-DMC cohort allows for a number of intriguing extensions to the data sets reported here. While in the present cross-sectional design we are only able to describe *trends* across an aging population, the existence of time-elapsing information permits the extraction of within-subject information that is invaluable for understanding the progression of aging and SVD-related effects. A number of studies have investigated the progression of cortical thickness, for instance, over time. (Gogtay et al., 2004) obtained cortical surfaces for individuals between the ages of 4 and 21, every two years for 8 to 10 years, and produced time-elapsing movies which demonstrated the development of the cortex over this period, with somatosensory and visual cortex preceding higher-order cortical regions. In an older cohort, (Thompson et al., 2003) investigated the progression of cortical GM thinning in Alzheimer's Disease patients and age-matched controls, scanned twice over a two-year period. They report a distinct pattern of progression, which corresponds to the pattern of neurofibrillary tangles and plaques observed in postmortem examinations: deterioration originating in temporal and limbic regions, and gradually spreading to frontal and occipital regions. Both of these studies provide a clear precedent for a similar investigation in our SVD cohort. Such spatiotemporal information can be used to pinpoint the origin of pathological conditions and thus help with clinical prognosis, the elucidation of their mechanisms, and their possible prevention.

Longitudinal data should also prove informative for analyses of effective connectivity and computational modelling. Cognitive theories such as neurocognitive scaffolding and dedifferentiation can be directly tested with the addition of a temporal aspect, that can demonstrate distinct changes both to functional and structural connectivity, and consequently effective connectivity. The daunting task of generative model inversion, discussed in the previous section, can potentially be simplified by the existence of empirical evidence from the same system, with altered morphology that can be directly measured using the morphological techniques described here. In sum, the addition of a new temporal dimension to the wealth of cross-sectional data that is already available for the methods I have discussed, promises a wealth of scientific discoveries for the considerable future. As such, it is perhaps the most appropriate place to conclude this dissertation, with gratitude to the reader who has followed to the end.

## 7. References

- Abraham M, Kötter R, Krumnack A, and Wanke E (2006). A connectivity rating for vertices in networks. In: Proceedings of the 4th IFIP International Conference on Theoretical Computer Science (Berlin: Springer), pp. 283-298.
- Achard S, and Bullmore E (2007). Efficiency and cost of economical brain functional networks. *PLoS Comput. Biol* 3 (2), e17.
- Albert, Jeong, and Barabasi (2000). Error and attack tolerance of complex networks. *Nature* 406 (6794), 378-382.
- Amunts K, Schleicher A, Bürgel U, Mohlberg H, Uylings HB, and Zilles K (1999). Broca's region revisited: cytoarchitecture and intersubject variability. *J. Comp. Neurol* 412 (2), 319-341.
- Amunts K, and Zilles K (2001). Advances in cytoarchitectonic mapping of the human cerebral cortex. *Neuroimaging Clin. N. Am* 11 (2), 151-169.
- Andersson JLR, and Skare S (2002). A model-based method for retrospective correction of geometric distortions in diffusion-weighted EPI. *Neuroimage* 16 (1), 177-199.
- Andrés P, Guerrini C, Phillips LH, and Perfect TJ (2008). Differential effects of aging on executive and automatic inhibition. *Dev Neuropsychol* 33 (2), 101-123.
- Apostolova LG, Akopyan GG, Partiali N, Steiner CA, Dutton RA, Hayashi KM, Dinov ID, Toga AW, Cummings JL, and Thompson PM (2007). Structural correlates of apathy in Alzheimer's disease. *Dement Geriatr Cogn Disord* 24 (2), 91-97.
- Apostolova LG, and Thompson PM (2007). Brain mapping as a tool to study neurodegeneration. *Neurotherapeutics* 4 (3), 387-400.
- Ashburner J, and Friston KJ (1999). Nonlinear spatial normalization using basis functions. *Hum Brain Mapp* 7 (4), 254-266.
- Ashburner J, and Friston KJ (2000). Voxel-based morphometry--the methods. *Neuroimage* 11 (6 Pt 1), 805-821.
- Bailey P, and von Bonin G (1951). *The Isocortex of Man* (Urbana: University of Illinois Press).
- Baltes PB, and Lindenberger U (1997). Emergence of a powerful connection between sensory and cognitive functions across the adult life span: a new window to the study of cognitive aging? *Psychol Aging* 12 (1), 12-21.
- Barone P, Batardiere A, Knoblauch K, and Kennedy H (2000). Laminar distribution of neurons in extrastriate areas projecting to visual areas V1 and V4 correlates with the hierarchical rank and indicates the operation of a distance rule. *J. Neurosci* 20 (9), 3263-3281.
- Batardière A, Barone P, Knoblauch K, Giroud P, Berland M, Dumas A, and Kennedy H (2002). Early specification of the hierarchical organization of visual cortical areas in the macaque monkey. *Cereb. Cortex* 12 (5), 453-465.

## References

- Behrens TEJ, Berg HJ, Jbabdi S, Rushworth MFS, and Woolrich MW (2007). Probabilistic diffusion tractography with multiple fibre orientations: What can we gain? *Neuroimage* 34 (1), 144-155.
- Behrens TEJ, Woolrich MW, Jenkinson M, Johansen-Berg H, Nunes RG, Clare S, Matthews PM, Brady JM, and Smith SM (2003). Characterization and propagation of uncertainty in diffusion-weighted MR imaging. *Magn Reson Med* 50 (5), 1077-1088.
- Benjamini Y, and Yekutieli D (2001). The control of the false discovery rate in multiple testing under dependency. *The Annals of Statistics* 29 (4), 1165-1188.
- Bezgin G, Wanke E, Krumnack A, and Kötter R (2008). Deducing logical relationships between spatially registered cortical parcellations under conditions of uncertainty. *Neural Netw* 21 (8), 1132-1145.
- Bojak I, and Liley DTJ (2005). Modeling the effects of anesthesia on the electroencephalogram. *Phys Rev E Stat Nonlin Soft Matter Phys* 71 (4 Pt 1), 041902.
- Bojak I, Oostendorp TF, Reid AT, and Kötter R (2010). Connecting Mean Field Models of Neural Activity to EEG and fMRI Data. *Brain Topogr* 23 (2), 139-149.
- Brandes U (2001). A faster algorithm for betweenness centrality. *Journal of Mathematical Sociology* 25 (2), 163-177.
- Broca P (1861). Sur le principe des localisations cérébrales. *Bulletin de la Société d'Anthropologie* 2, 190-204.
- Brodmann K (1905). Beiträge zur histologischen Lokalisation der Grosshirnrinde. Dritte Mitteilung: Die Rindenfelder der niederen Affen. *J. Psychol. Neurol. Lpz.* 4, 177-226.
- Brodmann K (1909). Vergleichende Lokalisationslehre der Grosshirnrinde in ihren Prinzipien dargestellt auf Grund des Zellenbaues (Leipzig: Johann Ambrosius Barth Verlag).
- Büchel C, and Friston KJ (1997). Effective connectivity and neuroimaging. In: *Human Brain Function* (San Diego: Academic Press).
- Campbell AW (1905). *Histological studies on the localisation of cerebral function* (Cambridge: Cambridge University Press).
- Chang A, Lad EM, and Lad SP (2007). Hippocrates' influence on the origins of neurosurgery. *Neurosurg Focus* 23 (1), E9.
- Charvet G, Rousseau L, Billoint O, Gharbi S, Rostaing J, Joucla S, Trevisiol M, Bourgerette A, Chauvet P, Moulin C, et al. (2010). BioMEA: a versatile high-density 3D microelectrode array system using integrated electronics. *Biosens Bioelectron* 25 (8), 1889-1896.
- Chumbley JR, and Friston KJ (2009). False discovery rate revisited: FDR and topological inference using Gaussian random fields. *Neuroimage* 44 (1), 62-70.
- Cocosco CA, Zijdenbos AP, and Evans AC (2003). A fully automatic and robust brain MRI tissue classification method. *Med Image Anal* 7 (4), 513-527.

- Colcombe SJ, Kramer AF, Erickson KI, and Scalf P (2005). The implications of cortical recruitment and brain morphology for individual differences in inhibitory function in aging humans. *Psychol Aging* 20 (3), 363-375.
- Collins DL, Neelin P, Peters TM, and Evans AC (1994). Automatic 3D intersubject registration of MR volumetric data in standardized Talairach space. *J Comput Assist Tomogr* 18 (2), 192-205.
- Dale AM, and Sereno MI (1993). Improved localization of cortical activity by combining EEG and MEG with MRI cortical surface reconstruction: a linear approach. *J Cogn Neurosci* 5, 162-176.
- Damoiseaux JS, Beckmann CF, Arigita EJS, Barkhof F, Scheltens P, Stam CJ, Smith SM, and Rombouts SARB (2008). Reduced resting-state brain activity in the "default network" in normal aging. *Cereb. Cortex* 18 (8), 1856-1864.
- Daselaar SM, Fleck MS, Dobbins IG, Madden DJ, and Cabeza R (2006). Effects of healthy aging on hippocampal and rhinal memory functions: an event-related fMRI study. *Cereb. Cortex* 16 (12), 1771-1782.
- Daunizeau J, David O, and Stephan KE (2009). Dynamic causal modelling: A critical review of the biophysical and statistical foundations. *Neuroimage*. Available at: <http://www.ncbi.nlm.nih.gov/pubmed/19961941> [Accessed April 26, 2010].
- De Groot JC, De Leeuw F, Oudkerk M, Van Gijn J, Hofman A, Jolles J, and Breteler MMB (2002). Periventricular cerebral white matter lesions predict rate of cognitive decline. *Ann. Neurol* 52 (3), 335-341.
- De Renzi E (2000). Disorders of visual recognition. *Semin Neurol* 20 (4), 479-485.
- Dekaban AS (1978). Changes in brain weights during the span of human life: relation of brain weights to body heights and body weights. *Ann. Neurol* 4 (4), 345-356.
- Dennis NA, Daselaar S, and Cabeza R (2007). Effects of aging on transient and sustained successful memory encoding activity. *Neurobiol. Aging* 28 (11), 1749-1758.
- Desimone R (1991). Face-Selective Cells in the Temporal Cortex of Monkeys. *Journal of Cognitive Neuroscience* 3 (1), 1-8.
- Dickstein SG, Bannon K, Castellanos FX, and Milham MP (2006). The neural correlates of attention deficit hyperactivity disorder: an ALE meta-analysis. *J Child Psychol Psychiatry* 47 (10), 1051-1062.
- von Economo C, and Koskina GN (1926). Die Cytoarchitektonik der Hirnrinde des erwachsenen Menschen. (The Cyto-Architectonics of the Cerebral Cortex of Adult Man.). *Arch Neurol Psychiatry*. Available at: <http://archneurpsyc.ama-assn.org> [Accessed April 29, 2010].
- Eickhoff S, Walters NB, Schleicher A, Kril J, Egan GF, Zilles K, Watson JDG, and Amunts K (2005a). High-resolution MRI reflects myeloarchitecture and cytoarchitecture of human cerebral cortex. *Hum Brain Mapp* 24 (3), 206-215.
- Eickhoff SB, Stephan KE, Mohlberg H, Grefkes C, Fink GR, Amunts K, and Zilles K (2005b). A

## References

- new SPM toolbox for combining probabilistic cytoarchitectonic maps and functional imaging data. *Neuroimage* 25 (4), 1325-1335.
- Erdős P, and Rényi A (1959). On Random Graphs I. *Publicationes Mathematicae* 6, 290-297.
- Felleman DJ, Burkhalter A, and Van Essen DC (1997). Cortical connections of areas V3 and VP of macaque monkey extrastriate visual cortex. *J. Comp. Neurol* 379 (1), 21-47.
- Felleman DJ, and Van Essen DC (1991). Distributed hierarchical processing in the primate cerebral cortex. *Cereb. Cortex* 1 (1), 1-47.
- Fera F, Weickert TW, Goldberg TE, Tessitore A, Hariri A, Das S, Lee S, Zolnick B, Meeter M, Myers CE, et al. (2005). Neural mechanisms underlying probabilistic category learning in normal aging. *J. Neurosci* 25 (49), 11340-11348.
- Fishman RS (2007). The Nobel Prize of 1906. *Arch. Ophthalmol* 125 (5), 690-694.
- Flood DG, and Coleman PD (1988). Neuron numbers and sizes in aging brain: comparisons of human, monkey, and rodent data. *Neurobiol. Aging* 9 (5-6), 453-463.
- Fransson P (2006). How default is the default mode of brain function? Further evidence from intrinsic BOLD signal fluctuations. *Neuropsychologia* 44 (14), 2836-2845.
- Freeman LC (1977). A set of measures of centrality based on betweenness. *Sociometry* 40, 35-41.
- Freeman LC (1978). Centrality in social networks conceptual clarification. *Social Networks* 1 (3), 215-239.
- Fries P (2009). Neuronal gamma-band synchronization as a fundamental process in cortical computation. *Annu. Rev. Neurosci* 32, 209-224.
- Fritsch G, and Hitzig E (1960). On the electrical excitability of the cerebrum (1870). In: Some Papers on the Cerebral Cortex (Springfield: Thomas), pp. 73-96.
- Gall FJ (1835). On the Functions of the Brain and of Each of Its Parts: Organology; or, An exposition of the instincts, propensities, sentiments, and talents, or the moral qualities, and the fundamental intellectual faculties in man and animals, and the seat of their organs (Boston: Marsh, Capen & Lyon).
- Genovese CR, Lazar NA, and Nichols T (2002). Thresholding of statistical maps in functional neuroimaging using the false discovery rate. *Neuroimage* 15 (4), 870-878.
- Gogtay N, Giedd JN, Lusk L, Hayashi KM, Greenstein D, Vaituzis AC, Nugent TF, Herman DH, Clasen LS, Toga AW, et al. (2004). Dynamic mapping of human cortical development during childhood through early adulthood. *Proc. Natl. Acad. Sci. U.S.A* 101 (21), 8174-8179.
- Good CD, Johnsrude IS, Ashburner J, Henson RN, Friston KJ, and Frackowiak RS (2001). A voxel-based morphometric study of ageing in 465 normal adult human brains. *Neuroimage* 14 (1 Pt 1), 21-36.
- Grady CL (2008). Cognitive neuroscience of aging. *Ann. N. Y. Acad. Sci* 1124, 127-144.

- Grady CL, Springer MV, Hongwanishkul D, McIntosh AR, and Winocur G (2006). Age-related changes in brain activity across the adult lifespan. *J Cogn Neurosci* 18 (2), 227-241.
- Grady CL, Yu H, and Alain C (2008). Age-related differences in brain activity underlying working memory for spatial and nonspatial auditory information. *Cereb. Cortex* 18 (1), 189-199.
- Greicius MD, Krasnow B, Reiss AL, and Menon V (2003). Functional connectivity in the resting brain: A network analysis of the default mode hypothesis. *Proc Natl Acad Sci U S A* 100 (1), 253-258.
- Gross CG, Rocha-Miranda CE, and Bender DB (1972). Visual properties of neurons in inferotemporal cortex of the Macaque. *J. Neurophysiol* 35 (1), 96-111.
- Gunning-Dixon FM, and Raz N (2003). Neuroanatomical correlates of selected executive functions in middle-aged and older adults: a prospective MRI study. *Neuropsychologia* 41 (14), 1929-1941.
- Guo S, Wu J, Ding M, and Feng J (2008). Uncovering interactions in the frequency domain. *PLoS Comput. Biol* 4 (5), e1000087.
- He Y, Dagher A, Chen Z, Charil A, Zijdenbos A, Worsley K, and Evans A (2009). Impaired small-world efficiency in structural cortical networks in multiple sclerosis associated with white matter lesion load. *Brain* 132 (Pt 12), 3366-3379.
- Hebert LE, Scherr PA, Bienias JL, Bennett DA, and Evans DA (2003). Alzheimer disease in the US population: prevalence estimates using the 2000 census. *Arch. Neurol* 60 (8), 1119-1122.
- Hegd  J, and Felleman DJ (2007). Reappraising the functional implications of the primate visual anatomical hierarchy. *Neuroscientist* 13 (5), 416-421.
- Hellwig B (2000). A quantitative analysis of the local connectivity between pyramidal neurons in layers 2/3 of the rat visual cortex. *Biological Cybernetics* 82 (2), 111-121.
- Hilgetag C, O'neill MA, and Young MP (1996). On Hierarchies: *Science* 271 (5250), 777b.
- Hilgetag CC, and Grant S (2010). Cytoarchitectural differences are a key determinant of laminar projection origins in the visual cortex. *Neuroimage* 51 (3), 1006-1017.
- Holmes CJ, Hoge R, Collins L, Woods R, Toga AW, and Evans AC (1998). Enhancement of MR images using registration for signal averaging. *J Comput Assist Tomogr* 22 (2), 324-333.
- Honey CJ, K tter R, Breakspear M, and Sporns O (2007). Network structure of cerebral cortex shapes functional connectivity on multiple time scales. *Proc. Natl. Acad. Sci. U.S.A* 104 (24), 10240-10245.
- Houk JC, and Wise SP (1995). Distributed modular architectures linking basal ganglia, cerebellum, and cerebral cortex: their role in planning and controlling action. *Cereb. Cortex* 5 (2), 95-110.
- Hubel DH, and Wiesel TN (1959). Receptive fields of single neurones in the cat's striate cortex. *J*

## References

- Physiol* 148, 574-591.
- Humphries MD, and Gurney K (2008). Network 'small-world-ness': a quantitative method for determining canonical network equivalence. *PLoS ONE* 3 (4), e0002051.
- Hutton C, Draganski B, Ashburner J, and Weiskopf N (2009). A comparison between voxel-based cortical thickness and voxel-based morphometry in normal aging. *Neuroimage* 48 (2), 371-380.
- Hyvärinen A, Karhunen J, and Oja E (2001). Independent Component Analysis S. Haykin, ed. (New York, USA: John Wiley & Sons, Inc.).
- Jansons KM, and Alexander DC (2003). Persistent Angular Structure: new insights from diffusion MRI data. Dummy version. *Inf Process Med Imaging* 18, 672-683.
- Jernigan TL, Archibald SL, Fennema-Notestine C, Gamst AC, Stout JC, Bonner J, and Hesselink JR (2001). Effects of age on tissues and regions of the cerebrum and cerebellum. *Neurobiol. Aging* 22 (4), 581-594.
- Jonides J, Marshuetz C, Smith EE, Reuter-Lorenz PA, Koeppel RA, and Hartley A (2000). Age differences in behavior and PET activation reveal differences in interference resolution in verbal working memory. *J Cogn Neurosci* 12 (1), 188-196.
- Kaiser M, and Hilgetag CC (2004). Edge vulnerability in neural and metabolic networks. *Biological Cybernetics* 90 (5), 311-317.
- Kanwisher N, McDermott J, and Chun MM (1997). The fusiform face area: a module in human extrastriate cortex specialized for face perception. *J. Neurosci* 17 (11), 4302-4311.
- Kass M, Witkin A, and Terzopoulos D (1988). Snakes: Active contour models. *Intl. J. Comp. Vis.* 1 (4), 321--331.
- Keightley ML, Chiew KS, Anderson JAE, and Grady CL (2010). Neural correlates of recognition memory for emotional faces and scenes. *Soc Cogn Affect Neurosci*. Available at: <http://www.ncbi.nlm.nih.gov/pubmed/20194514> [Accessed April 25, 2010].
- Kennedy D, Lange N, Makris N, Bates J, Meyer J, and Caviness V (1998). Gyri of the human neocortex: an MRI-based analysis of volume and variance. *Cereb. Cortex* 8 (4), 372-384.
- Kennedy H, and Bullier J (1985). A double-labeling investigation of the afferent connectivity to cortical areas V1 and V2 of the macaque monkey. *J. Neurosci* 5 (10), 2815-2830.
- Kim JS, Singh V, Lee JK, Lerch J, Ad-Dab'bagh Y, MacDonald D, Lee JM, Kim SI, and Evans AC (2005). Automated 3-D extraction and evaluation of the inner and outer cortical surfaces using a Laplacian map and partial volume effect classification. *Neuroimage* 27 (1), 210-221.
- Kötter R, Stephan KE, Palomero-Gallagher N, Geyer S, Schleicher A, and Zilles K (2001). Multimodal characterisation of cortical areas by multivariate analyses of receptor binding and connectivity data. *Anat. Embryol* 204 (4), 333-350.
- Kötter R (2004). Online retrieval, processing, and visualization of primate connectivity data from

- the CoCoMac database. *Neuroinformatics* 2 (2), 127-144.
- Kötter R, Reid AT, Krumnack A, Wanke E, and Sporns O (2007). Shapley ratings in brain networks. *Front Neuroinformatics* 1, 2.
- Kötter R, and Stephan KE (2003). Network participation indices: characterizing component roles for information processing in neural networks. *Neural Netw* 16 (9), 1261-1275.
- Kötter R, and Wanke E (2005). Mapping brains without coordinates. *Philos. Trans. R. Soc. Lond., B, Biol. Sci* 360 (1456), 751-766.
- Krumnack A, Reid AT, Wanke E, Bezgin G, and Kötter R (2010). Criteria for optimizing cortical hierarchies with continuous ranges. *Front Neuroinformatics* 4, 7.
- Kwee RM, and Kwee TC (2007). Virchow-Robin spaces at MR imaging. *Radiographics* 27 (4), 1071-1086.
- Lashley K (1950). In search of the engram. *Society of Experimental Biology Symposium* 4, 454-482.
- Latham P, and Roudi Y (2009). Mutual information. *Scholarpedia* 4 (1), 1658.
- Launer LJ (2003). Epidemiology of white-matter lesions. *Int Psychogeriatr* 15 Suppl 1, 99-103.
- Lazar M, and Alexander AL (2005). Bootstrap white matter tractography (BOOT-TRAC). *Neuroimage* 24 (2), 524-532.
- Le Bihan D (2003). Looking into the functional architecture of the brain with diffusion MRI. *Nat. Rev. Neurosci* 4 (6), 469-480.
- Lee JK, Lee J, Kim JS, Kim IY, Evans AC, and Kim SI (2006a). A novel quantitative cross-validation of different cortical surface reconstruction algorithms using MRI phantom. *Neuroimage* 31 (2), 572-584.
- Lee L, Friston K, and Horwitz B (2006b). Large-scale neural models and dynamic causal modelling. *Neuroimage* 30 (4), 1243-1254.
- de Leeuw FE, de Groot JC, and van Gijn J (2001). Cerebral white matter lesions in the elderly: vascular risk factors and cognitive consequences. *Ned Tijdschr Geneesk* 145 (43), 2067-2071.
- de Leeuw F, de Groot JC, Oudkerk M, Wittteman JCM, Hofman A, van Gijn J, and Breteler MMB (2002). Hypertension and cerebral white matter lesions in a prospective cohort study. *Brain* 125 (Pt 4), 765-772.
- Lerch JP, Pruessner JC, Zijdenbos A, Hampel H, Teipel SJ, and Evans AC (2005). Focal decline of cortical thickness in Alzheimer's disease identified by computational neuroanatomy. *Cereb. Cortex* 15 (7), 995-1001.
- Liley DTJ, Cadusch PJ, and Dafilis MP (2002). A spatially continuous mean field theory of electrocortical activity. *Network: Computation in Neural Systems* 13 (1), 67.

## References

- Lyttelton O, Boucher M, Robbins S, and Evans A (2007). An unbiased iterative group registration template for cortical surface analysis. *Neuroimage* 34 (4), 1535-1544.
- MacDonald D, Kabani N, Avis D, and Evans AC (2000). Automated 3-D extraction of inner and outer surfaces of cerebral cortex from MRI. *Neuroimage* 12 (3), 340-356.
- Mai JK, Assheuer J, and Paxinos G (1997). Atlas of the human brain (San Diego: Academic Press).
- Maldjian JA, Laurienti PJ, Kraft RA, and Burdette JH (2003). An automated method for neuroanatomic and cytoarchitectonic atlas-based interrogation of fMRI data sets. *Neuroimage* 19 (3), 1233-1239.
- Mattay VS, Fera F, Tessitore A, Hariri AR, Berman KF, Das S, Meyer-Lindenberg A, Goldberg TE, Callicott JH, and Weinberger DR (2006). Neurophysiological correlates of age-related changes in working memory capacity. *Neurosci. Lett* 392 (1-2), 32-37.
- Maunsell JH, and Van Essen DC (1983). The connections of the middle temporal visual area (MT) and their relationship to a cortical hierarchy in the macaque monkey. *J. Neurosci* 3 (12), 2563-2586.
- Mayberg HS, Lozano AM, Voon V, McNeely HE, Seminowicz D, Hamani C, Schwalb JM, and Kennedy SH (2005). Deep brain stimulation for treatment-resistant depression. *Neuron* 45 (5), 651-660.
- Mazziotta J, Toga A, Evans A, Fox P, Lancaster J, Zilles K, Woods R, Paus T, Simpson G, Pike B, et al. (2001). A probabilistic atlas and reference system for the human brain: International Consortium for Brain Mapping (ICBM). *Philos. Trans. R. Soc. Lond., B, Biol. Sci* 356 (1412), 1293-1322.
- McIntosh AR, and Gonzalez-Lima F (1991). Structural modeling of functional neural pathways mapped with 2-deoxyglucose: effects of acoustic startle habituation on the auditory system. *Brain Res* 547 (2), 295-302.
- Meier-Ruge W, Bruder A, and Theodore D (1992). Histochemical and morphometric investigation of the pathogenesis of acute brain infarction in primates. *Acta Histochem. Suppl* 42, 59-70.
- Meynert T (1868). Der Bau der Grosshirnrinde und seine örtlichen Verschiedenheiten, nebst einem pathologisch-anatomischen Korollarium. *Vjschr. Psychiatr. Vienna*. 1, 77-93.
- Moseley ME, Cohen Y, Kucharczyk J, Mintorovitch J, Asgari HS, Wendland MF, Tsuruda J, and Norman D (1990). Diffusion-weighted MR imaging of anisotropic water diffusion in cat central nervous system. *Radiology* 176 (2), 439-445.
- Narr KL, Bilder RM, Toga AW, Woods RP, Rex DE, Szeszko PR, Robinson D, Sevy S, Gunduz-Bruce H, Wang Y, et al. (2005). Mapping cortical thickness and gray matter concentration in first episode schizophrenia. *Cereb. Cortex* 15 (6), 708-719.
- Nielson KA, Langenecker SA, and Garavan H (2002). Differences in the functional neuroanatomy of inhibitory control across the adult life span. *Psychol Aging* 17 (1), 56-71.
- van Norden AGW, Fick WF, de Laat KF, van Uden IWM, van Oudheusden LJB, Tendolkar I,

- Zwiers MP, and de Leeuw FE (2008). Subjective cognitive failures and hippocampal volume in elderly with white matter lesions. *Neurology* 71 (15), 1152-1159.
- Nusbaum AO, Tang CY, Buchsbaum MS, Wei TC, and Atlas SW (2001). Regional and global changes in cerebral diffusion with normal aging. *AJNR Am J Neuroradiol* 22 (1), 136-142.
- O'Brien J (2003). Behavioral symptoms in vascular cognitive impairment and vascular dementia. *Int Psychogeriatr* 15 Suppl 1, 133-138.
- Papadimitriou CH, and Steiglitz K (1998). Combinatorial optimization (Mineola, New York: Courier Dover Publications).
- Park DC, and Reuter-Lorenz P (2009). The adaptive brain: aging and neurocognitive scaffolding. *Annu Rev Psychol* 60, 173-196.
- Parker GJM, and Alexander DC (2005). Probabilistic anatomical connectivity derived from the microscopic persistent angular structure of cerebral tissue. *Philos. Trans. R. Soc. Lond., B, Biol. Sci* 360 (1457), 893-902.
- Passingham RE, Stephan KE, and Kötter R (2002). The anatomical basis of functional localization in the cortex. *Nat. Rev. Neurosci* 3 (8), 606-616.
- Paxinos G, Huang X, and Toga AW (1999). The Rhesus Monkey Brain in Stereotaxic Coordinates 1st ed. (San Diego: Academic Press).
- Penny WD, Stephan KE, Mechelli A, and Friston KJ (2004). Modelling functional integration: a comparison of structural equation and dynamic causal models. *Neuroimage* 23 Suppl 1, S264-274.
- Penny W, Kiebel S, and Friston K (2003). Variational Bayesian inference for fMRI time series. *Neuroimage* 19 (3), 727-741.
- Perrett DI, Oram MW, Harries MH, Bevan R, Hietanen JK, Benson PJ, and Thomas S (1991). Viewer-centred and object-centred coding of heads in the macaque temporal cortex. *Exp Brain Res* 86 (1), 159-173.
- Persson J, Lustig C, Nelson JK, and Reuter-Lorenz PA (2007). Age differences in deactivation: a link to cognitive control? *J Cogn Neurosci* 19 (6), 1021-1032.
- Pfefferbaum A, Sullivan EV, Hedehus M, Lim KO, Adalsteinsson E, and Moseley M (2000). Age-related decline in brain white matter anisotropy measured with spatially corrected echo-planar diffusion tensor imaging. *Magn Reson Med* 44 (2), 259-268.
- Preul C, Lohmann G, Hund-Georgiadis M, Guthke T, and von Cramon DY (2005). Morphometry demonstrates loss of cortical thickness in cerebral microangiopathy. *J. Neurol* 252 (4), 441-447.
- Ptolemy 2C Ptolemy's Geographia [Electronic resource] : Books I & II. *Oxford University Computing Services*. Available at: <http://ota.ahds.ac.uk/headers/2422.xml> [Accessed April 25, 2010].
- Raichle ME, and Snyder AZ (2007). A default mode of brain function: a brief history of an

## References

- evolving idea. *Neuroimage* 37 (4), 1083-1090.
- Raz N, Gunning FM, Head D, Dupuis JH, McQuain J, Briggs SD, Loken WJ, Thornton AE, and Acker JD (1997). Selective aging of the human cerebral cortex observed in vivo: differential vulnerability of the prefrontal gray matter. *Cereb. Cortex* 7 (3), 268-282.
- Raz N, Gunning-Dixon F, Head D, Rodrigue KM, Williamson A, and Acker JD (2004). Aging, sexual dimorphism, and hemispheric asymmetry of the cerebral cortex: replicability of regional differences in volume. *Neurobiol. Aging* 25 (3), 377-396.
- Reid AT, Krumnack A, Wanke E, and Kötter R (2009). Optimization of cortical hierarchies with continuous scales and ranges. *Neuroimage* 47 (2), 611-617.
- Reid AT, van Norden AGW, de Laat KF, van Oudheusden LJB, Zwiers MP, Evans AC, de Leeuw F, and Kötter R (2010). Patterns of cortical degeneration in an elderly cohort with cerebral small vessel disease. *Hum Brain Mapp.* Available at: <http://www.ncbi.nlm.nih.gov/pubmed/20336684> [Accessed April 25, 2010].
- Rengachary SS, and Wilkins RH (1996). *Neurosurgical Operative Atlas* (New York: Thieme Medical Publishers, Inc.).
- Restrepo JG, Ott E, and Hunt BR (2006). Characterizing the dynamical importance of network nodes and links. *Phys. Rev. Lett* 97 (9), 094102.
- Reuter-Lorenz PA, Jonides J, Smith EE, Hartley A, Miller A, Marshuetz C, and Koeppel RA (2000). Age differences in the frontal lateralization of verbal and spatial working memory revealed by PET. *J Cogn Neurosci* 12 (1), 174-187.
- Salat DH, Kaye JA, and Janowsky JS (1999). Prefrontal gray and white matter volumes in healthy aging and Alzheimer disease. *Arch. Neurol* 56 (3), 338-344.
- Salat DH, Tuch DS, Hevelone ND, Fischl B, Corkin S, Rosas HD, and Dale AM (2005). Age-related changes in prefrontal white matter measured by diffusion tensor imaging. *Ann. N. Y. Acad. Sci* 1064, 37-49.
- Salat DH, Buckner RL, Snyder AZ, Greve DN, Desikan RSR, Busa E, Morris JC, Dale AM, and Fischl B (2004). Thinning of the cerebral cortex in aging. *Cereb. Cortex* 14 (7), 721-730.
- Salat DH, Kaye JA, and Janowsky JS (2002). Greater orbital prefrontal volume selectively predicts worse working memory performance in older adults. *Cereb. Cortex* 12 (5), 494-505.
- Saleem KS, Suzuki W, Tanaka K, and Hashikawa T (2000). Connections between Anterior Inferotemporal Cortex and Superior Temporal Sulcus Regions in the Macaque Monkey. *J. Neurosci.* 20 (13), 5083-5101.
- Saleem KS, and Tanaka K (1996). Divergent Projections from the Anterior Inferotemporal Area TE to the Perirhinal and Entorhinal Cortices in the Macaque Monkey. *J. Neurosci.* 16 (15), 4757-4775.
- Schmidt R, Fazekas F, Enzinger C, Ropele S, Kapeller P, and Schmidt H (2002). Risk factors and progression of small vessel disease-related cerebral abnormalities. *J. Neural Transm.*

- Suppl* (62), 47-52.
- Schmidtke K, and Hüll M (2005). Cerebral small vessel disease: how does it progress? *J. Neurol. Sci* 229-230, 13-20.
- Shapley L (1953). A Value for n-person Games. In: Contributions to the Theory of Games (Princeton, NJ: Princeton University Press).
- Shattuck DW, Mirza M, Adisetiyo V, Hojatkashani C, Salamon G, Narr KL, Poldrack RA, Bilder RM, and Toga AW (2008). Construction of a 3D Probabilistic Atlas of Human Cortical Structures. *Neuroimage* 39 (3), 1064-1080.
- Sherbondy AJ, Dougherty RF, Ben-Shachar M, Napel S, and Wandell BA (2009). ConTrack: Finding the most likely pathways between brain regions using diffusion tractography. *J Vis* 8 (9), 15.1-1516.
- Sled JG, Zijdenbos AP, and Evans AC (1998). A nonparametric method for automatic correction of intensity nonuniformity in MRI data. *IEEE Trans Med Imaging* 17 (1), 87-97.
- Smith SM, Jenkinson M, Woolrich MW, Beckmann CF, Behrens TEJ, Johansen-Berg H, Bannister PR, De Luca M, Drobnjak I, Flitney DE, et al. (2004). Advances in functional and structural MR image analysis and implementation as FSL. *Neuroimage* 23 Suppl 1, S208-219.
- Sowell ER, Peterson BS, Thompson PM, Welcome SE, Henkenius AL, and Toga AW (2003). Mapping cortical change across the human life span. *Nat. Neurosci* 6 (3), 309-315.
- Sporns O, Tononi G, and Edelman G (2000). Theoretical Neuroanatomy: Relating Anatomical and Functional Connectivity in Graphs and Cortical Connection Matrices. *Cereb. Cortex* 10 (2), 127-141.
- Sporns O, and Honey CJ (2006). Small worlds inside big brains. *Proc. Natl. Acad. Sci. U.S.A* 103 (51), 19219-19220.
- Sporns O, Honey CJ, and Kötter R (2007). Identification and classification of hubs in brain networks. *PLoS ONE* 2 (10), e1049.
- Steffens DC, Skoog I, Norton MC, Hart AD, Tschanz JT, Plassman BL, Wyse BW, Welsh-Bohmer KA, and Breitner JCS (2000). Prevalence of Depression and Its Treatment in an Elderly Population: The Cache County Study. *Arch Gen Psychiatry* 57 (6), 601-607.
- Stejskal EO, and Tanner JE (1965). Spin Diffusion Measurements: Spin Echoes in the Presence of a Time-Dependent Field Gradient. *J. Chem. Phys.* 42 (1), 288.
- Stephan KE, Kamper L, Bozkurt A, Burns GA, Young MP, and Kötter R (2001). Advanced database methodology for the Collation of Connectivity data on the Macaque brain (CoCoMac). *Philos. Trans. R. Soc. Lond., B, Biol. Sci* 356 (1412), 1159-1186.
- Storey JD (2003). The Positive False Discovery Rate: A Bayesian Interpretation and the q-Value. *The Annals of Statistics* 31 (6), 2013-2035.
- Talairach J, and Tournoux P (1988). Co-Planar Stereotaxic Atlas of the Human Brain: 3-D

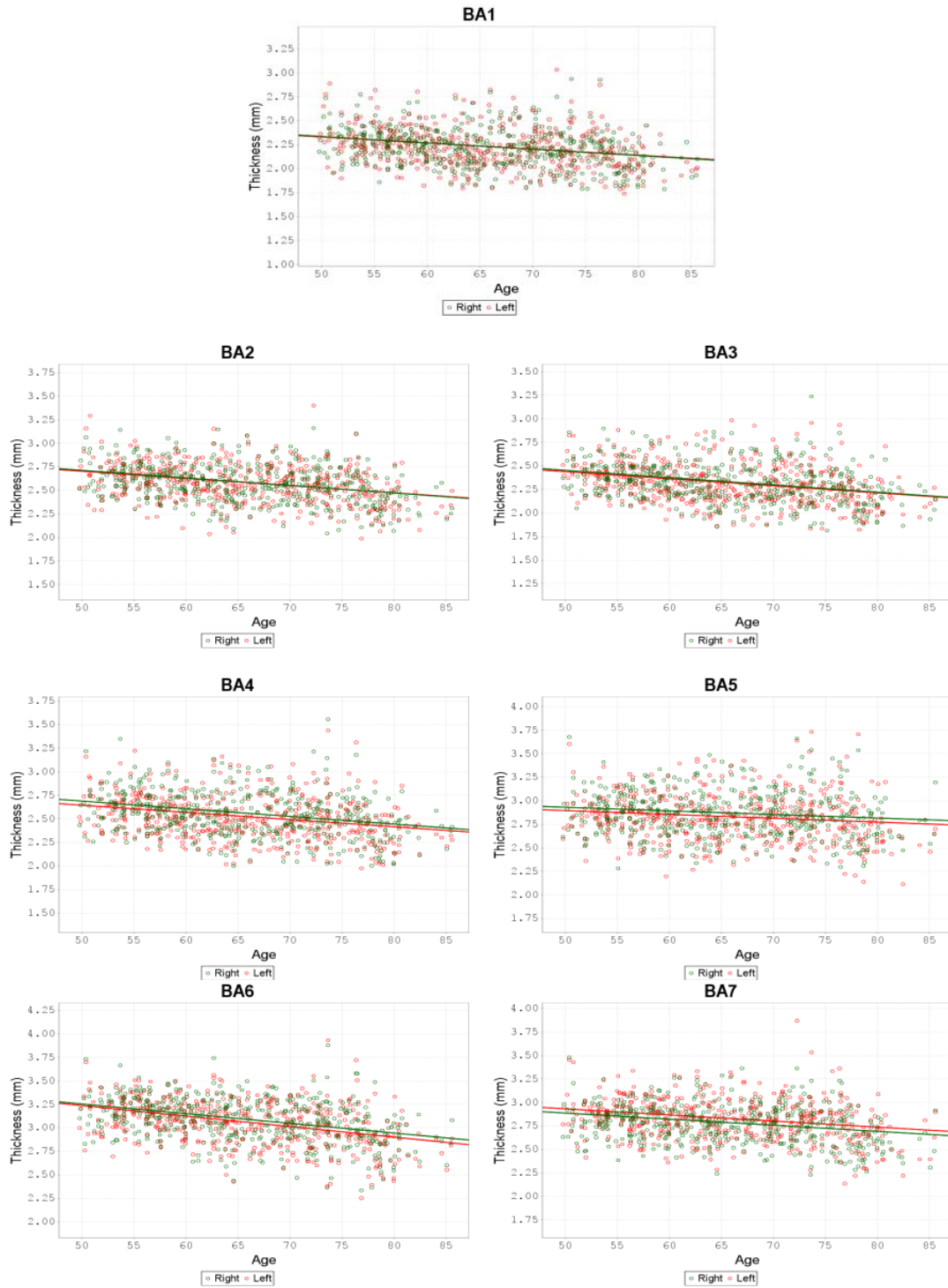
## References

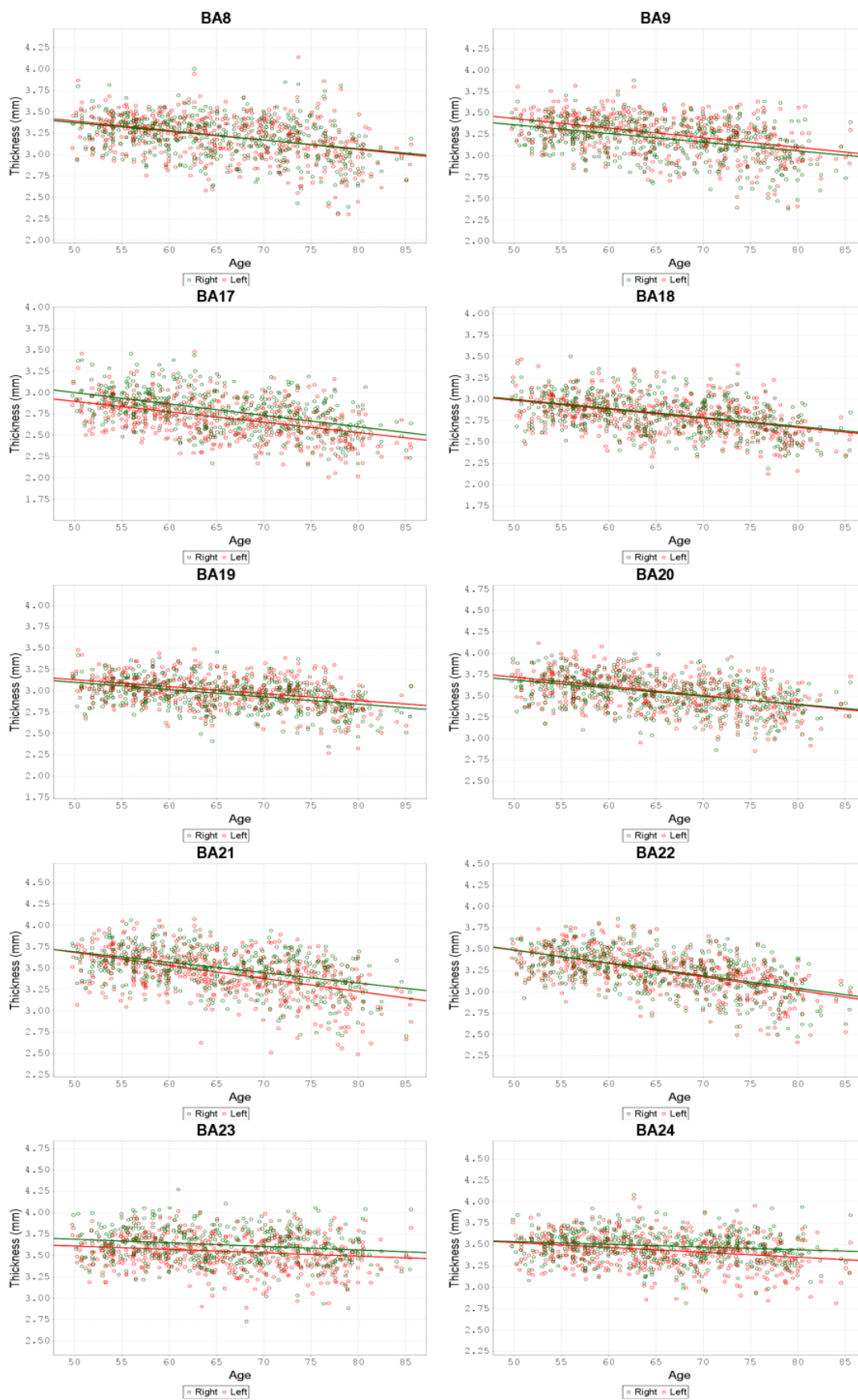
- Proportional System: An Approach to Cerebral Imaging (New York: Thieme Medical Publishers, Inc.).
- Tamura H, and Tanaka K (2001). Visual Response Properties of Cells in the Ventral and Dorsal Parts of the Macaque Inferotemporal Cortex. *Cereb. Cortex* 11 (5), 384-399.
- Taniwaki T, Okayama A, Yoshiura T, Togao O, Nakamura Y, Yamasaki T, Ogata K, Shigeto H, Ohyagi Y, Kira J, et al. (2007). Age-related alterations of the functional interactions within the basal ganglia and cerebellar motor loops in vivo. *Neuroimage* 36 (4), 1263-1276.
- Thompson PM, MacDonald D, Mega MS, Holmes CJ, Evans AC, and Toga AW (1997). Detection and mapping of abnormal brain structure with a probabilistic atlas of cortical surfaces. *J Comput Assist Tomogr* 21 (4), 567-581.
- Thompson PM, Hayashi KM, de Zubicaray G, Janke AL, Rose SE, Semple J, Herman D, Hong MS, Dittmer SS, Doddrell DM, et al. (2003). Dynamics of Gray Matter Loss in Alzheimer's Disease. *J. Neurosci.* 23 (3), 994-1005.
- Travers J, and Milgram S (1969). An Experimental Study of the Small World Problem. *Sociometry* 32 (4), 425-443.
- Tuch DS, Wedeen VJ, Dale AM, George JS, and Belliveau JW (1999). Conductivity mapping of biological tissue using diffusion MRI. *Ann. N. Y. Acad. Sci* 888, 314-316.
- Tuch DS (2004). Q-ball imaging. *Magn Reson Med* 52 (6), 1358-1372.
- Tzourio-Mazoyer N, Landeau B, Papathanassiou D, Crivello F, Etard O, Delcroix N, Mazoyer B, and Joliot M (2002). Automated anatomical labeling of activations in SPM using a macroscopic anatomical parcellation of the MNI MRI single-subject brain. *Neuroimage* 15 (1), 273-289.
- Uylings HBM, Rajkowska G, Sanz-Arigita E, Amunts K, and Zilles K (2005). Consequences of large interindividual variability for human brain atlases: converging macroscopical imaging and microscopical neuroanatomy. *Anat. Embryol* 210 (5-6), 423-431.
- Van Essen DC, Drury HA, Joshi S, and Miller MI (1998). Functional and structural mapping of human cerebral cortex: solutions are in the surfaces. *Proc. Natl. Acad. Sci. U.S.A* 95 (3), 788-795.
- Van Essen DC (2005). A Population-Average, Landmark- and Surface-based (PALS) atlas of human cerebral cortex. *Neuroimage* 28 (3), 635-662.
- Vogt C, and Vogt O (1919). Ergebnisse unserer hirnforschung. 1.-4. Mitteilung. *J. Psychol. Neurol.* 25, 59-86.
- Von Neumann J (1958). *The Computer and the Brain* (New Haven, CT: Yale University Press).
- Vovk U, Pernus F, and Likar B (2007). A review of methods for correction of intensity inhomogeneity in MRI. *IEEE Trans Med Imaging* 26 (3), 405-421.
- Walker AE (1940). A cytoarchitectural study of the prefrontal area of the macaque monkey. *The Journal of Comparative Neurology* 73 (1), 59-86.

- Wandell BA (1999). Computational neuroimaging of human visual cortex. *Annu. Rev. Neurosci* 22, 145-173.
- Watts DJ, and Strogatz SH (1998). Collective dynamics of 'small-world' networks. *Nature* 393 (6684), 440-442.
- Weissman DH, Roberts KC, Visscher KM, and Woldorff MG (2006). The neural bases of momentary lapses in attention. *Nat. Neurosci* 9 (7), 971-978.
- Wernicke C (1874). *Der Aphasische Symptomencomplex* (Breslau: Cohn and Weigert).
- Wittstock M, Grossmann A, Kunesch E, Walter U, Benecke R, and Wolters A (2010). Altered callosal function in cerebral microangiopathy. *J. Neurol* 257 (4), 590-597.
- Worsley KJ, Evans AC, Marrett S, and Neelin P (1992). A three-dimensional statistical analysis for CBF activation studies in human brain. *J. Cereb. Blood Flow Metab* 12 (6), 900-918.
- Worsley KJ, Taylor JE, Carbonell F, Chung MK, Duerden E, Bernhardt B, Lyttelton O, Boucher M, and Evans AC (2009). SurfStat: A Matlab toolbox for the statistical analysis of univariate and multivariate surface and volumetric data using linear mixed effects models and random field theory. In: (OHBM Poster).
- Worsley KJ, Taylor JE, Tomaiuolo F, and Lerch J (2004). Unified univariate and multivariate random field theory. *Neuroimage* 23 Suppl 1, S189-195.
- Young MP (1992). Objective analysis of the topological organization of the primate cortical visual system. *Nature* 358 (6382), 152-155.
- Zhang Y, Brady M, and Smith S (2001). Segmentation of brain MR images through a hidden Markov random field model and the expectation-maximization algorithm. *IEEE Trans Med Imaging* 20 (1), 45-57.
- Zilles K, and Amunts K (2010). Centenary of Brodmann's map--conception and fate. *Nat. Rev. Neurosci* 11 (2), 139-145.

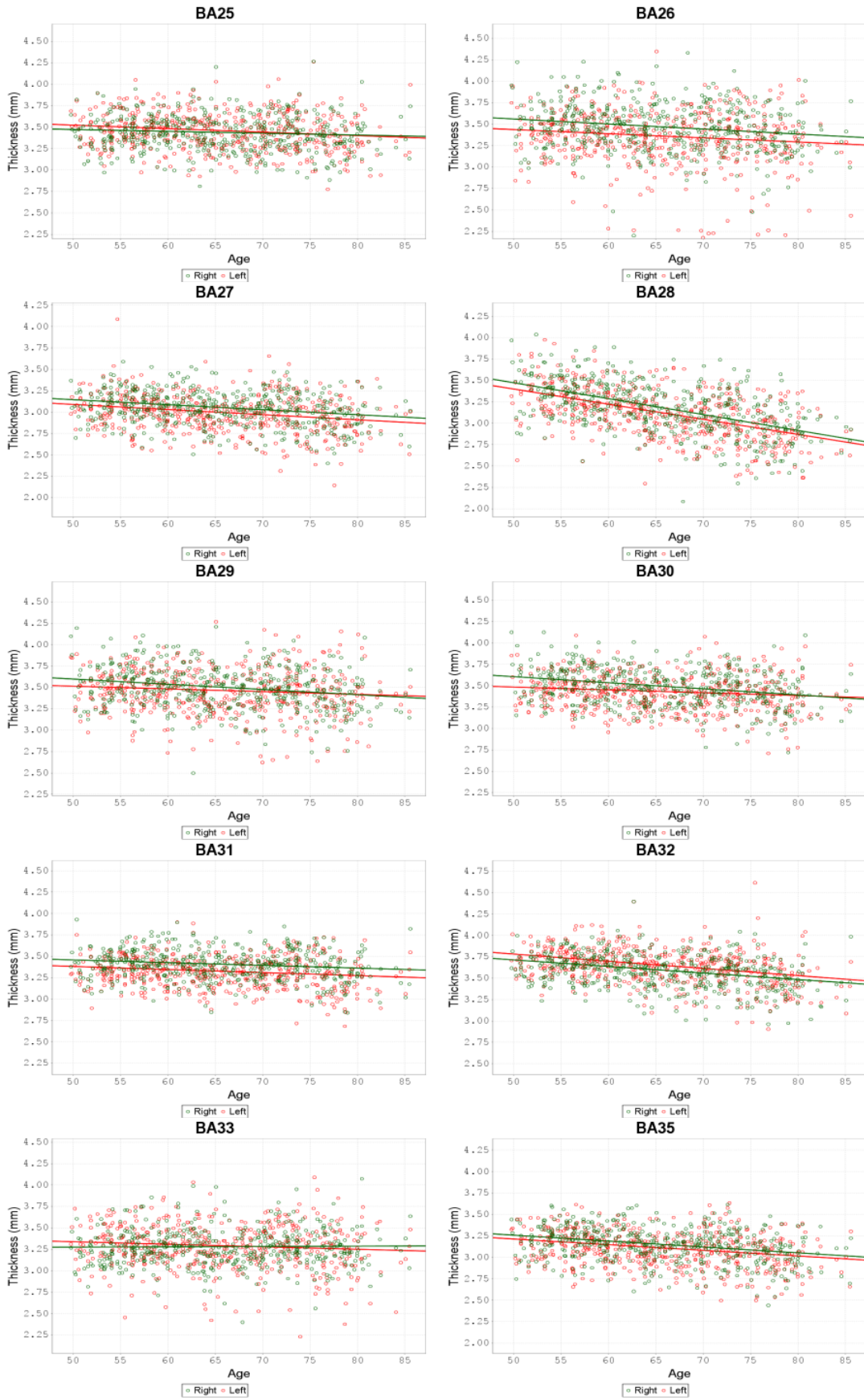
## 8. Appendix

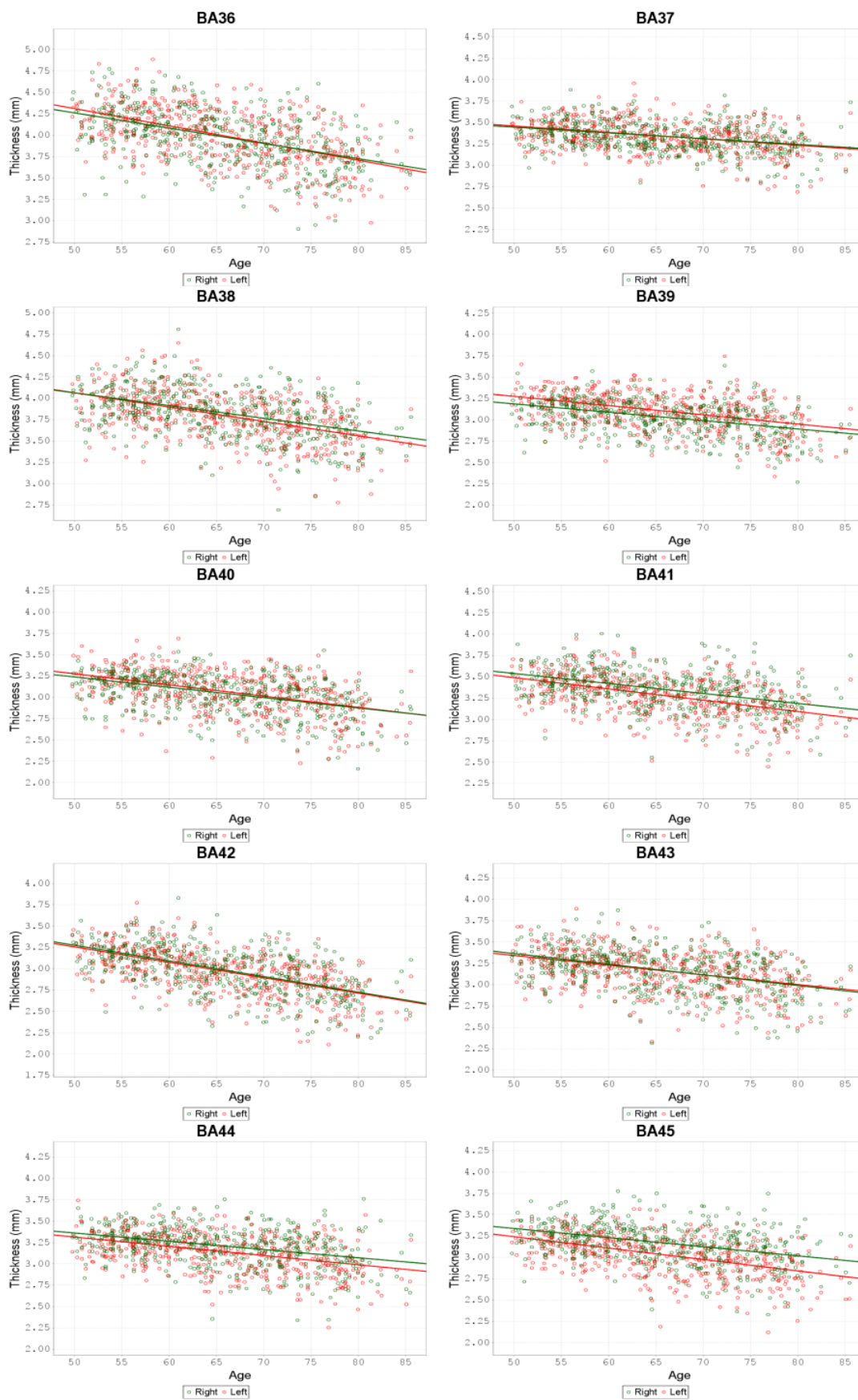
Scatterplots of  $Age \times Thickness$  for each BA ROI, separated by hemisphere.





Appendix





Appendix

